Durham E-Theses

Chemical Modification of Graphene via A Potassium Graphite Intercalation Approach

JIANG, YU

How to cite:

JIANG, YU (2018) *Chemical Modification of Graphene via A Potassium Graphite Intercalation Approach*, Durham theses, Durham University. Available at Durham E-Theses Online: http://etheses.dur.ac.uk/12799/

Use policy

Chemical Modification of Graphene via A Potassium Graphite Intercalation Approach

Yu Jiang

A thesis submitted in partial of the requirement for the degree of Master of Research

Department of Chemistry
Durham University

09.2018

Acknowledgements

Abstract

Graphene is frequently termed a 'wonder material' due to its excellent properties and potential for use in a broad range of applications. Key to the realization of graphene in various applications is surface modification. The aim of the work was to investigate a facile approach to functionalize graphene with various functional groups for specific applications. To this aim, a graphite intercalation compounds (GICs) approach was introduced to activate graphene layers. In the first study, two kinds of natural graphite were used for preparation of potassium GICs. Raman spectroscopy and Powder XRD were used to investigate the quality of prepared GICs. It was found the GICs prepared from 325 mesh graphite possessed a higher order of intercalation. In the second study, potassium GIC was functionalized by various diazonium salts and benzyl bromides. Successful functionalization was confirmed by Raman spectroscopy, Thermogravimetric Analysis (TGA) and X-ray photoelectron spectroscopy (XPS). Finally, functionalized graphene was decorated with amine modified gold nanoparticles. This work provided a potential approach to functionalize graphene with various functional groups.

Chapter 1: Literature Review

1.1 Properties and Applications of Graphene

Graphene is a single-layer two-dimensional (2D) material composed of sp^2-hybridized carbon. It is the thinnest material found yet of only one-atom thickness and is the first successfully isolated 2D crystal. Since the isolation of graphene by Geim and Novoselov in 2004[1], the research field of graphene has undergone rapid expansion. The number of publications relating to GBMs (graphene-based materials) has increased every year and reached to 83 per day in 2017 (Figure **1**). This tremendous interest towards graphene is not only caused by its unique structure and exceptional properties, but also due to the fact that its finding has profoundly changed our understanding of 2D crystals, which were thought to be thermodynamically unstable and cannot be isolated at finite temperature. With the rapid development of GBMs, other 2D materials such as molybdenum disulfide (MoS_2)[2], hexagonal boron nitride (h-BN)[3], and phosphorene[4] have also been widely studied in aspect of their material properties, in order to broaden new applications of 2D materials.

During the past few years, research towards graphene in terms of its mechanical, electrical, thermal, and optical properties has been intensively conducted. Specifically, graphene has been found to be stronger than steel with a high Young's modulus of about 1TPa[5]. A sheet of single-layer graphene has a theoretical specific surface area (SSA) of 2630 m^2/g, which is larger than that of carbon black (typically < 900 m^2/g) and carbon nanotubes (from 100 to 1000 m^2/g), and is similar to activated carbon[6]. Furthermore graphene possess incredible electron mobility under ambient conditions[1], according to the reported value

exceeding 15,000 $cm^2/V^{-1} s^{-1}$. Graphene also has a superior thermal conductivity of ca. 5,000 W/mK at room temperature[7]. Besides, a single layer graphene has excellent transmittance and is found to have a low opacity of 2.3 ± 0.1% and negligible reflectance (<0.1%)[8].
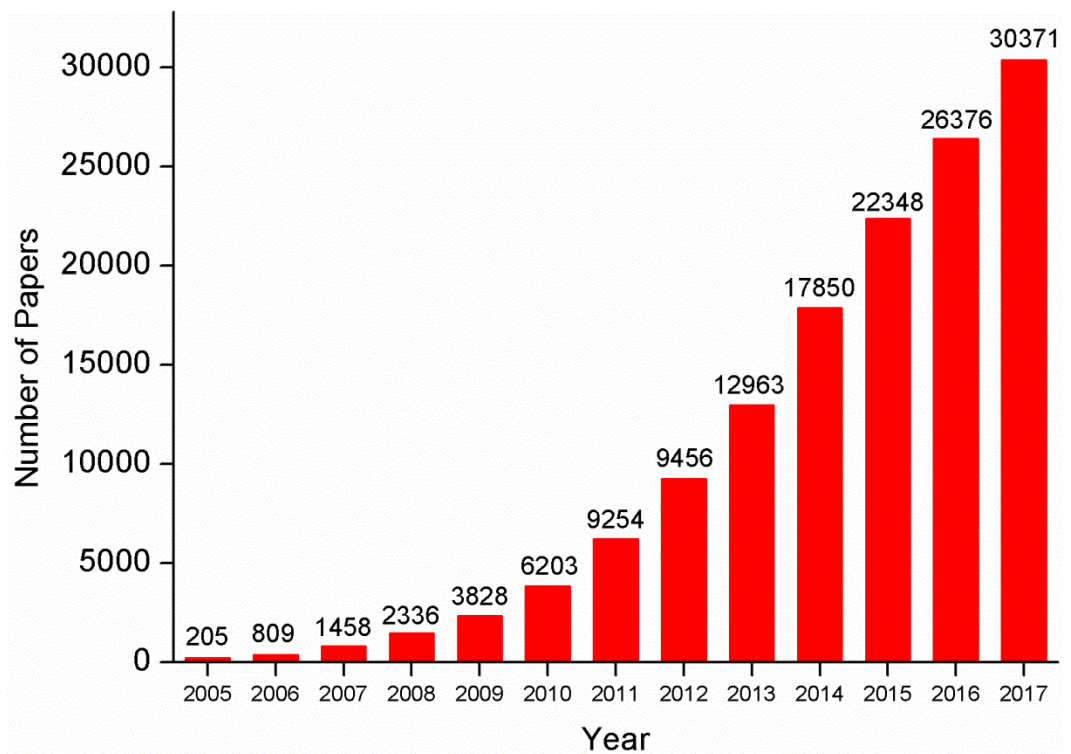
Figure 1 Number of publications in the field of graphene from 2005-2017. Data obtained from Web of Science. Key word: Graphene.

Graphene is considered as 'wonder material' due to its fantastic material properties. However, the unique properties listed above arise from an ideal single-layer pristine graphene sheet while few-layer graphene can start to pose very different properties to single-layer graphene, as its electronic structure begins to approach the 3D limit of graphite at 10 layers. GBMs including pristine graphene films[9, 10], pristine graphene powder[1, 11, 12], graphene nanoribbons (GNRs)[13], graphene oxide (GO) and reduced graphene oxide (rGO)[14-16] as well as three-dimensional (3D) structured graphene foam[17, 18] have been widely investigated and

4

fabricated at laboratorial or industrial scale. The synthetic versatility of GBMs enables a wide

range of functionality and tailored properties that open a great potential in many new

applications (Figure **2**)[19]. For example, foldable graphene films made by chemical vapor

deposition possess excellent electrical conductivity and transparency[9], which can be used for

bendable touch screen and other flexible electronics devices; pristine graphene powder

exfoliated from bulk graphite can be used in the flexible circuit printing as the conductive

ink[20-22]; GO synthesized via oxidation and exfoliation of natural graphite flakes contains oxygen

functional groups attached, making it easily to be fabricated for graphene based composites[23].

However, the defects in the carbon matrix of GO caused by the oxidation and doping of the

functional groups disrupts the delocalized structure, reduce its electrical and thermal

conductivity. The reduction of GO can remove the attached oxygen containing groups and to

some extent recover the conjugated structure of carbon matrix, and the obtained reduced GO

possesses a high surface/mass ratio as well as a relevantly high conductivity that can be used

for energy storage devices[17, 18, 24]. Besides, heteroatom doped graphene[25] and GNRs[13] have an

energy gap between the valence band and conductive band. As graphene is a zero-band gap

material, doping of heteroatoms and processing graphene/graphite into GNRs can open a band

gap (usually between 0.1 to 0.5 eV) to this material, which make it possible for field effect

transistor (FET) applications.

Apart from the main-stream applications mentioned above, GBMs also show great

potential in the liquid lubricant industry[26]. The high chemical inertness, extreme strength, and

easy shear capability of graphene are the major favorable attributes for its impressive

tribological behavior. In addition, it is thought that the graphene powder or dispersion could

reduce the wear and friction in nano-scale and macro-scale electromechanical systems, therefore, a high-performance functional coating can extend their lifetime.
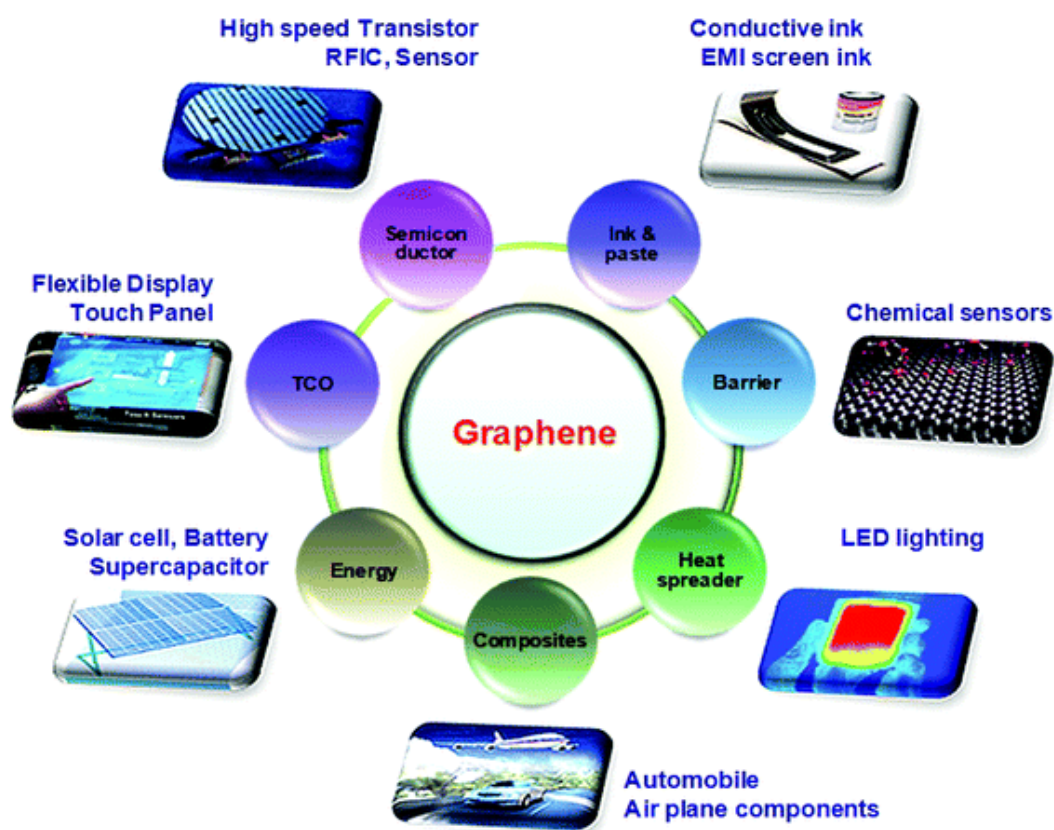
Figure 2 Overview of applications of graphene-based materials in different sectors. Reproduced with permission from ref 19. Copyright 2015 the Royal Society of Chemistry.

Besides, graphene exhibits excellent ability to passivate a surface.[27-30] The corrosion and oxidation of the surface of metals lead to performance degradation in terms of thermal and electrical conductivities. Due to the impermeability of graphene film towards the molecules of most liquids and gases including water and oxygen, simply coating a monolayer of graphene on a metal surface can significantly slow down the corrosion or oxidation process and protect the surface.

6

1.2 Preparation of Graphene

The methods for the preparation of graphene can be divided into two categories: top-down and bottom-up. The top-down method involves the exfoliation of graphene from bulk graphite while bottom-up method uses an alternative carbon source to build up the graphene structure. There are four main approaches to produce graphene: 1) chemical vapor deposition (CVD); 2) epitaxial growth of graphene; 3) mechanical exfoliation from bulk graphite and 4) reduction of graphene oxide (GO). Among these methods, method 1 and 2 can be classified as bottom-up methods, while method 3 and 4 are top-down approaches. To date, the CVD method has been used to produce high-quality graphene films on an industry scale although mechanical exfoliation as well as the reduction of GO are probably the most promising ways to prepare graphene powder at large scale[9, 10, 31].

1.2.1 Chemical Vapor Deposition

Chemical vapor deposition (CVD) is the growth of graphene films on a metal substrate using high temperature pyrolysis of a carbon-containing gas as the precursor. It is widely used to produce carbon nanotubes, graphene, and other 2D film materials such as MoS_2[32] and h-BN[33, 34]. As the graphene films produced by the CVD method can exhibit superior conductivity, large lateral sizes (from micrometers to millimeters) and thin thickness (high proportion of mono-layer graphene), this method has been recognized as an appropriate way to manufacture graphene for electronic applications[9, 13].
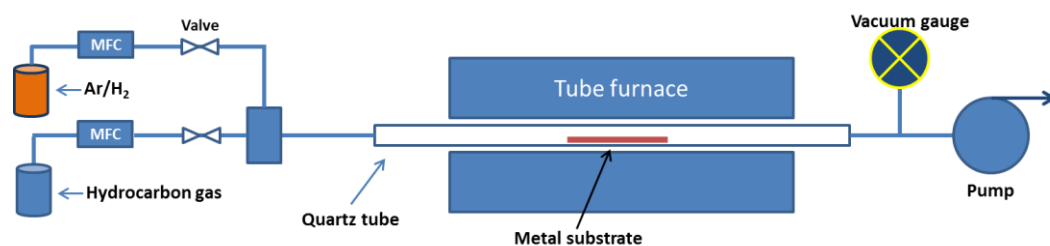
Figure 3 Schematic diagram of typical set-up for CVD graphene synthesis (MFC: mass flow controller).

The growth of graphene is usually conducted in a tube furnace equipped with a temperature and pressure control system (Figure **3**) and the whole process is conducted under the protection of Ar/H$_2$. In the first step of the procedure, the metal substrate is placed in the quartz tube and heated to a high temperature (~1000 °C) under a hydrogen atmosphere to eliminate impurities. The mixture of hydrogen and carbon-containing gas such as methane are then passed into the tube to achieve the growth of carbon films. The system is then cooled down to room temperature under the flow of hydrogen. The metal substrate plays a very important role in the growth of graphene.

Transition metals have been used for the graphene film growth. As the d orbitals of transition elements are not fully occupied, they can form chemical bonds with carbon atoms at high temperature, which can weaken the C-H bonds of the carbon sources and facilitate the decomposition. The fragments of carbon source are then assembled on the surface of the substrate at a high temperature to form the carbon film. Single crystalline transition metals such as Co, Pt, Pd, Ir and Ru have been used for growth of graphene by the CVD method under ultrahigh vacuum (UHV) condition. However, the high cost of single crystalline materials and the extreme reaction conditions have restricted the scale of materials preparation. In 2009, Kong and co-workers[35] successfully grew graphene on polycrystalline Ni substrate. In this work,

ultrathin graphene film (1-10 layers) has been grown on the substrate by using methane as the carbon source and hydrogen as the carrier gas. This was the first time that continued larger-area graphene films were made by CVD methods and successfully transferred to a different substrate.

The graphene grown on Ni substrate usually has small crystallite sizes and non-uniform distribution of film thickness. This can be attributed to the high solubility of the carbon atoms in Ni at high temperature. When the Ni substrate is heated up to the reaction temperature, excess carbon atoms diffuse into the Ni phase due to its high solubility. The excess carbon atoms segregate over the cooling down step as the solubility of carbon decreases with the temperature[36, 37], resulting in the formation of thick carbon films. To address this issue, several methods including controlling the cooling process and using other metal as the substrate, have been developed. Among the transition metals, Cu shows a low solubility towards carbon atoms and theoretically excellent potential for large-area homogenous graphene films growth. For example, Ruoff and co-workers[38] have successfully grown graphene films at a micrometer scale on copper foils by using methane and hydrogen as precursors at 1000 $^{\circ}$C. Scanning electron microscopy (SEM) images show that the produced graphene films were uniform and continuous. Raman spectra showed an I_{2D}/I_G ratio of 2, indicating the graphene film is predominantly made up by monolayer flakes. An analysis combining Raman spectra and optical microscope showed that only < 5% of the area was covered by bilayer or three-layer flakes. It is noteworthy that when the reacting time was extended from 10 min to 60 min, no significant difference of the grown graphene film was observed. They concluded it was because the growth of graphene was a surface-catalyzed process at low pressure. After this work, a

graphene film with larger a lateral size of 30 inches has been successfully produced on a Cu

substrate and tested for touch screen use[9].

Synthesizing graphene sheets by CVD is a popular bottom-up method to manufacture

high-quality, large-area graphene films for many applications. However, CVD-derived graphene

films are typically polycrystalline[16, 39] which degrades its mechanical and electrical performance

due to the existence of grain boundaries. Therefore, developing approaches for the growth of

large-area and single-crystal graphene films has been targeted as the next critical step. Given

that during the conversion of hydrocarbons to graphene grains the precursor molecules firstly

deposit on the active sites of the substrate to form small nuclei, which then adsorb other

carbon species at the edges to achieve the growth[39], the key of obtaining high quality graphene

films lies on the control of nucleation density at a low value to reduce the formed boundaries.

There are several approaches to meet this goal. For instance, diluting the precursor by inert

gas[40] and reducing the flow rate as well as partial pressure of carbon sources[41] yielded a lower

density of graphene nuclei. In addition, optimizing the surface structure of copper foil by

electrochemically polishing[42], preheating under argon atmosphere[43-45] and short-time exposure

to oxygen[46] can all reduce the nucleation density. Besides, other substrates such as Cu-Ni

alloys[47], noble metals[48, 49] and insulating materials[50] have shown potential as alternatives for

CVD growth of high quality graphene films.

1.2.2 Epitaxial Growth

Epitaxial growth is an alternative method to produce graphene films at wafer size by

using commercially available silicon carbide (SiC) wafers as the starting material.
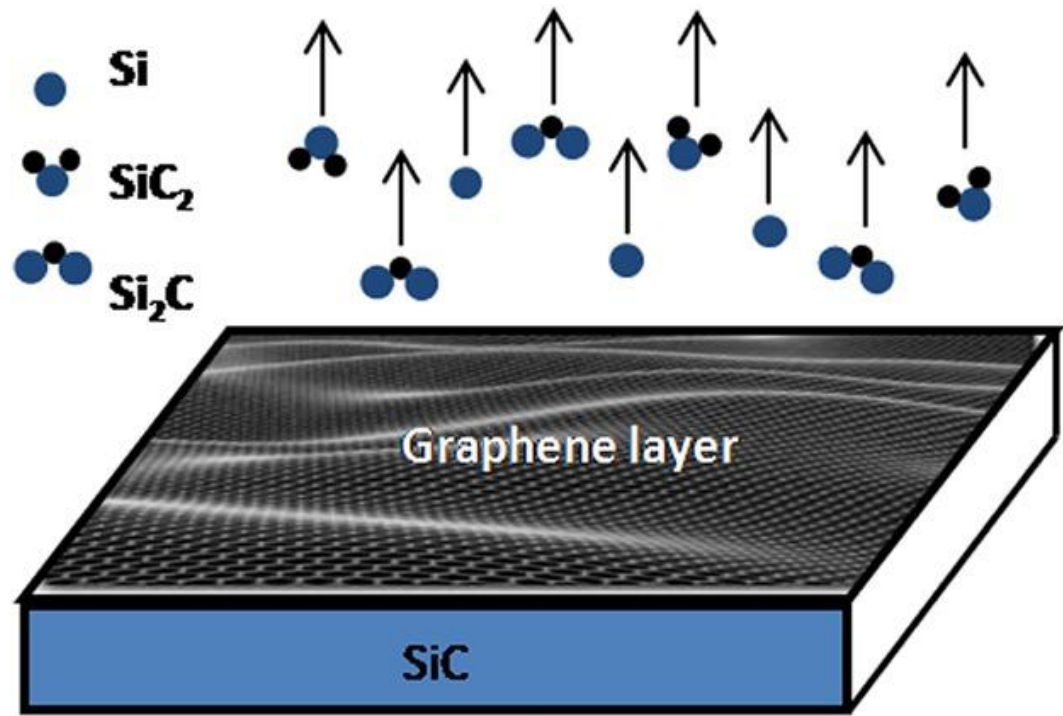
Figure 4 Growth of epitaxial graphene on silicon carbide wafer via sublimation of silicon atoms. Reproduced with permission from ref 51. Copyright 2016 Wiley Online Library.

In this approach, a graphene film can be prepared by annealing SiC wafer at high temperature (> 1200 °C) under UHV condition or atmospheric pressure. During this process, silicon atoms evaporate and escape from the SiC surface while carbon species remain in the solid-state due to its negligible vapor pressure compared to silicon[51]. Finally, graphene films deposited on a Si substrate through the rearrangement of the remaining carbon atoms (Figure **4**). The main advantage of the epitaxial growth of graphene on a SiC wafer is that no transferring procedure is required for the preparation of electronic devices as the SiC wafer itself is a semiconductor[52].

Attempts to produce graphene through vacuum graphitization of SiC wafers have been carried out, and the differences of graphene sheets grown on Si-terminated (0001) and C-terminated (000$\bar{1}$) faces have been discussed[53-55]. However, the high sublimation rate of Si at

a high temperature in UHV resulted in poor quality of graphene while the relatively low annealing temperature led to low-graphitized graphene grains. To address these issues, a modified confinement controlled sublimation (CCS) method involving the use of inert gas and external gaseous silicon flow has been used to suppress the silicon sublimation and improve the mobility of carbon atoms. Virojanadara et al.[56] successfully grew graphene films under argon atmosphere at an ambient pressure of 1 atm. The role of argon is to slow down the loss of silicon atoms thereby allowing a higher temperature (2000 ^{o}C) to be reached to enhance the graphitization. The low energy electron microscope (LEEM) images revealed a better thickness uniformity of the sample compared with that prepared under UHV. More recently, a team from Georgia Tech[57] produced graphene by confining the SiC wafer into a graphite enclosure with a diameter-controlled leak and annealing it in an inert gas and under UHV, respectively. The enclosure limited the escape of silicon and maintained a high silicon vapor pressure around the wafer. They concluded that the concentration of silicon vapor is constant over the surface and near thermodynamic equilibrium, which is important for the uniform growth of graphene.

1.2.3 Mechanical Exfoliation

As mechanical force can be used to separate the stacked layers in graphite, pristine graphene flakes with few defects can be produced by the mechanical exfoliation of bulk graphite. To date, several methods including micromechanical cleavage, liquid phase exfoliation (LPE), and ball milling have been developed to meet this goal. The initial protocol of cleavage of graphite crystals was developed by Geim and co-workers[1]. In their preparation, graphene sheets were peeled off from pre-treated highly-oriented pyrolytic graphite (HOPG) by using scotch tape, which was then transferred onto a SiO_2 wafer for characterization. The

prepared carbon films were made up of single-layer and few-layer graphene with lateral size from 10 μm to 100 μm. Due to the highly crystalline structure of the exfoliated graphene films[58], it exhibited excellent electronic properties.

As the scotch tape preparation cannot be scaled up, exfoliating graphite in liquids has been developed to produce low-defect graphene flakes at a larger scale. The LPE approach typically involves three steps: 1) dispersing graphite in a solvent; 2) mechanical exfoliation, and 3) remove of solvent and un-exfoliated large flakes. In 2008, Coleman[59] and co-workers successfully produced graphene sheets by exfoliating graphite powder in N-methylpyrrolidone (NMP) by bath sonication. During the sonicating treatment, the pressure fluctuations caused the growth and collapse of micrometer-sized bubbles and voids, and the formed cavitation then overcame the van der Waals interaction between graphene layers thereby achieving exfoliation[12]. Once the graphene sheets were exfoliated, they were stabilized by NMP molecules to avoid re-aggregation. UV-vis-IR showed the concentration of graphene suspension reached up to 0.01 mg ml^{-1} after centrifugation. TEM showed that graphene flakes were made up of monolayer, bilayer and few-layer graphene sheets with lateral size of several micrometers, with the fraction of monolayer graphene flakes ca. 28%. The absence of a D peak in the Raman spectra indicated no introduction of significant structural defects. However, the concentration of graphene dispersion is too low to be practically useful. To address this issue, the initial concentration of graphite was improved and the sonicating time was extended[60] and finally a concentrated graphene suspension (up to 1.2 mg ml^{-1}) with 4 wt.% monolayers has been obtained.

Shear mixing is an alternative method to exfoliate graphene in the liquid phase. Differing

from sonication, shear mixing uses shear force to delaminate graphene nanosheets. The first trial of producing graphene by shear mixing at a large scale was conducted by Coleman and co-workers[11] in 2014. In their process, a defined amount of graphite powder was firstly mixed with NMP in a vessel. Subsequently, the mixer head was lowered into the liquid and the rotating speed of the shear mixer (Figure **5a**) increased gradually until the set value was reached. The mixer then ran for a predetermined time for efficient exfoliation of graphite. TEM (Figure **5e**) illustrated the lateral sizes of exfoliated graphene sheets ranged from 300 to 800 nm and the number of layers of exfoliated flakes was between 4 and 7. XPS showed no evidence of oxidation and Raman spectra showed no defects were introduced to the basal planes. Compared with sonication, preparation of graphene through shear mixing possesses advantages in terms of less time and energy consumed. Most importantly, the production rate increases strongly with the mixing volume[61], which is essential for scale-up. Apart from the two methods mentioned above, other approaches involving shear force introduced by fluid dynamics such as high pressure homogenization[62], turbulence-assisted exfoliation[61] and microfluidization[22] were also investigated to enhance the production efficiency of graphene nanosheets.
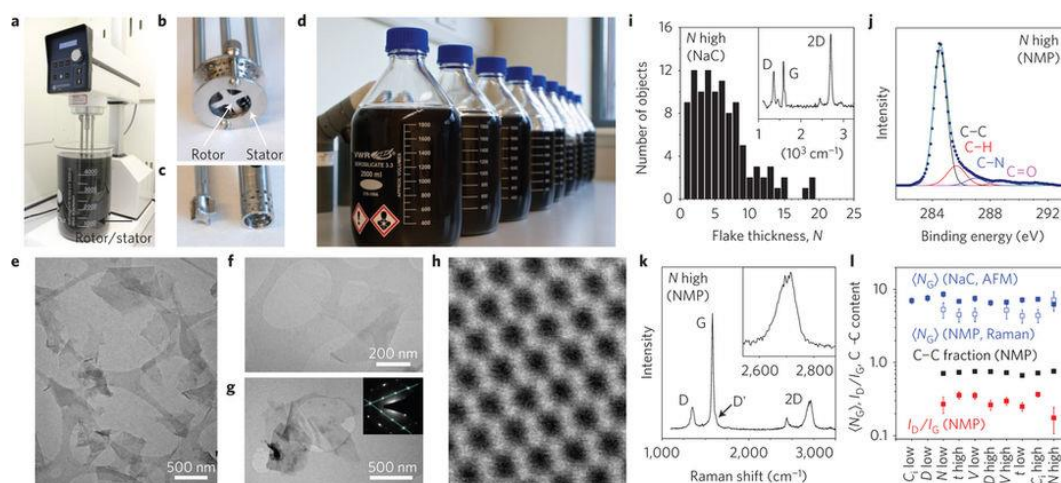
Figure 5 a, A Silverson model L5M high-shear mixer with mixing head in a 5 L beaker of graphene dispersion. b.c, Close-up view of mixing heads. d, Graphene-NMP dispersions produced by shear exfoliation. e-h, TEM image of graphene nanosheets. i, Histogram of nanosheet thickness. j,k, XPS (j) and Raman (k) spectra. l, Information extracted from Raman, XPS and flake thickness data plotted versus dispersion type. Reproduced with permission from ref 11. Copyright 2014 Nature Publishing Group.

In general, the LPE method can produce graphene few-layers flakes possessing small lateral sizes (typically < 1 micrometer) and few defects. Compared with scotch tape peeling, LPE is more productive and is recognized as a more promising way to produce pristine graphene nanosheets. However, there are still some obstacles to overcome. For example, long time sonicating and shear mixing can decrease the lateral size of graphene sheets[12]. This will restrict the range of applications of the graphene produced. Choice of solvent is the most important factor for high-efficient exfoliation. It has been demonstrated that solvents with interfacial intension matching that of graphene can separate the graphene sheets, and the net energetic cost of this process can be minimized. The enthalpy of mixing graphene with stabilizer can be calculated by equation **1**:

$$\frac{\Delta H_{mix}}{\Delta V_{mix}} \approx \frac{2}{T_{flake}} (\delta_G - \delta_{sol})^2 \phi \qquad (1)$$

In equation **1**, δ_G and δ_{sol} are the square root of the surface energy of graphite and solution, respectively, T_{flake} is the thickness of a graphene flake and ϕ is the graphene volume fraction. Given that the surface tension of graphite γ_G is 40 mJ/m^2, one can conclude that the solvent with a surface tension of 40 mJ/m^2 should be the best solvent for LPE. Further mechanism studies have also confirmed this conclusion[11]. Some organic solvents such as

NMP[59] (NMP ~40 mJ/m^2), N,N-dimethylformamide[63] (DMF ~37.1 mJ/m^2), and ortho-dichlorobenzene[64] (o-DCB ~37 mJ/m^2) can meet this requirement. However, these solvents are expensive, toxic and hard to remove after exfoliation due their high boiling points. Besides, other kinds of stabilizers including ionic liquid[59, 65], polymers[66], and surfactants[67] have been used to improve the efficiency of exfoliation.

1.2.4 Reduction of Graphene Oxide
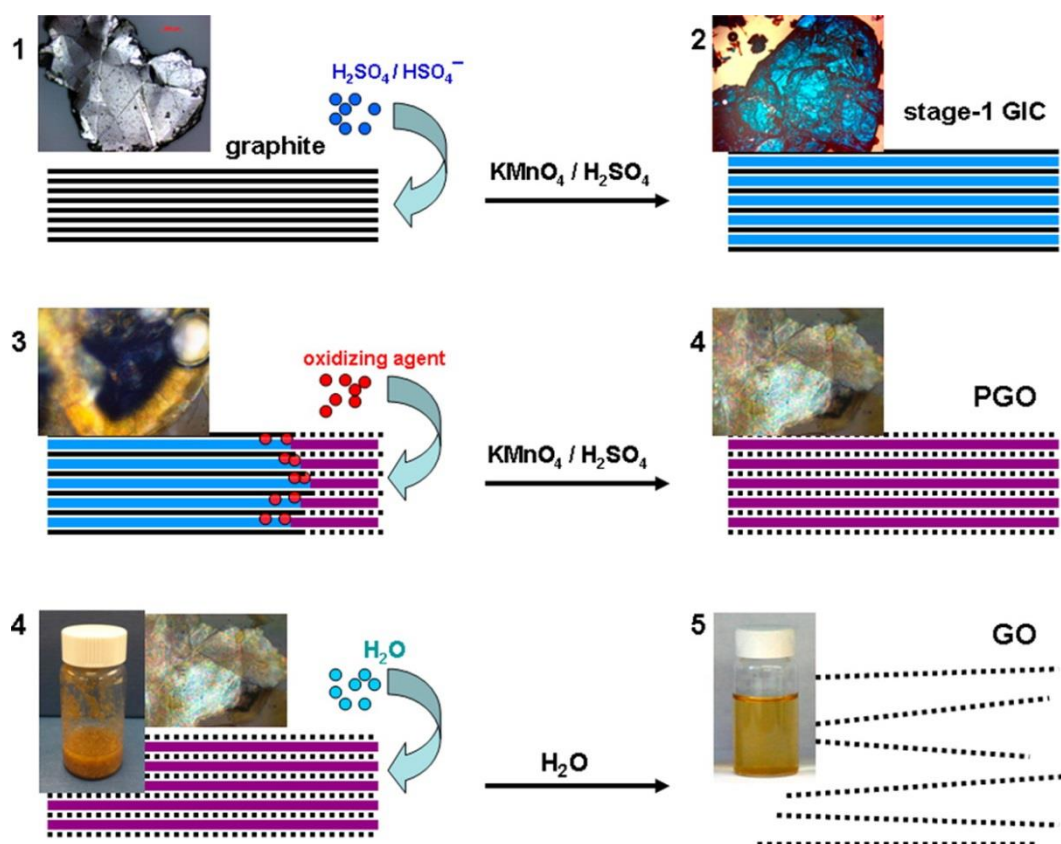
Figure 6 Schematics of conversion of bulk graphite into GO with corresponding micrographic images or sample appearances at each phase. Reproduced with permission from ref 68. Copyright 2014 American Chemical Society.

The reduction of graphene oxide (GO) is considered as one of the most widely used methods to produce graphene powder at low cost and large scale. GO is usually produced by

oxidation and exfoliation of bulk graphite. This process can be achieved by treating graphite with a range of strong oxidizing agents[16] such as potassium chlorate ($KClO_3$), nitric acid (HNO_3), and potassium permanganate ($KMnO_4$). Among various methods, the Hummers' method as well as modified Hummers' method[14, 15] involving the utilization of potassium permanganate, sodium nitrate, and sulfuric acid are the most popular methods for GO preparation. The mechanism of GO preparation through this method can be described as follow[68]: as shown in Figure **6**, bulk graphite was firstly converted to graphite intercalated compounds (H_2SO_4-GIC) by mixing graphite with concentrated sulfuric acid (H_2SO_4), then the H_2SO_4-GIC was further oxidized by the oxidizing agent. After that, the oxidized graphite was exfoliated to GO after reacting with water.
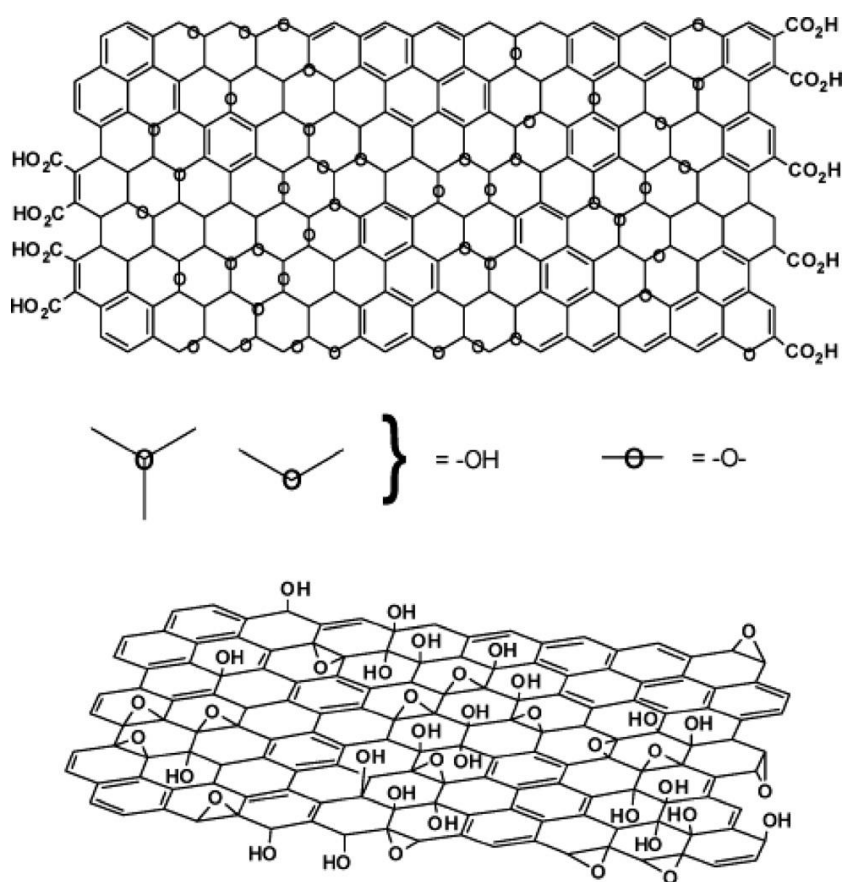
Figure 7 Variations of the Lerf-Klinowski model in the presence or absence of carboxylic groups on the

periphery of the basal plane in GO. Reproduced with permission from ref 16. Copyright 2010 the Royal

Society of Chemistry.

Currently, several models[16] have been developed to describe the specific structure of GO

although it remains difficult to precisely define the structure of this material. More recently,

Ruoff and co-workers[69] have used ^{13}C-labled solid-state nuclear magnetic resonance (SSNMR)

characterization to investigate the structure of GO. It was found one of the possible simulations,

Lerf-Klinowski model (Figure **7**), looks most promising.

Since the surface of GO are grafted with lots of oxygen containing functional groups such

as hydroxyl, carboxyl and epoxy, the dispersibility of GO is significantly higher than pristine

graphene in common solvents such as water, which makes this material possess greater

processability as well as high potential in many applications including energy storage[70, 71],

biological applications[70], and nanocomposites[72, 73].

However, a high density of defects introduced during the oxidation process disrupts the

conjugated structure of the carbon matrix. GO exhibits poor material performances in terms of

thermal and electrical conductivity. One of the most promising ways to address this issue is

reducing GO to form the reduced graphene oxide (rGO). The reduction of GO can remove most

of the attached functional groups and to some extent "recover" the highly defective structure.

The approaches for reduction of GO can be divided into three categories: 1) chemical reduction;

2) electrochemical reduction; 3) thermal reduction. The chemical reduction of GO involves the

utilization of a wide range of reducing agents. For example, Ruoff and co-workers[74] have

utilized hydrazine to reduce GO. In their process, GO was made from Hummers' method and

then mixed with hydrazine at 100 ^{o}C for 24 h. The obtained product showed an enhanced electrical conductivity of 2 x 10^2 S/m and an increase of C/O ratio from 2.7 (GO) to 10.3 (rGO), indicating the conjugated structure of GO was recovered and a large proportion of oxygen containing groups were removed. Besides, other reducing regents such as borohydrides (e.g. NaBH$_4$), aluminum hydride (e.g. LiAlH$_4$), and metal-alkaline (e.g. Zn/NH$_3$) have been investigated[75]. However, some of the reducing regents, like hydrazine, are dangerous and highly toxic. Furthermore, the degree of reduction cannot be precisely controlled due to the diversity of the functional groups.

Compared with chemical reduction, electrochemical reduction is a relatively fast, facile and environmentally friendly method to produce rGO[76]. The electrochemical reduction of GO is usually conducted in a three-electrode electrochemical system consisting of working, counter and reference electrodes as well as a buffer electrolyte. And it can be achieved by means of cyclic voltammetry (CV), linear sweep voltammetry (LSV) and constant potential method. For instance, Xia and co-workers[77] turned GO into graphene by applying controlled potentials on the working electrode from -0.8 V to -1.5 V in a PBS (K$_2$HPO$_4$/KH$_2$PO$_4$) solution. During this process, the reduction occurred on the GO adjacent to the working electrode and the solubility of GO decreased with the removal of functional groups, resulting in the sedimentation of rGO onto the electrode surface. Vacuum FT-IR spectroscopy indicated the successful removal of oxygen containing groups and the electrical conductivity of rGO was significantly improved after reduction. However, electrochemical reduction cannot move all the functional groups since a cathode potential more negative than -1.5V (vs. SCE) could lead to hydrogen evolution while some oxygen containing groups remain stable[78].

Alternatively, rGO can be produced by means of high temperature treatment and microwave irradiation. For example, a study conducted by Aksay and co-workers[79] showed that the oxygen containing groups of graphite oxide decomposed at high temperature, and the generated pressure between GO layers can facilitate the exfoliation of graphite oxide to form rGO. Based on the calculation, the pressures were in excess of 200 MPa and 600 MPa at 200 ^{o}C and 1000 ^{o}C, respectively. The high-temperature environment can also be achieved through microwave irradiation, which can provide a more rapid heating speed. For instance, Ruoff and co-workers[80] irradiated graphite oxide precursor in a microwave oven at 700 W for less than 1min. The XPS results showed that the oxygen containing groups were significantly removed. Moreover, the Raman spectra of produced rGO showed a decreased intensity ratio of D/G band, revealing the removal of covalently attached groups. By further optimizing reaction conditions, rGO with pristine graphene features could be produced. For example, Voiry and co-workers[81] partially reduced GO through heat treatment at 300 ^{o}C under argon, leading to a better absorption of GO towards a microwave energy, prior to microwave irradiation at 1000 W for 1-2 s under argon. The Raman spectra of produced rGO showed sharp and symmetrical G and 2D peaks, which were different from those of electrochemically, chemically or other thermally reduced GO. This may indicate that microwave irradiation could be a relatively fast approach to produce high-quality rGO.

Though GO can be thermally reduced to rGO quickly, the issue of large energy consumption of this process should be addressed before the large-scale production.

1.3 Functionalization of Graphene

Graphene possesses many excellent properties as well as great potential in many applications. However, the poor dispersity of graphene in most of common solvents such as water and ethanol, restricts its solution processability[82]. Graphene is a zero-gap semiconductor as the conduction and valence bands of graphene meet at the Dirac points. This feature makes it impossible to manufacture field effect transistors[83], which was thought to be a great application of this wonder material. Therefore, it is essential to change the surface properties as well as the electronic structure of graphene, and the most efficient way to achieve this goal is functionalization. Currently there are two types of methods to functionalize graphene: 1) non-covalent functionalization and 2) covalent functionalization, the latter is a more effective approach to tailor the properties of graphene and will be discussed in detail.

Given that the surface of pristine graphene (PG) is highly inert, functionalization of graphene is difficult. Fortunately, the surface of PG is not absolutely flat but wrinkled in many places, and the electrons of π-bonds within the aromatic carbons at these curved areas are less delocalized therefore can be more easily attacked by functional moieties[84]. To date, several approaches including radical addition[85-87], cycloaddition[88] and introduction of single atoms[89] have been used to modify PG, these methods will be discussed. Compared with PG, GO and rGO are more reactive towards functionalization. Considering the strongly oxidizing conditions during GO preparation, the GO flakes have attached oxygen containing groups[16] such as hydroxyl, carboxyl, and epoxy groups. As these groups are much more reactive than the carbon network, the issues of functionalization of GO and rGO depend much more on the interaction between the functional moieties and surface functional groups than they do on the carbon

layer and functional groups.

1.3.1 Radical Addition

Radical addition involves the reactive radicals generated by reduction of aryl-based diazonium salts, which has been used to modify carbon nanomaterials such as carbon nanotubes[90, 91] and fullerenes[92]. Since the discovery of graphene, studies regarding the functionalization of graphene via a diazonium reaction have been intensely studied. The reaction mechanism of diazonium functionalization is illustrated in Figure **8**[86]: 1) a delocalized electron is transferred from the carbon matrix to the aryl diazonium cation, making the latter into an aryl radical after releasing a molecule of N_2. 2) The aryl radical then attacks the carbon matrix under the protection of an inert gas and forms a covalent bond with the carbon atom, the hybridization of the carbon atom is then changed from sp^2 to sp^3. For example, Haddon and co-workers[85] achieved the modification of epitaxial graphene (EG) grown on SiC wafer by covalent attachment of aryl groups. They used 4-nitrobenzene diazonium tetrafluoroborate as the precursor
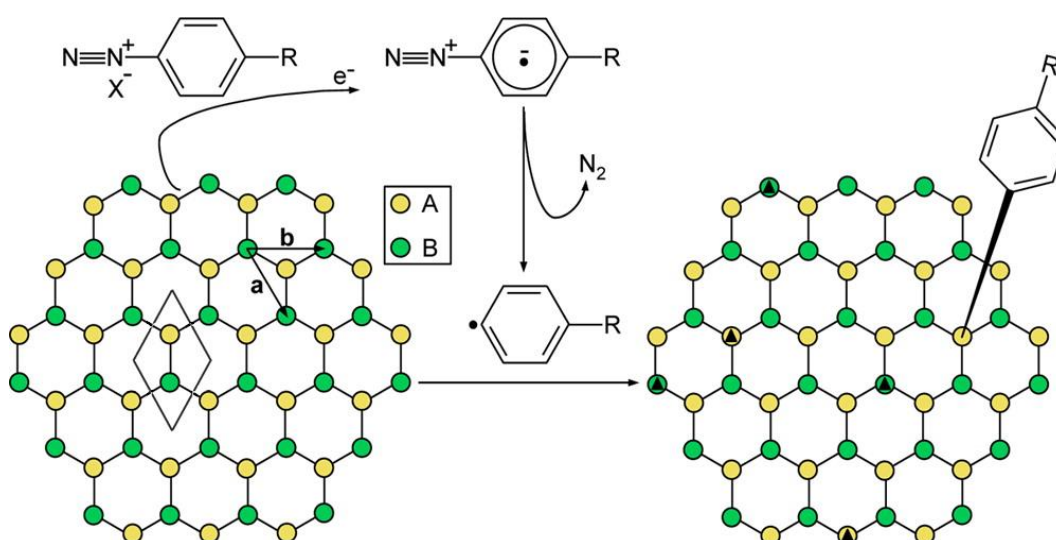
Figure 8 Schematic illustration of grafting a diazonium salt with functional group R and counter ion X⁻ to

and mixed it with SiC supported graphene in acetonitrile (ACN). The reaction was carried out under an argon atmosphere at room temperature for 20 h. The presence of NO_2 groups on the EG surface was confirmed by FT-IR and XPS. A p-type doping of epitaxial graphene was also observed through XPS, revealing a successful covalent modification. The cyclic voltammetry (CV) measurement of the modified EG showed the surface coverage of the functional moieties is on the order of 10^{15} molecules/cm^{-2}. It is noteworthy that the conductivity of modified EG decreased after functionalization, compared with pristine EG. However, the effects of modification on the band structure and dispersity of graphene were not discussed. After that, Tour and co-workers[93] reported another protocol, in which the thermally expanded graphite was pre-modified by in-situ formed diazonium salt derived from 4-bromoaniline. The pre-functionalized graphite then experienced a mild sonication treatment in N,N'-dimethylformamide (DMF) and was exfoliated down to graphene sheets. XPS measurement demonstrated the successful attachment of Br on graphene with a concentration varied from 0.56% to 0.67%, Energy Filtered Transmission Electron Microscopy (EFTEM) images confirmed that Br atoms were mainly distributed at the edges of graphene flakes. Besides, the solubility of modified graphene ranged from 0.01 to 0.02 mg/mL in DMF, which is comparable to the situation of using stabilizers. The effect of modification towards the graphene band structure was discussed by Haddon and co-workers[94]. Graphene samples produced by mechanical exfoliation and epitaxial growth were tested after modification through the angle-resolved photoemission spectroscopy (ARPES) technique. The results showed that a band gap of 0.4 eV was introduced after functionalization. More recently, Guo and

co-workers[95] developed an electrochemical protocol to modify CVD grown graphene. The reaction was performed in a three-electrode system in which the graphene was attached on the working electrode, and a solution of sulfuric acid (0.1 M) containing (4-nitrophenyl) diazonium tetrafluoroborate was used as the electrolyte. The nitrophenyl group coverage on the surface of functionalized graphene was estimated to be 12.7% to 20.0%. Interestingly, the modification could be achieved within a few seconds and the ratio of nitro groups to amino groups could be controlled by altering the potential bias. Inspired by this discovery, modifying graphene by electrochemical grafting has been sufficiently studied to make the process more efficient [96-98].

There are several factors to influence the effectiveness of graphene modification through radical addition such as the morphologies of the graphene sheets, number of layers and the edge structure. Ruoff and co-workers[99] found that the carbon atoms at highly curved regions of graphene sheets were more active than those in basal planes. To increase the curvature, they deposited spherical SiO_2 nanoparticles on a Si substrate before the graphene was transferred onto it. After functionalization by using diazonium salts, a significantly enhanced intensity of the D band was observed at wrinkled areas of graphene sheets caused by SiO_2 nanoparticles, indicating a higher efficiency of the covalent functionalization. Strano et al.[100] concluded that the single-layer graphene possesses a 10 times higher reactivity towards radical attack than bi- or multi-layers graphene. In addition, the reactivity of carbon atoms at graphene edges is at least two times higher than that of interior carbon atoms. Another study carried out by Baek and co-workers[101] revealed that the freshly exposed graphene edges formed during the break of large graphite flakes show higher reactivity compared with those in

the basal plane due to the altered electronic structure and dangling bonds.

1.3.2 Cycloaddition

Functional moieties can also be grafted on the surface of graphene by cycloaddition method, in which the graphene acts as a diene or dienophile. A commonly used approach for cycloaddition-type functionalization is the Diels-Alder reaction. For example, Ma and co-workers[102] obtained aryne functionalized graphene by mixing graphene sheets with 2-triflatophenyl silane benzyne precursors. An enhanced D band in Raman spectra was observed after functionalization, revealing the successful covalent functionalization. The functionalization was further evidenced by the improved dispersibility of modified graphene in different solvents such as N,N-dimethylformamide (DMF),1,2-dichlorobenzene (O-DCB), and ethanol.

However, some researchers[44, 103, 104] concluded that the cycloaddition of graphene possessed the feature of region-selectivity. Specifically, the covalent cycloaddition reaction preferred to occur at edges or defective regions of graphene while non-covalent complexation was much more favorable on defect-free interior areas. Regarding this, a study recently reported by Simon and co-workers[105] pointed out that the functionality can also be grafted to the in-plane regions of graphene with the assistance of the substrate and bond polarization of the functionality.

1.3.3 Introduction of Heteroatoms

Alternative to radical addition and cycloaddition, the surface properties of graphene can also be altered by the introduction of single atoms including hydrogen, nitrogen, oxygen and

halogens.

Among several methods for introduction of heteroatoms, hydrogenation has been widely used for graphene functionalization, which can convert this highly conductive carbon material into a semiconductor or insulator. There are two popular ways to modify graphene by hydrogenation[25]: 1) gas based hydrogen plasma and 2) liquid based Birch reduction. The first gaseous hydrogenation was achieved by Elias and co-workers[106] under a low-pressure hydrogen-argon atmosphere (0.1 mbar, 10% H_2) with DC plasma. The obtained material exhibited an insulating feature after hydrogenation, revealed by a significantly enhanced dependence of resistivity towards temperature and decreased carrier mobility. Raman spectra showed a sharp D band as well as a D' band, which can be attributed to formation of C-H sp^3 bonds. A decreased and slightly broadened 2D band was also observed, which is another signal of covalent functionalization. Interestingly, the functionalized material could be recovered almost to the initial state by annealing the sample under argon atmosphere at 450 °C. Another study conducted by Lin and co-workers[107] showed that the rate of hydrogenation was controlled by the energy barriers, which strongly depended on the number of layers of graphene. Differing from radical addition, the hydrogenation of monolayer graphene is much less feasible than that of bi-layer or multilayers graphene.

Hydrogenation of graphene can also be achieved by Birch reduction, which is used to hydrogenate aromatic carbon based materials such as carbon nanotubes[108], fullerene[109] and graphene. The birch reduction involves the utilization of alkali metals such as lithium[110] and potassium[111] and liquid ammonia to generate solvated electrons, which can generate anionic radicals with the aromatic carbon rings of graphene. The negatively charged graphene is then

attacked by proton donors (e.g. t-BuOH, water) to form hydrogenated graphene. For example, Billups and co-workers[110] hydrogenated graphene by using lithium/NH$_3$ as the electron donor and tert-butyl alcohol as the proton donor. The formation of C-H bonds was confirmed by Raman spectra and FT-IR. TGA and element analysis showed the hydrogen content of graphene was 6%, and a band gap of 4 eV was obtained after hydrogenation.

Alternative to hydrogenation, fluorination is also an effective way to introduce heteroatoms in graphite[112, 113], carbon nanotubes[114, 115], and graphene. To date, there are mainly three approaches[116-119] to achieve fluorination: 1) halogen-based plasma; 2) exposure to halogen atoms derivatives such as XeF$_2$; 3) exfoliation of fluorinated graphite. For instance, Baraket and co-workers[120] employed plasmas generated from argon and SF$_6$ gaseous mixture to fluorinate CVD grown graphene sheets. XPS spectra of C1s showed a series of peaks attributed to fluorinated functionalities such as C-CF (286.5 eV), C-F (288 eV), and C-F$_2$ (290 eV). After exposure to Ar/SF$_6$, the fluorine concentration in carbon matrix reached up to 18%. Robinson and co-workers[118] exposed a graphene film grown on copper foil to XeF$_2$ gas at 30 °C for 30 to 1200 s. It was found that fluorination saturated at a concentration of 25% (C$_4$F) and 100% (CF) coverage for single side and double side modification, respectively. Compared with pristine graphene, the film resistance of C$_4$F was increased by 6 orders of magnitude. Moreover, a band gap of ~3.07 eV was introduced after 100% fluorination towards both sides of the graphene film. It is noteworthy that the C-F bond has reversed polarity compared with C-H bond due to the strong electronegativity of fluorine[119]. As a result, fluorination can not only change the band structure and resistance of graphene but also tailor its chemical properties and make graphene more susceptible to nucleophilic attack.

1.4 Characterizations of Graphene

1.4.1 Raman Spectroscopy
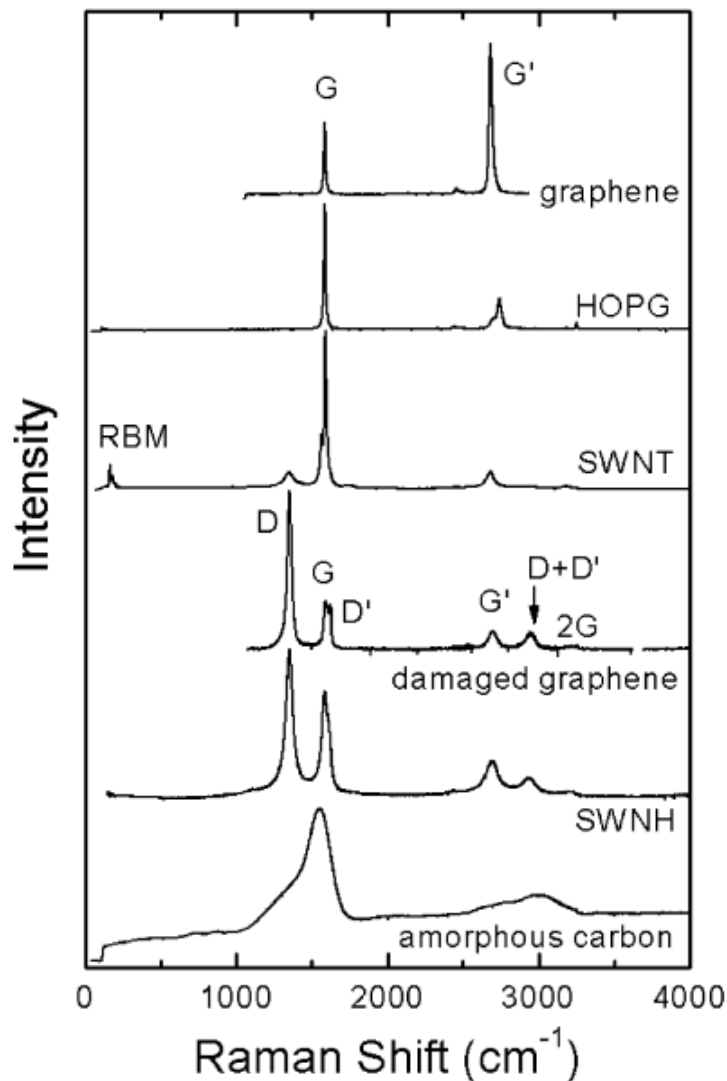
Figure 9 Raman spectra from different types of nanocarbons. The graphene-related structures are labeled next to their respective spectrum. Reproduced with permission from ref 121. Copyright 2010 American Chemical Society.

Raman spectroscopy is a useful tool to gain information towards the vibrational state of molecules. As the Raman spectra of different sp^2 hybridized materials have identified peak position, intensity and line shape, it can be used for the characterization of carbon nanotubes

and graphene based materials[121].

As shown in Figure **9**, the Raman spectrum of graphene has three featured peaks: D band (around 1355 cm^{-1}), G band (around 1582 cm^{-1}) and 2D band (around 2500 – 2800 cm^{-1}). The G peak is due to the doubly degenerate zone center E_{2g} mode and comes from the first order Raman scatting process of sp^2 carbon. It is the most featured peak of graphene as it is attributed to the in-plane bond stretching of sp^2 carbons. The D peak comes from the second order Raman scatting process and is the most important feature of sp^3 hybridized carbon. As a result, the D peak is due to the defects of the materials. The density of defects in the graphene matrix can be revealed by the intensity ratio of D peak to G peak (I_D/I_G) and has been used to evaluate the quality as well as degree of covalent functionalization of graphene. The 2D peak also comes from the second order Raman scattering process. The 2D peak is concerned with the interaction between graphene layers and sensible to the number of layers and the intensity ratio of 2D peak to G peak (I_{2D}/I_G) is usually used for approximate judgment of the number of layers of graphene. For instance, an I_{2D}/I_G value over 2 indicates the single-layer graphene and the value of I_{2D}/I_G decreases with the increase of graphene thickness. The shape of the 2D peak can also be used to evaluate the number of layers of graphene. For example, the 2D band of the monolayer graphene is a symmetrical single peak with a full width of half maximum (FWHM) below 30 cm^{-1} and can be well fitted by Lorentzian model. The 2D band of bi-layer or few-layer graphene usually involves the coupling of multiple peaks and the shape of 2D band is identifiable when the number of layers is less than 5. Graphene having a larger number of layers has a similar 2D peaks compared with graphite. It should be noticed that the I_{2D}/I_G as well as the FWHM value cannot be used to judge the number of layers of highly functionalized

graphene, as the doping of graphene will lead to a significant change of peak position and a deceased intensity of the 2D peak depending on the degree of functionalization[122].

1.4.2 Thermogravimetric Analysis (TGA)

Thermogravimetric analysis is a thermal analysis method to measure mass loss of sample over a programmed heating process in a controlled atmosphere. The plot of the sample mass is given as a function of temperature, which contains the information of the thermo-stability of the sample. In some cases, the TGA measurement can be coupled with mass spectroscopy (TG-MS) or Fourier Transform Infrared Spectroscopy (TG-FTIR) to further investigate the molecular structure of the gaseous fragment, which comes from the decomposition of the sample over the heating treatment.

The TGA can also be used as a tool to investigate the degree of covalent functionalization of graphene. The detaching of the covalently attached functionality usually starts from 300-400 °C in inert atmosphere, and the mass loss after this point can be used to calculate the concentration of functionality by equation **2** shown below:

$$C_F = \frac{W_F/M_F}{W_G/12} \qquad \textbf{(2)}$$

Where C_F is the concentration of functionality, W_F is the mass loss, M_F is the molecular weight of the functionality and W_G is the residual weight of the carbon materials. It should be noticed that this calculation can only be used in case of pristine graphene functionalization as GO and rGO contain lots of oxygen groups so their basic unit is not simply a carbon atom.

1.4.3 X-ray Photoelectron Spectroscopy (XPS)

X-ray Photoelectron Spectroscopy (XPS) is a surface-sensitive quantitative spectroscopic technique which can measure the elemental composition in the sample surface and the chemical or electronic state of each element. A typical XPS measurement is conducted under ultra-high vacuum (UHV) condition by bombarding the sample with x-rays. During this process, electrons from surface atoms were ejected into the UHV environment where they were detected and their binding energy calculated. The binding energy of the elected electron can be calculated by equation **3** shown below:

$$E_b = E_{hv} - E_k - W_m \qquad \textbf{(3)}$$

In which E_b is the binding energy of the electron, E_{hv} is the energy of the photons, E_k is the kinetic energy of the electron, and W_m is the work function of the instrument. As each element has an identified binding energy, a survey scan ranging from 0 to 1200 eV can be used to measure the elemental composition of the sample. This makes XPS a useful tool in detecting functionalities on the surface of carbon nanomaterials. For example, Shen and co-workers[123] have functionalized rGO with amino groups and the successful attachment of these amino groups were confirmed by the N1s peaks at 396 - 440 eV. However, survey scan cannot be used to identify the chemical state of elements. In this case, high-resolution scans toward specific ranges are necessary. As shown in Figure **10b**, the N1s peak can be de-convoluted into two peaks corresponding to pyridinic (398.3 ± 0.2 eV) and primary amine (399.5 ± 0.2 eV), environments respectively, which can be attributed to the covalent interaction. The C-N group shown in the C1s peak also indicated the formation of covalent bonds between the carbon

matrix and the functional groups.
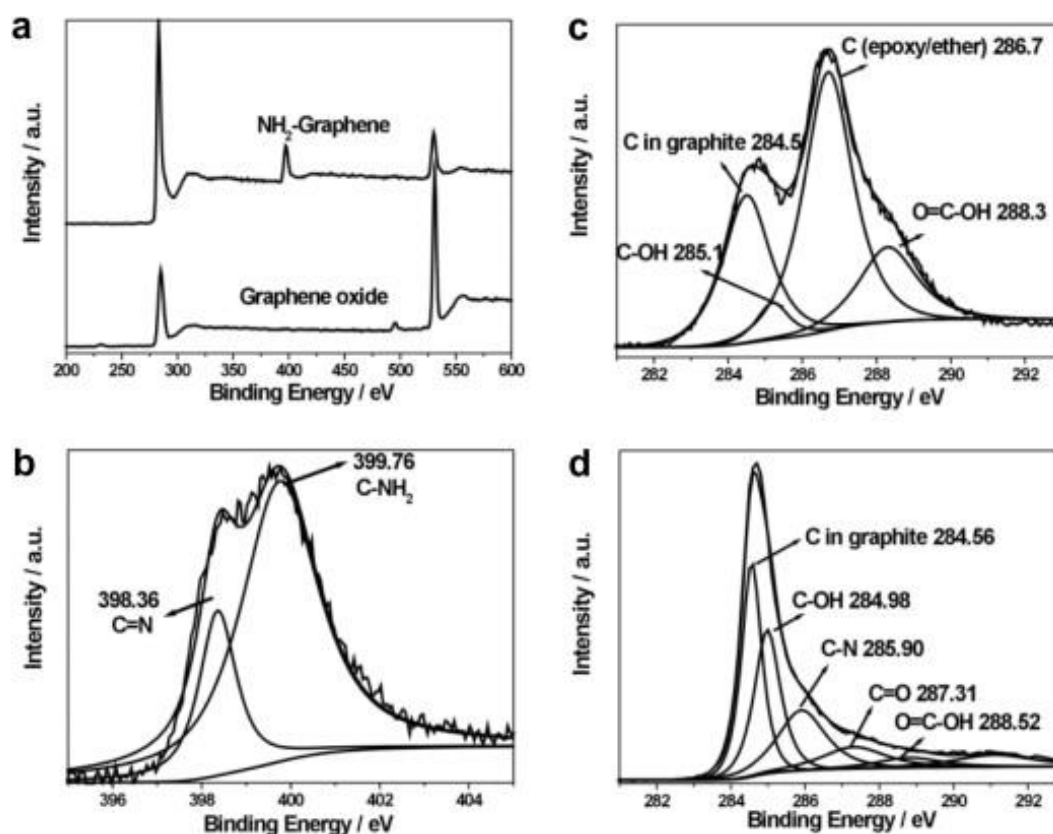
Figure 10 Survey XPS spectra for NH_2 modified graphene and GO; (b) N1s spectrum of NH_2 modified graphene; (C) C1s spectrum of GO; and (d) C1s spectrum of NH_2 modified graphene. Reproduced with permission from ref 123. Copyright 2011 Published by Elsevier Ltd.

1.4.4 UV-Vis Spectrophotometer

UV-Vis Spectroscopy is an absorption spectroscopy working in the ultraviolet-visible spectral region and can give information of the structure of molecules. Under the irradiation of ultraviolet or visible light, the π-electrons or non-bonding electrons (n electrons) of the molecules can be excited to higher anti-bonding orbitals after absorbing energy from the light. This excitation can be reflected by the signal of absorbance (or light transmittance), which is a function of the wavelength of the light.
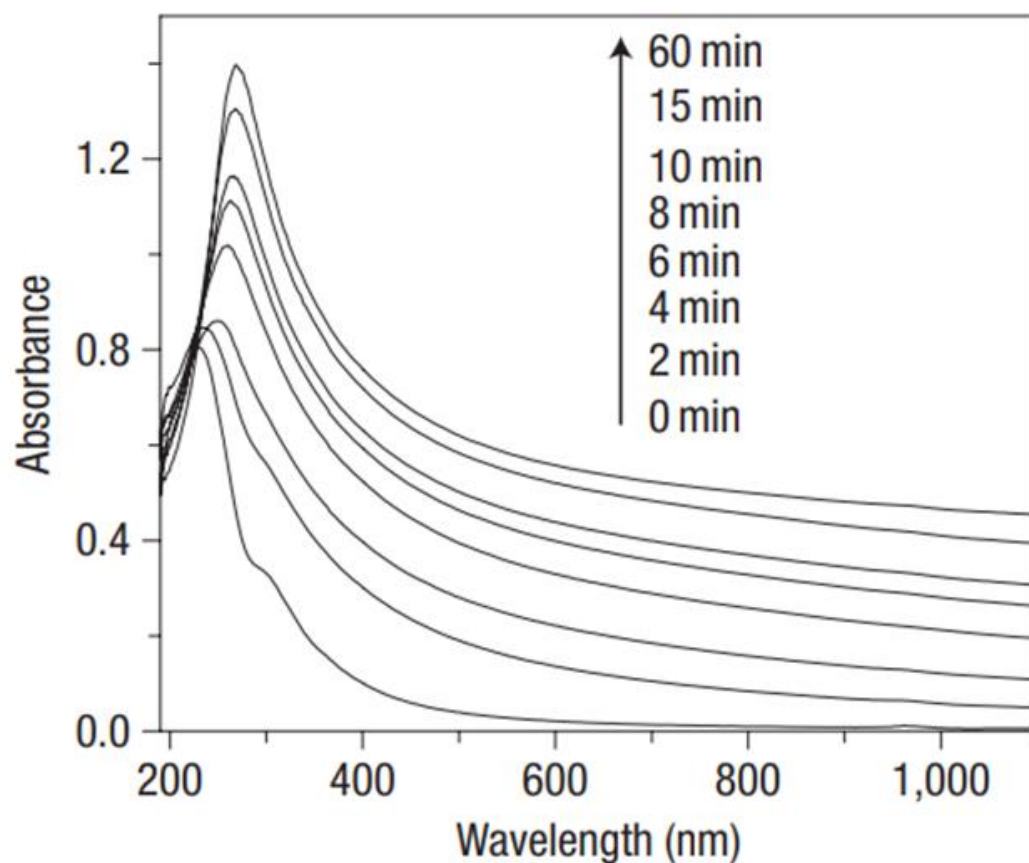
Figure 11 UV-Vis spectra of GO samples over reduction process. Reproduced with permission from ref 124. Copyright 2008 Nature Publishing Group.

UV-Vis spectra have been used as a tool to monitor the reduction process of rGO[124]. As shown in Figure **11**, the main featured peak of GO dispersions is centered at ~231 nm, this peak is attributed to the π-π^* transition from the aromatic backbone. This peak gradually redshifts to ~270 nm when the degree of reduction is increased. And the absorption in the whole region (> 231 nm) was enhanced during the reduction process, indicating the conjugated structure of the carbon matrix was restored over the reaction. The UV-Vis spectra can also be used to evaluate the concentration of graphene dispersion. The concentration of graphene in diluted dispersion can be found from Lambert-Beer's law and can be calculated by equation **4** shown below:

$$A = cl\alpha_{<660>} \tag{4}$$

Where A is the absorbance, c is the concentration of graphene, l is the path length and

$\alpha_{<660>}$ is the molar extinction coefficient at 660 nm. This law has been used to measure the

concentration of graphene or functionalized graphene dispersed in various solvents[59, 60].

1.5 Project Aims

Graphene is a wonder material with fantastic electrical and thermal properties, which

has a wide range of potential applications. The surface modification is essential in graphene

chemistry as it can attach various functionalities onto the graphene surface and make

graphene practically useful for specific applications. Over the past few years, tremendous effort

has been invested in the functionalization of graphene with most research focused on

graphene oxide (GO) or reduced graphene oxide (rGO) based materials. The surface

modification of pristine graphene remains a challenge. However, compared with GO and rGO,

pristine graphene possess the intrinsic advantages of graphene such as a lower density of

defects, a higher electrical and thermal conductivity and impressive strength. Consequently, it

is more important to find a versatile approach to functionalize pristine graphene. Recently,

potassium graphite intercalated compounds (GICs) have attracted much interest as potassium

metal can active pristine graphene by electron doping. The negatively charged carbon layers

are highly reactive towards electrophile-type functionalities such as diazonium compounds.

In this study, we have prepared potassium GICs and functionalized them by utilizing

electrophile type regents - benzyl bromides and diazonium compounds. The GICs were

prepared from two kinds of graphite: 1) 325 mesh natural graphite flakes (≤ 45 μm) and 2)

natural graphite powder with small lateral size (≤ 5.2 µm). The effect of lateral size of graphite towards the degree of intercalation was studied by Raman spectroscopy and powder XRD. Subsequently, various benzyl bromides and diazonium salts were used for the functionalization of the GICs and the degree of the functionalization was investigated by Raman spectroscopy, statistical Raman spectroscopy, and TGA. The functionalities on the surface of graphene were further detected by XPS. Finally, the functionalized graphene samples attached with carboxyl groups were decorated with gold nanoparticles and the morphology of the hybrids was investigated by TEM.

Chapter 2: Preparation and Characterization of Potassium Graphite Intercalation Compounds (GICs)

2.1 Introduction

Graphite Intercalation Compounds (GICs) are complex materials having a formula of CX_n where the ion X_n^+ or X_n^- is intercalated between the oppositely charged carbon layers. GICs have been the subject of intense research since the 1970s due to their unique structure and interesting properties such as excellent electrical conductivity [125] and superconductivity [126]. As one of the most widely studied GICs, potassium GICs have attracted significant attention since the discovery of graphene in 2004. This can be attributed to two reasons: 1) the intercalation of potassium can activate the graphene. The potassium metal can act as an electron donor and the intercalation can initiate the charge transfer between potassium and graphite to produce negatively charged carbon layers. These electron-doped carbon layers are recognized as strong reducing agents and are more reactive towards electrophile type functionalities compared with pristine graphite. This feature can be used to address the issue of high chemical inertness of graphite during functionalization. For instance, Hirsch and co-workers[127] reduced graphite by mixing graphite powder with a Na/K alloy dispersion in di-methyl ether (DME) to form intermediate GICs. Subsequent quenching with 1-iodohexane formed alkylated graphene. More recently, a study carried out by Ruoff and co-workers[128] involved a similar approach by immersing CVD grown graphene in a Na/K alloy dispersion in tetrahydrofuran (THF). The graphene was electron doped by the alloy dispersion and various electrophilic aryl as well as alkyl halides were used as the quenching chemicals. It was found that different functionalities

have different reactivity, with the iodides showing the highest reactivity towards functionalization. 2) Unlike other GICs which can only produce expanded graphite or few layer graphene[129, 130], potassium GICs can be fully exfoliated into single-layer graphene in aprotic solvents such as THF and methyl-2-pyrrolidinone (NMP)[131]. As aforementioned, the intercalation can cause charge transfer between the carbon matrix and potassium and the π-π interaction between individual carbon layers will be replaced by electrostatic repulsive-force. This can help to facilitate the exfoliation of carbon layers in liquid media and prevent their re-aggregation once they have been exfoliated. The exfoliated negatively charged carbon layers can be stabilized by counter ions (K⁺). After a high-speed centrifugation process to remove insoluble materials, graphenide solution containing single-layer or few-layer charged graphene can be obtained. This negatively charged graphene has small lateral size[132] (50-400 nm), high specific area, and a high reactivity towards electrophile type functionalities. For example, Alain Pénicaud and co-workers[133] have quenched graphenide solution with nickel cations to form Ni nanoparticle decorated graphene. The UV-Vis spectroscopy and XPS measurement revealed that the nickel cations were reduced by the negative charge of the graphenide solution.

There are factors that can affect the reactivity of the GICs, including the potassium concentration of the GICs and the lateral size of initial graphite. It was found by Hirsch's group[134] that the highest ordered GICs of potassium KC_8, where the molar ratio of potassium to carbon is 1:8, could reach a high degree of covalent functionalization. Potassium concentration below this value leads to a decreased degree of functionalization while further increasing the concentration of potassium has little effect in terms of functionalization. This can be attributed to the fact that no more K can react with graphite above this ratio. A further study conducted

by the same group[135] pointed out that graphite with smaller lateral size was more easily functionalized as there were more edges exposed to the reactive species.

In the work described here two kinds of natural graphite with different lateral sizes will be used for the preparation of stage 1 potassium GICs. The quality of the raw materials as well as the stage number of the prepared GICs will be investigated by Raman spectroscopy. The structure of prepared GICs will be characterized by powder XRD.

2.2 Preparation and Characterization of Potassium GICs

In the preparation of KC_8, two kinds of graphite were selected as the starting materials - 325 mesh natural graphite flakes and Micrograft natural graphite powder. The 325 mesh graphite flakes have a main lateral size less than 45 μm while the Micrograft natural graphite powder has a smaller lateral size (90% of the flakes ≤ 5.2 μm). The latter was labeled as "S-Graphite" in the following discussion. Raman spectra (Figure **12a, b**) showed these two kinds of graphite have three featured peaks: a D band (1349 cm^{-1} for 325 mesh graphite and 1352 cm^{-1} for S-Graphite), a G band (1580 for 325 mesh graphite and 1581 cm^{-1} for S-Graphite), and a 2D band (2713 cm^{-1} for 325 mesh graphite and 2709 cm^{-1} for S-Graphite).
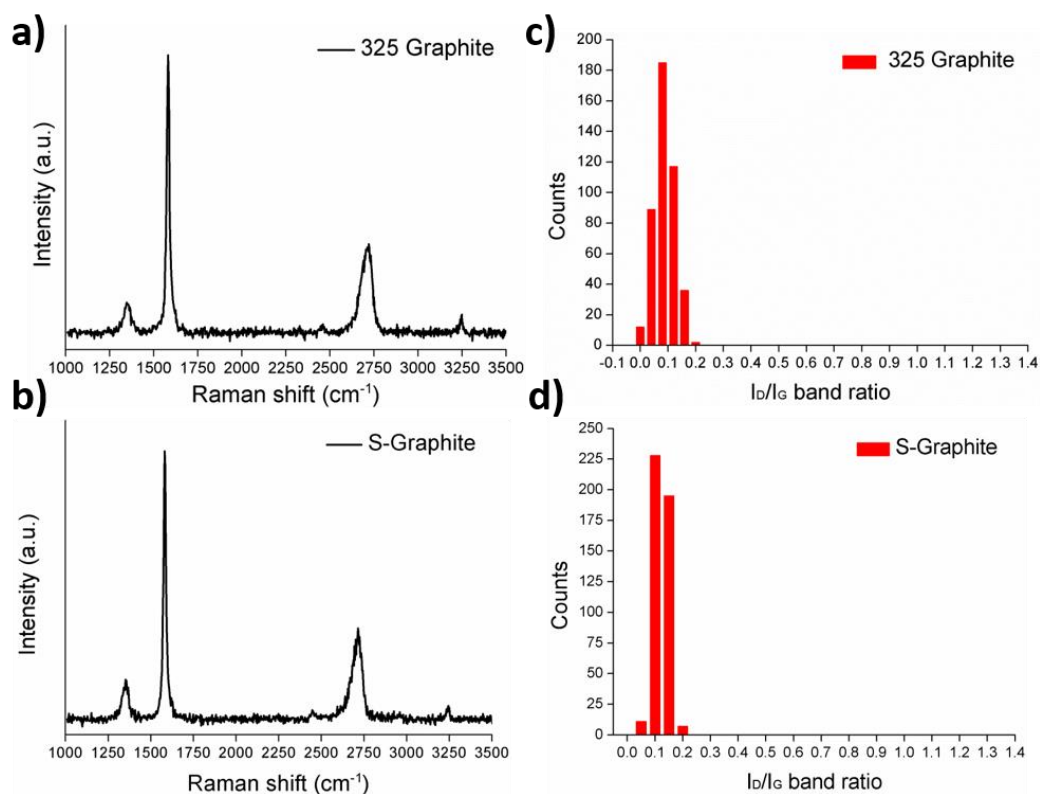
Figure 12 a, b) Raman spectra of 325 mesh graphite and S-Graphite; c, d) histogram of I_D/I_G ratio of 325 mesh graphite and S-Graphite.

Statistical Raman (Figure **12c, d**) was conducted for these two samples and the result shows that both kinds of graphite have low density of defects, reveled by a small value of I_D/I_G ratio (0.11±0.036 for 325 mesh graphite and 0.15±0.023 for S-Graphite).

The fabrication of the GICs was carried out following the liquid phase method reported in the literature[132]. Due to the highly reactive character of potassium metal, the experiment was conducted inside a nitrogen filled glove box (H_2O < 10 ppm, O_2 < 10 ppm). Typically, a specific quality of potassium and graphite were mixed in a glass vial, the molar ratio of potassium and carbon was 1:8. The vial was then heated up to 200 °C on a heating plate.
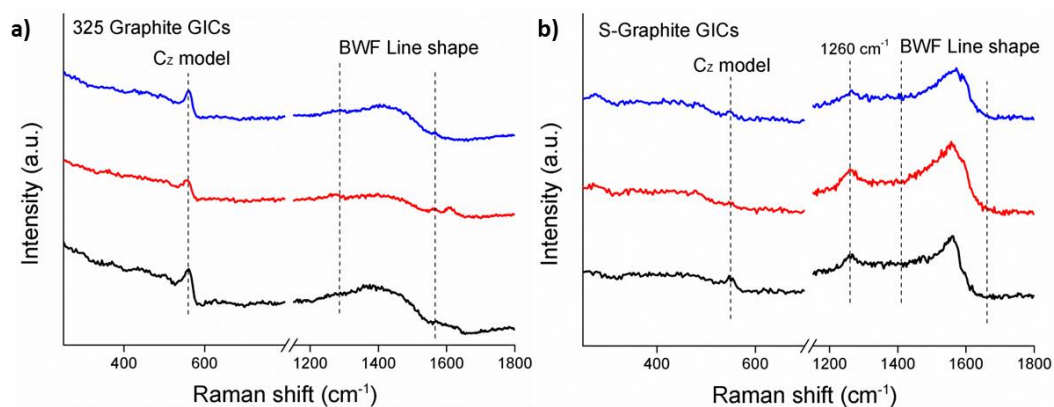
Figure 13 Raman spectra of potassium GICs prepared from 325 mesh graphite (a) and S-Graphite (b).

The volume of the powder was expanded during heating and the color of the powder was turned from black to golden yellow, indicating the successful intercalation of potassium. After 4 hours of heating the powder was cooled down to room temperature. A small quantity of the GICs powder was sealed in a cuvette inside the glove box and was taken out for further characterization. Raman spectroscopy was used to investigate the stage number of the GICs. As shown in Figure **13a**, 325 mesh graphite GICs exhibited characteristic features of a stage 1 GICs with the C_z mode at 560 cm^{-1}. This mode corresponds to the M point of the graphene Brillouin zone, and it becomes Raman active when high intercalation levels are achieved[136]. A broad Breit-Wigner-Fano (BWF) line-shape was also found between 1400 cm^{-1} and 1600 cm^{-1}, which usually indicates the formation of KC_8[137]. As for the S-Graphite GICs (Figure **13b**), a Breit-Wigner-Fano line shape was also found between 1440 cm^{-1} to 1700 cm^{-1}, revealing the formation of GICs. However, no obvious C_z mode was found around 560 cm^{-1}. This may due to the relatively low degree of intercalation of the GICs. The mode observed around 1260 cm^{-1} could be attributed to intrinsic disorder present on the graphite rather than pristine GICs[136]. This mode is not obvious in the spectra for 325 mesh graphite GICs, which matches the I_D/I_G ratio distribution of these two kinds of graphite.
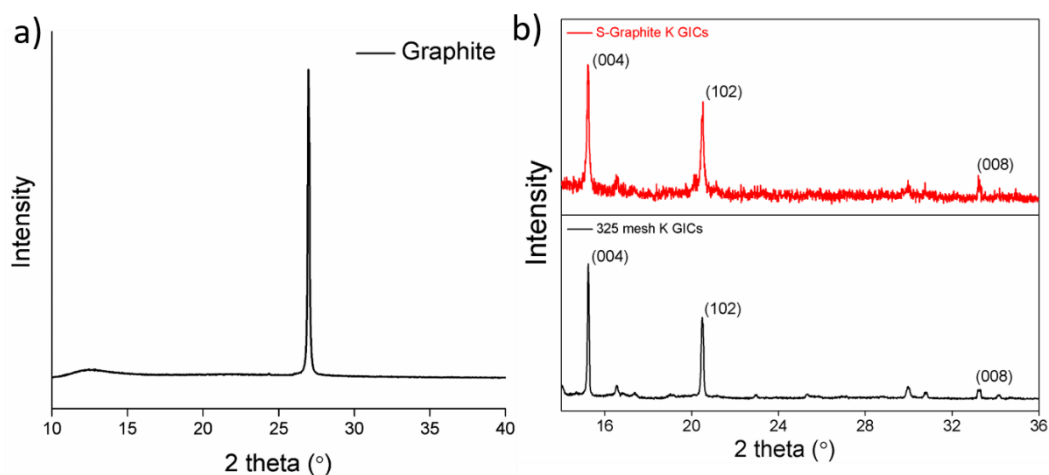
Figure 14 Powder XRD of graphite (a) and potassium GICs prepared from 325 mesh graphite (b below) and S-Graphite (b above).

As shown in Figure **14a**, the powder XRD pattern of 325 mesh graphite showed a characteristic peak located at $2\theta = 26.9°$. This peak represents (002) reflection of graphite and disappears after potassium intercalation (Figure **14b**), indicating the change of interlayer distance after intercalation. Besides, characteristic peaks at $2\theta = 15.3°$ and $33.2°$ were observed in these two GICs. These peaks represent the (004) and (008) diffraction lines of crystalline KC_8 samples. This result confirmed that both of these two GICs contained stage 1 GICs.

2.3 Conclusions

In summary, potassium GICs has been successfully prepared by using two kinds of graphite as starting materials. Raman and Powder XRD measurements were used to characterize the potassium GICs. It was found that both 325 mesh graphite and S-graphite can be intercalated by potassium and the final products contained stage 1 GICs – KC_8. Compared with GICs made from S-Graphite, the GICs prepared from 325 mesh graphite can achieve a higher degree of intercalation as well as crystallinity.

Chapter 3: Functionalization of Graphene via Diazonium Approach

3.1 Introduction

Over the past decades, the diazonium chemistry in graphene functionalization has been intensely studied and several kinds of diazonium salts such as 4-nitrobenzene diazonium tetrafluoroborate (4-NBD), 4-bromobenzene diazonium tetrafluoroborate (4-BBD), 4-propargyloxybenzene diazonium tetrafluoroborate (4-PBD), as well as 4-tert-butylphenyldiazonium tetrafluoroborate (4-BPD) have been used for graphene modification[86]. Although these diazonium salts showed adequate reactivity towards graphene functionalization, it is still difficult to overcome the high inertness of graphene, which can limit the degree of functionalization. Consequently, it is of great importance to find a more suitable and controllable reaction condition. Over the past few years, the functionalization of potassium GICs by diazonium chemistry has attracted great research interest. As the functionalization of graphene is initialized by the transfer of delocalized electron from conjugated carbon matrix to diazonium compounds, the electron doped carbon layer in potassium GICs should be more reactive towards diazonium salts compared with pristine graphene and the degree of functionalization could be further improved. Besides, the enhanced reactivity of carbon sheets can be functionalized by a wider range of functionalities. For example, it was difficult to modify pristine graphene with sophisticated functionalities such as porphyrin groups, which can be achieved after potassium intercalation[138].

In this project, the potassium GICs prepared from two kinds of graphite will be

functionalized by three diazonium salts: 4-carboxybenzene diazonium tetrafluoroborate (4-CBD), 4-fluorobenzene diazonium tetrafluoroborate (4-FBD), and 4-nitrobenzene diazonium tetrafluoroborate (4-NBD). The 4-CBD and 4-FBD were synthesized in the lab following literature procedures[139], while 4-NBD was purchased from Sigma Aldrich. The synthesized diazonium salts were characterized by FT-IR, mass spectrometry and NMR. The functionalization of the GIC samples were characterized by Raman spectroscopy, Statistical Raman spectroscopy, and TGA and the reactivity of these three diazonium compounds compared. The 4-FBD functionalized sample was further characterized by XPS as the fluorine can be easier to be recognized.

To the best of our knowledge, the modification of potassium GICs by 4-carboxybenzene diazonium tetrafluoroborate (4-CBD) has not been reported, despite the carbonyl group's suitability for a range of diverse applications. For example, carboxyl group functionalized graphene can be further attached with glucose oxidase containing amines groups to make biosensors. The 4-CBD functionalized sample was further decorated with amine modified gold nanoparticles and will be discussed in detail in chapter 5.

3.2 Results and discussion

The functionalization of GICs by 4-FBD was conducted inside the glove box. Typically, 51 mg of 325 mesh GIC was dispersed in 25 ml of dry THF in a sample vial. The dispersion was sonicated at 200 W for 2 mins for further exfoliation of the GICs.
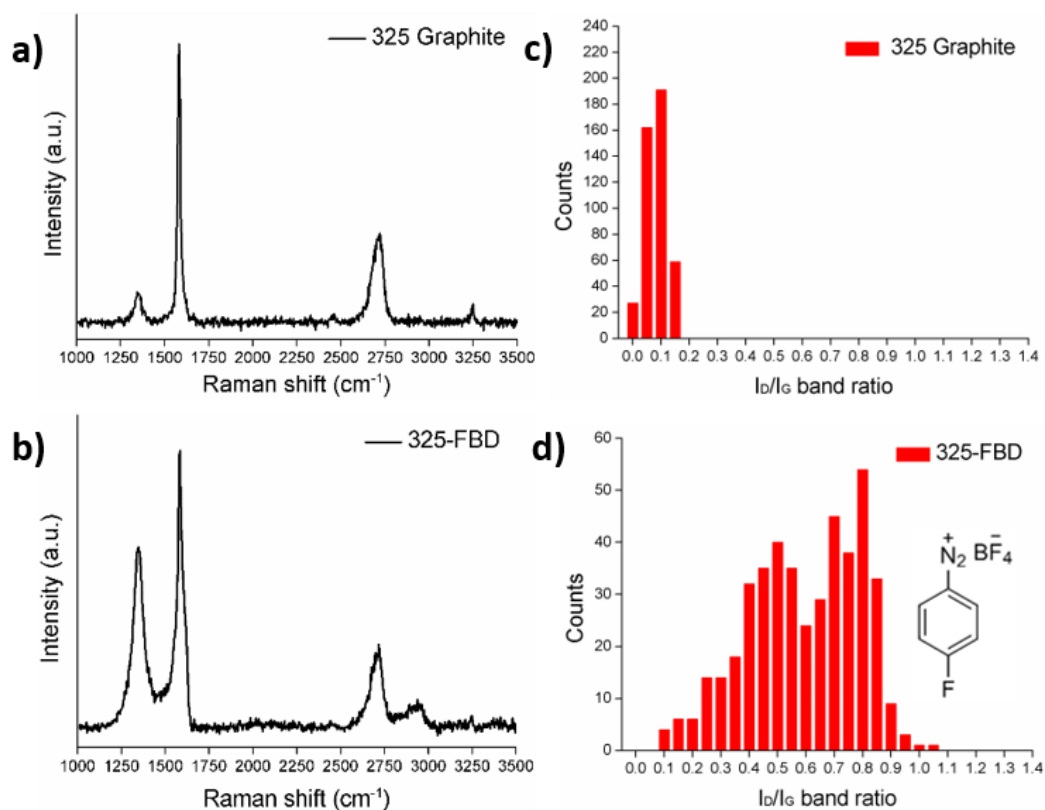
Figure 15 a, b) Raman spectra of 325 mesh graphite and 325-FBD sample; c, d) histogram of I_D/I_G ratio distribution of 325 mesh graphite and 325-FBD sample.

Subsequently, 1.5 mmol of 4-FBD was added to the GICs dispersion under vigorous stirring. During the adding of the diazonium compound, the GICs were quenched immediately accompanied by an obvious color change from golden yellow to black. A violent release of nitrogen bubbles was observed, indicating the rapid formation of aryl radicals. The reaction was maintained for 24 hours under stirring. Then the sample was taken out from the glove box and washed completely with acetone and water to remove unreacted reagents and potassium species. Raman spectra (Figure **15b**) of the 4-FBD functionalized sample showed three featured peaks: A D band at 1346 cm^{-1}, a G band at 1583 cm^{-1} and a 2D band at 2706 cm^{-1}. A much-enhanced D band as well as a new peak (D+D' model) centered at 2937 cm^{-1} were observed, this could be attributed to the hybridization of in-plane carbon atoms transferred

from sp^2 to sp^3. Statistical Raman Spectra (Figure **15d**) further confirmed that the D band was significantly enhanced, revealed by a higher value of I_D/I_G ratio (0.62±0.20) compared with 325 mesh graphite (0.11±0.036).
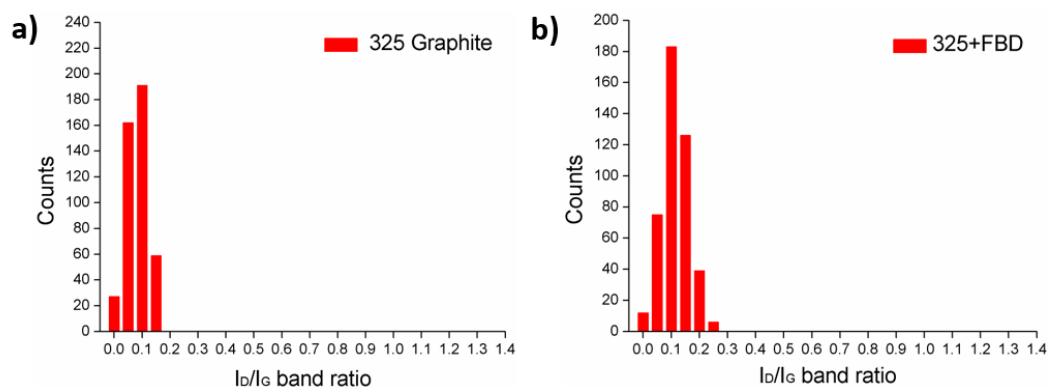
Figure 16 Histogram of I_D/I_G ratio distribution of 325 mesh graphite (a) and 325+FBD sample (b).

For investigating the function of potassium intercalation in this process, a control experiment was carried out by directly mixing 4-FBD and graphite under the same conditions and the sample was labeled as 325+FBD. Statistical Raman (Figure **16b**) showed that after reaction, the I_D/I_G ratio of the sample experienced a negligible increase from 0.11±0.036 to 0.14±0.048, which is much lower than that of 325-FBD. This result indicated that potassium intercalation played a very important role in activating the carbon layers and making them more reactive towards radical attacking. XPS measurement was carried out to detect the functionality on the surface of the sample. The XPS F1s spectra (**Figure 17**) revealed clear presence of fluorine in both 325-FBD and 325+FBD samples. This indicated the successful attachment of functional groups by mixing 4-FBD with GICs and pristine graphite.
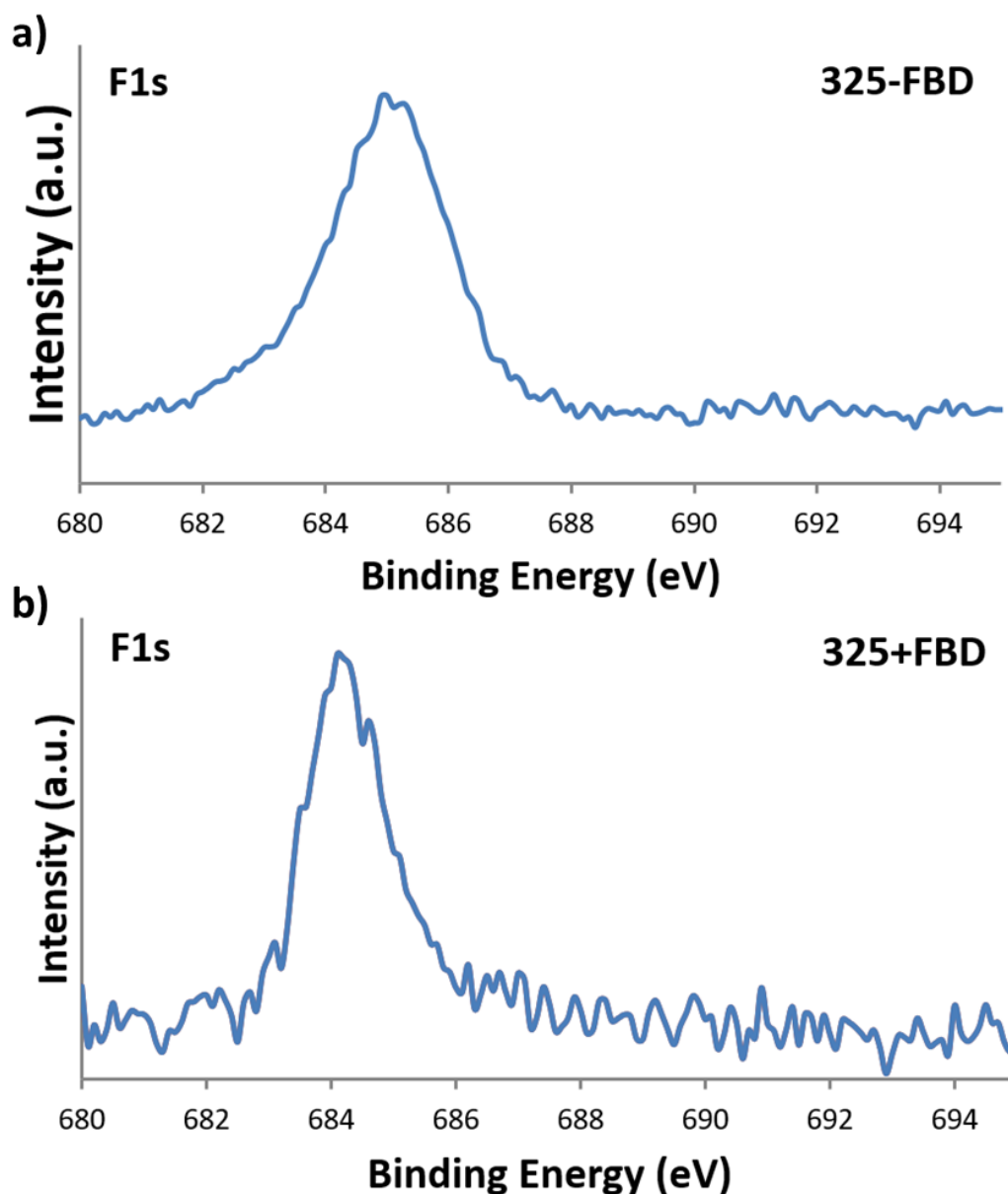
Figure 17 XPS F1s spectra of 325-FBD and 325+FBD samples. (Explain peak position)

Except for 4-FBD, other diazonium salts including 4-CBD and 4-NBD were also used for functionalization under the same reaction condition. As shown in Figure **18a** and **18c**, the Raman spectra for 325-CBD showed a huge and broad D band centered at 1348 cm^{-1}. Similar to 325-FBD sample, a D+D' model was observed at 2924 cm^{-1}. By contrast, no identifiable D+D' model was found for 325-NBD sample (Figure **18b**) and the intensity of D band was much lower than that of 325-CBD and 325-FBD (Figure **18d**), this could be attributed to the low reactivity of

4-NBD towards functionalization.
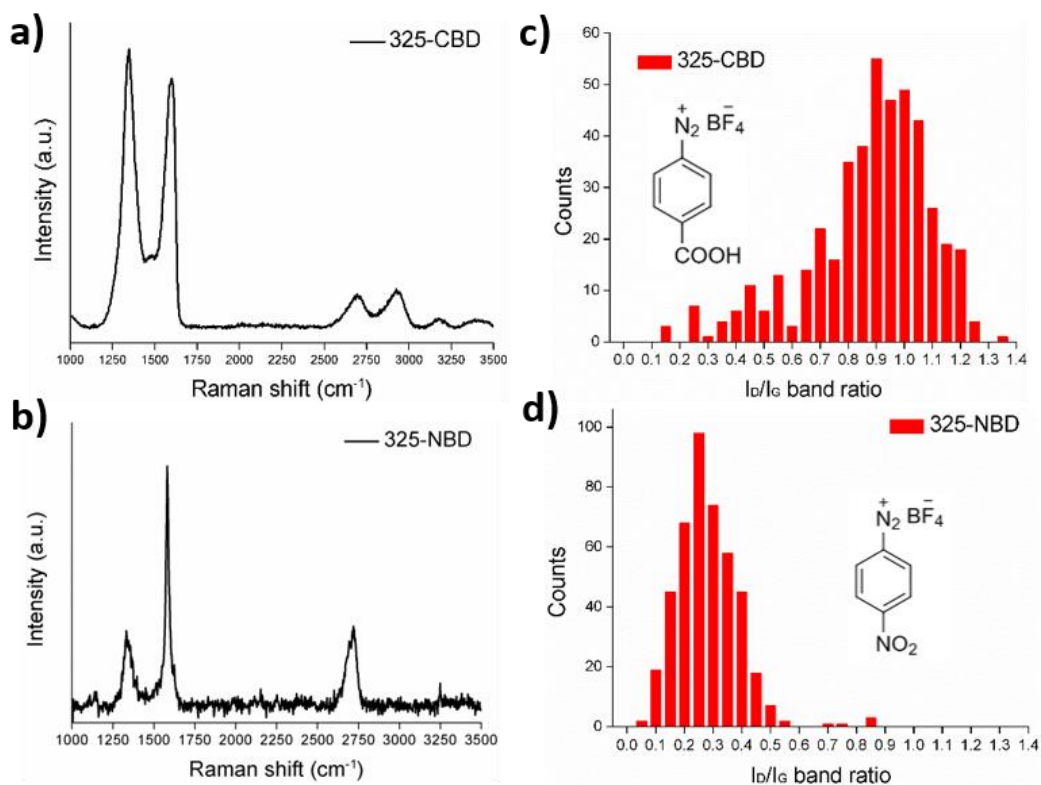
Figure 18 a, b) Raman spectra of 325-CBD and 325-NBD samples; c, d) histogram of I_D/I_G ratio distribution of 325-CBD and 325-NBD samples.

Statistical Raman measurement was also conducted for 325-CBD and 325-NBD samples. The average I_D/I_G ratios of various samples were calculated, and the results were listed in Table **1**. It was found that 325-CBD sample possessed the highest degree of functionalization, revealed by the highest I_D/I_G ratio of 0.90±0.22 and the I_D/I_G for 325-NBD was 0.30±0.11. In general, it can be roughly concluded that the order of functionalization degree was 325-CBD > 325-FBD > 325-NBD.
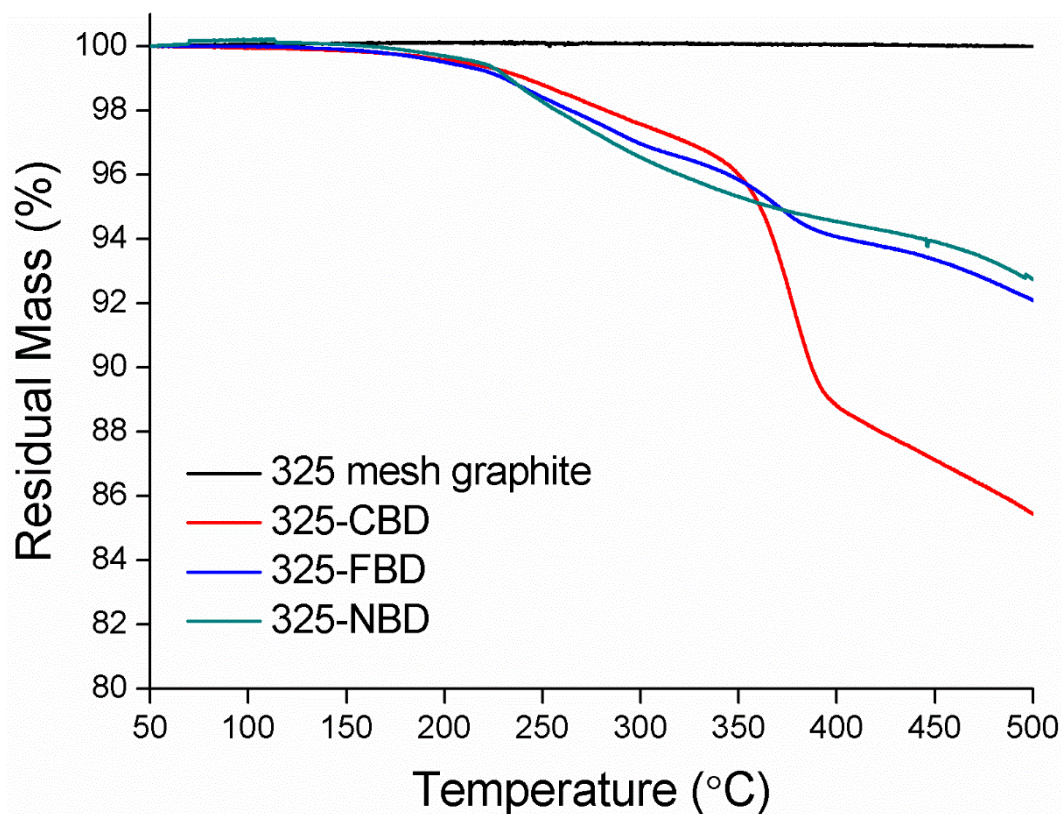
Figure 19 TGA spectra of 325 mesh graphite (black line) 325-CBD (red line), 325-FBD (blue line), and 325-NBD (green line) samples.

To further investigate the degree of functionalization of various samples, a TGA measurement was carried out in a helium atmosphere from room temperature to 500 ℃. For obtaining an accurate value of mass loss, the mass loss before 200 ℃ was ignored as the mass loss in this region is usually attributed to the evaporation of moisture or solvent. As shown in Figure **19**, the pristine graphite showed negligible mass loss (<0.1%) when heated up to 500 ℃ while the mass loss for 325-CBD, 325-FBD and 325-NBD were 14.2%, 7.4% and 6.9%, respectively. The concentration of the functionality C_f was calculated by equation **5** shown below:

$$C_f = \frac{w_f/m_f}{w_r/12} \qquad \textbf{(5)}$$

49

In which w_f is the weight of functionality (mass loss), m_f is the molecular weight of functionality and w_r is the weight of residual carbon materials. The functionality concentration was calculated to be 0.018 per carbon for 325-CBD and 0.010 per carbon for 325-FBD sample. As the $-NO_2$ group on 4-NBD might be reduced to $-NH_2$ group during the reaction[140], the functionality concentration of 325-NBD sample cannot be correctly calculated.

Table 1 Average I_D/I_G Ratio of 325 mesh graphite, 325-CBD, 325-FBD, and 325-NBD samples.

Sample name	I_D/I_G Ratio (average)	Mass loss in TGA (%)	Functionality concentration per carbon
325 graphite	0.11±0.036	<0.1	/
325-CBD	0.90±0.22	14.2	0.018
325-FBD	0.62±0.20	7.4	0.010
325-NBD	0.30±0.11	6.9	/

The GICs prepared from S-Graphite were also functionalized by 4-CBD, 4-FBD and 4-NBD. As shown in Figure **20** and Table **2**, an enhanced D band and I_D/I_G ratio were observed for all functionalized samples, indicating the successful covalent functionalization. Among these functionalized samples, SG-CBD possessed the highest I_D/I_G ratio (0.53±0.035), followed by SG-FBD (0.42±0.024) and SG-NBD (0.25±0.066). Besides, an identifiable D+D' model can be found in the Raman spectra of SG-CBD and SG-FBD samples, which was absent in the spectra of SG-NBD sample. These results further confirmed that 4-CBD possess the highest reactivity towards covalent functionalization of potassium GICs while the 4-NBD has the lowest reactivity.
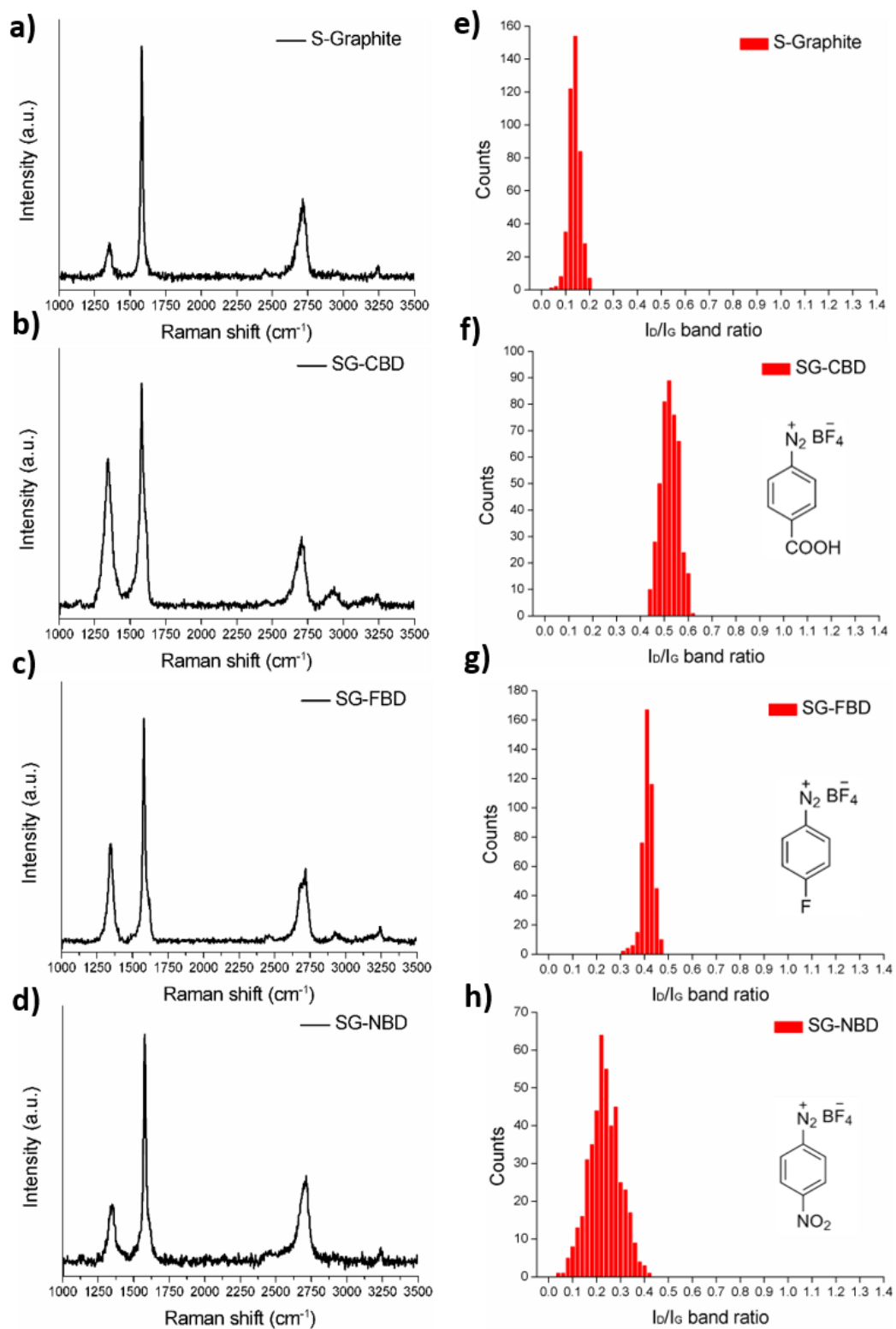
Figure 20 a-d) Raman spectra of S-Graphite, SG-CBD, SG-FBD and SG-NBD samples; e-h) histogram of

I_D/I_G ratio distribution of S-Graphite, SG-CBD, SG-FBD and SG-NBD samples.

It is worth noting that although S-Graphite had a higher intrinsic defect density

compared with 325 mesh graphite, the functionalized S-Graphite GICs possessed a lower I_D/I_G ratio than those of functionalized 325 GICs even when they were functionalized by the same diazonium compound. This could be attributed to that the GICs prepared from 325 mesh graphite had a higher order of intercalation as well as crystallinity thereby the in-plane carbon atoms were more reactive than those of GICs made from S-Graphite.
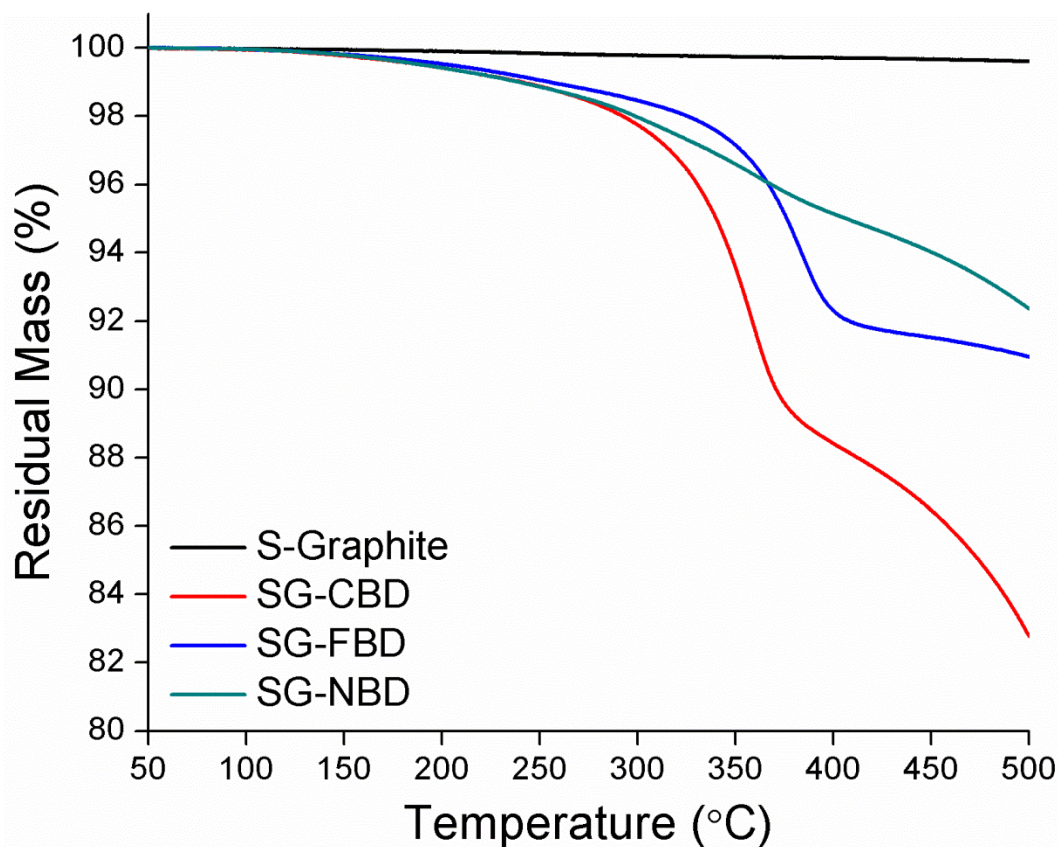
Figure 21 TGA spectra of S-Graphite (black line) and SG-CBD (red line), SG-FBD (blue line) and SG-NBD (green line) samples.

TGA characterization was also conducted for S-Graphite and functionalized S-Graphite GICs samples. As shown in Figure **21**, the pristine S-Graphite showed negligible mass loss when heated up to 500 ℃. Interestingly, though S-graphite GICs derived samples had low degree of in-plane functionalization, the mass loss for SG-CBD, SG-FBD and SG-NBD were measured to be

17.1%, 8.6% and 7.1% at 500 ℃, respectively, which are comparable with that of functionalized graphene derived from 325 mesh GICs. This could be attributed to that the graphite with smaller lateral size has more exposed edges, which possess a higher reactivity than in-plane carbon atoms. As a result, there was more edge functionalization possible for S-Graphite GICs derived samples.

Table 2 Average I_D/I_G Ratio of S-Graphite and SG-CBD, SG-FBD and SG-NBD samples.

Sample name	I_D/I_G Ratio (average)	Mass loss in TGA (%)	Functionality concentration per carbon
S-Graphite	0.15±0.023	<0.1	/
SG-CBD	0.53±0.035	17.1	0.020
SG-FBD	0.42±0.024	8.6	0.012
SG-NBD	0.25±0.066	7.1	/

3.3 Conclusion

In summary, potassium GIC made from 325 mesh natural graphite has been functionalized by various diazonium salts. Raman spectra, TGA and XPS measurement indicated the successfully covalent functionalization. Among these three kinds of diazonium compounds used, 4-carboxybenzene diazonium tetrafluoroborate (4-CBD) had the highest reactivity towards functionalization. Potassium GICs made from S-Graphite was also functionalized with the same diazonium compounds. Raman spectra showed that S-Graphite derived samples had a relatively lower degree of in-plane functionalization. However, TGA measurement showed that the functionalized S-Graphite GICs possessed a comparable overall functionality concentration compared with GICs made from 325 mesh graphite. This could be attributed to

that S-Graphite GICs had more exposed edges than 325 meshed GICs and there is more edge

functionalization present for S-Graphite derived samples.

Chapter 4: Functionalization of Graphene via Benzyl Bromide Approach

4.1 Introduction

Benzyl bromide is often used in organic synthesis to introduce benzyl groups to other moieties as the bromide can act as a good leaving group. Since the benzyl carbocation is relatively stable under reaction conditions and has high electrophilicity, it is reasonable to suspect that benzyl bromide can interacted with negatively charged potassium GICs and achieve the benzylation of graphene.

In this project, the GICs prepared from 325 mesh graphite were functionalized by various benzyl bromides including 4-bromomethyl benzoic acid (4-BBA), 4-fluorobenzyl bromide (4-FBB), and 4-nitrobenzyl bromide (4-NBB). The 325 GICs were selected as the starting materials due to their higher degree of potassium intercalation as well as higher in-plane reactivity toward diazonium compounds. The degree of functionalization of various samples was characterized by Raman spectroscopy, statistical Raman Spectroscopy, and TGA. The functionality will be further detected by XPS measurement.

4.2 Results and discussion

Briefly, inside the glove box, 325 mesh graphite GICs were dispersed in 25 ml of absolute tetrahydrofuran (THF) with an initial concentration of 0.12 mg/ml. The dispersion was sonicated at 200 W for 2 mins for further exfoliation of the GICs. Subsequently, 1.5 mmol of 4-FBB was added to the GIC dispersion under magnetic stirring.
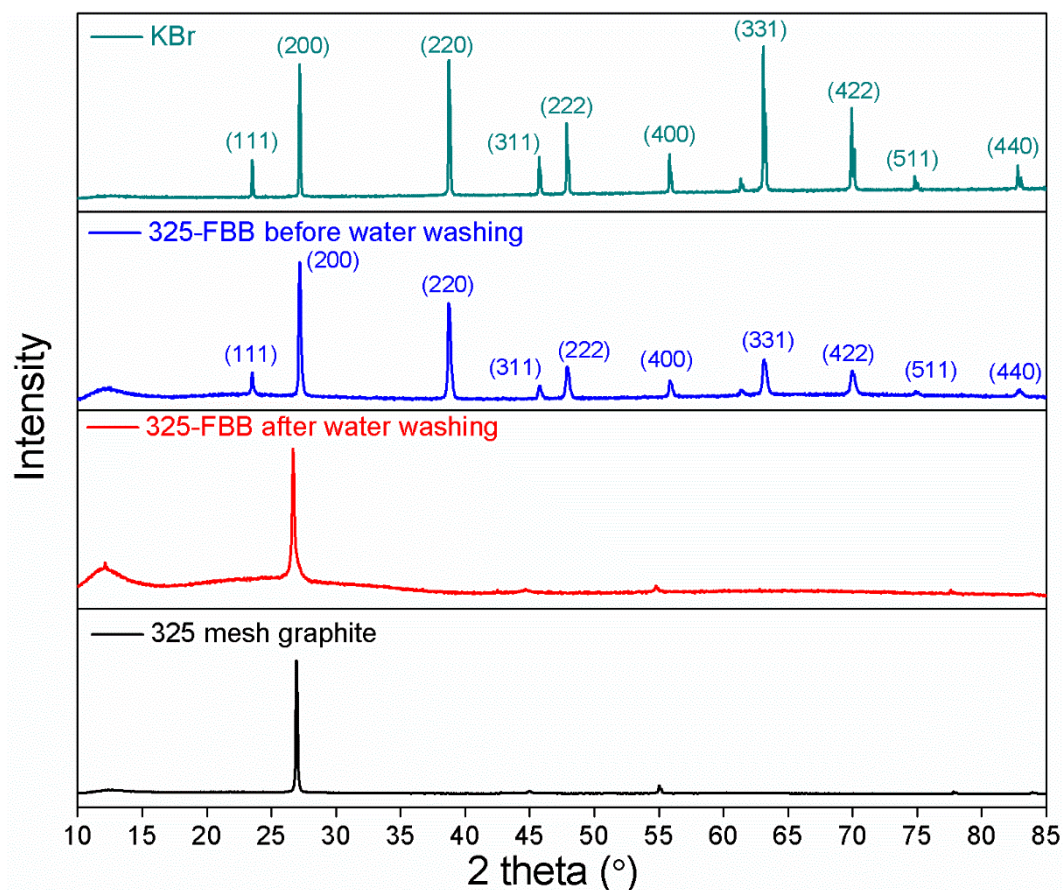
Figure 22 Powder XRD pattern of 325 mesh graphite (black line), KBr (green line), 325-FBB sample before (blue line) and after (red line) water washing.

During the adding of benzyl bromides, the color of the dispersion turned from golden brown yellow to black, indicating successful discharge of the GICs. The mixture was stirred for 24 hours after all the reactant was added. The product was then taken out from the glove box and was further quenched by 1 ml of methanol for complete remove of any residual charge. The product was collected by vacuum filtration and washed with acetone to remove residual reactant and then dried in the oven.
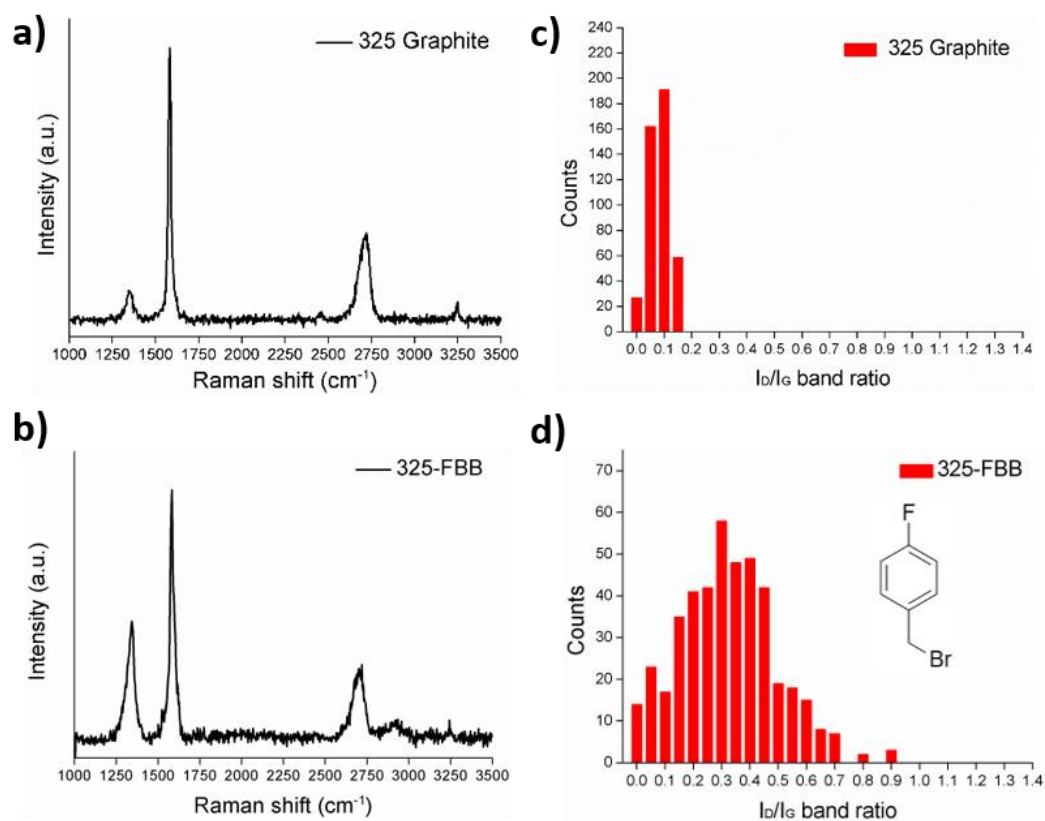
Figure 23 a, b) Raman spectra of 325 mesh graphite and 325-FBB samples; c, d) Histogram of I_D/I_G ratio distribution of 325 mesh graphite and 325-FBB samples.

Powder XRD characterization was conducted to investigate the crystal structure of the functionalized material. As shown in Figure **22**, the sample obtained after acetone washing exhibited featured XRD pattern of potassium bromide, indicating the bromine has successfully left during the reaction and combined with potassium ion to form KBr crystals.
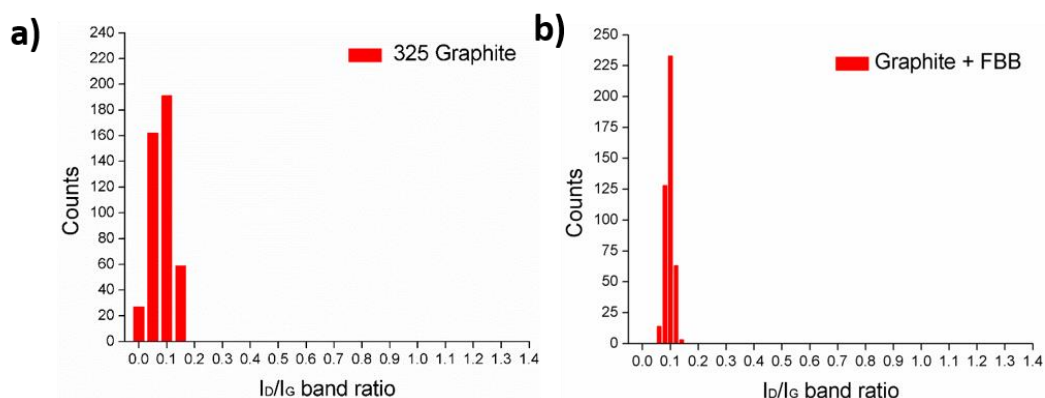
Figure 24 Histogram of I_D/I_G ratio for325 mesh graphite and 325+FBB sample.

After washing with water to remove potassium salts, the featured KBr peaks disappeared. Raman spectra (Figure **23b**) and statistical Raman spectra (Figure **23d**) showed an enhanced D band after functionalization and the I_D/I_G ratio was improved from 0.11±0.036 to 0.35±0.17. Besides, a weak D+D' peak was found at 2923 cm^{-1}, indicating the functional groups were covalently attached onto the surface of graphene. A Control experiment was conducted by directly mixing 4-FBB with graphite in THF inside the glove box and the product was labeled as 325+FBB. Statistic Raman result showed (Figure **24b**) negligible change in terms of I_D/I_G ratio after reaction.

XPS measurement was also carried out to detect the functionality on the surface of the sample. As shown in **Figure 25a**, the XPS F1s spectrum of 325-FBB sample reveals presence of fluorine**.** This indicates the successful attachment of fluorine containing group on graphene surface. By contrast, no F1s peak was found for 325+FBB sample, indicting no reaction or adsorption or of 4-FBB on graphene after washing. This result further confirmed that charged GICs played a key role in functionalization.
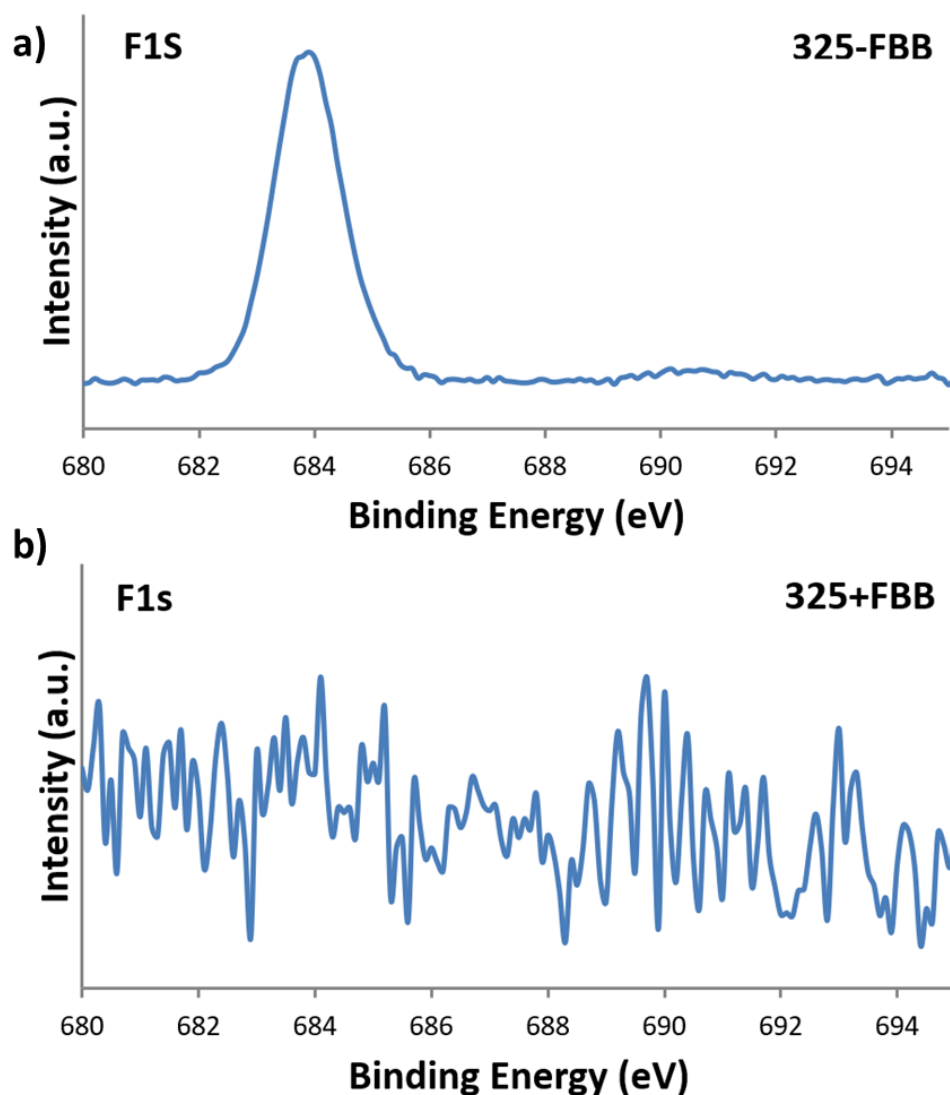
Figure 25 XPS F1s spectra of 325-FBB and 325+FBB samples.

For comparison, 4-bromomethyl benzoic acid (4-CBA) and 4-nitrobenzyl bromide (4-NBB) were also used for functionalization. As shown in Figure **26** and Table **3**, the 325 mesh GIC experienced an enhancement in I_D/I_G ratio after functionalization by 4-CBA and 4-FBB and the values were 0.34±0.16 and 0.19±0.086, respectively. TGA measurement (Figure **27**) showed that 325-CBA, 325-FBB and 325-NBB samples exhibited a mass loss of 9.1%, 7.8% and 5.6% at 500 ℃, respectively, and the functionality concentration was calculated to be 0.0088 per carbon for 325-CBA and 0.0095 per carbon for 325-FBB. Combining the TGA results and Raman

spectra, it can be concluded that 4-bromomethyl benzoic acid and 4-fluorobenzyl bromide have comparable reactivity towards functionalization while 4-nitrobenzyl bromide possessed the lowest reactivity.
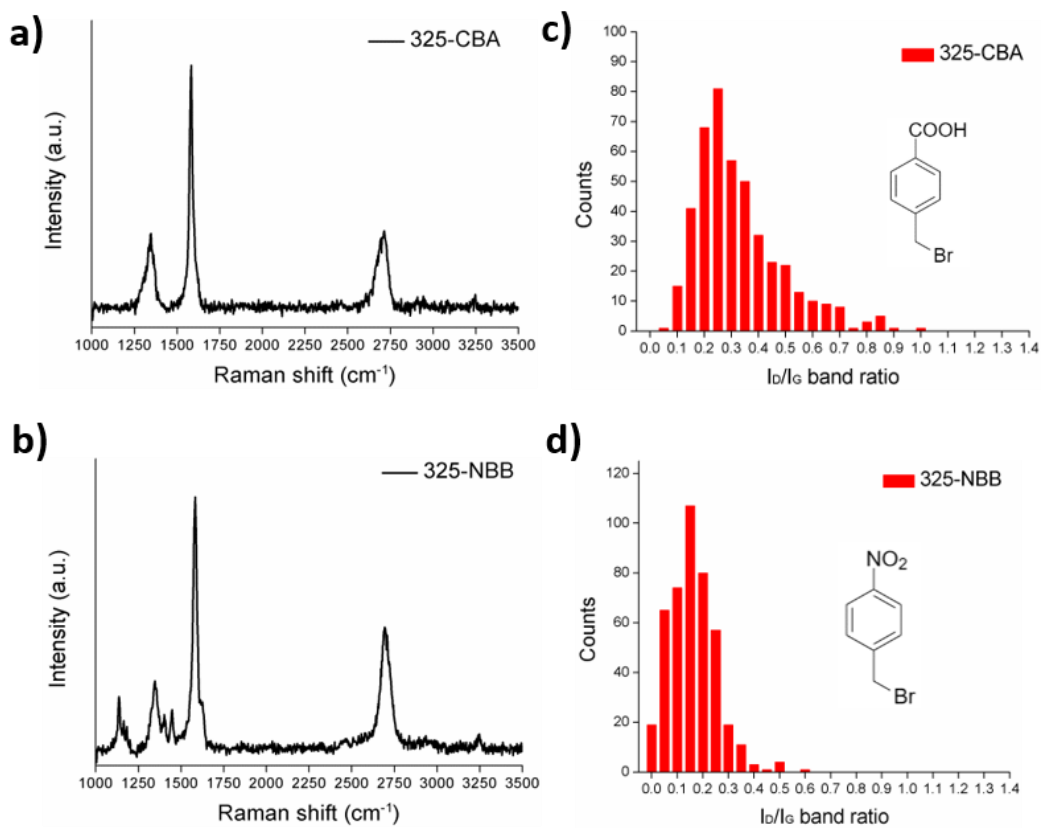
Figure 26 a, b) Raman spectra of 325-CBA and 325-NBB sample; c, d) Histogram of I_D/I_G ratio of 325-CBA and 325-NBB sample.

The efficiency of functionalization via benzyl bromides was lower than that of the diazonium approach. This was revealed by a lower I_D/I_G ratio as well as a lower functionality concentration of benzyl bromides functionalized samples compared with diazonium compounds functionalized samples.
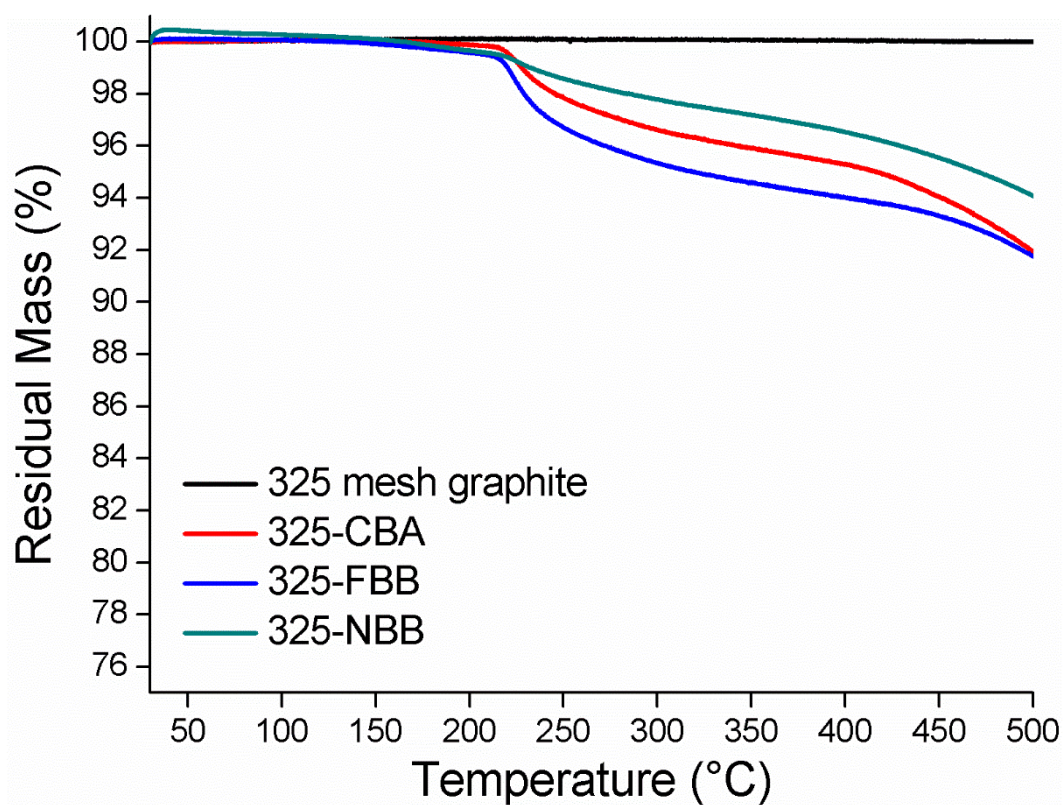
Figure 27 TGA spectra of 325 mesh graphite (black line), 325-CBA (red line), 325-FBB (blue line) and 325-NBB (green line) samples.

Table 3 Average I_D/I_G Ratio of 325 mesh graphite and 325-CBA, 325-FBB, and 325-NBB samples.

Sample name	I_D/I_G Ratio (average)	Mass loss in TGA (%)	Functionality concentration per carbon
325 mesh graphite	0.11±0.036	<0.1	/
325-CBA	0.34±0.16	9.10	0.0088
325-FBB	0.35±0.17	7.80	0.0095
325-NBB	0.19±0.086	5.60	/

4.3 Conclusion

In summary, potassium GIC made from 325 mesh natural graphite has been functionalized by various benzyl bromides. Raman spectra, TGA and XPS measurement indicated successfully covalent functionalization. It was also found that the charged graphene was essential for the reaction to take place. Among the benzyl bromides studied, 4-bromomethyl benzoic acid (4-CBA) and 4-fluorobenzyl bromide (4-FBB) had comparable reactivity towards functionalization while 4-nitrobenzyl bromide (4-NBB) had the lowest reactivity. It can also be concluded that diazonium compounds possess higher reactivity than benzyl bromides.

Chapter 5: Decorating Functionalized Graphene with positively charged gold nanoparticles (Au-NPs)

5.1 Introduction

Over the past few years, nanoparticles decorated graphene, in particular Au-NPs/graphene hybrids have attracted much attention in diverse areas such as catalysis[141, 142] and bio-sensors[143, 144]. This could be attributed to the high specific area as well as the high conductivity of graphene, which can help the hybrid reach up to a high density of active sites and a high charge transfer rate. However, one of the drawbacks of pristine graphene is the lack of an anchor site, which can interact with metal nanoparticles thus preventing their re-aggregation. The surface modification of graphene can introduce functional groups on the surface of graphene, which can anchor the nanoparticles to achieve a good distribution of nanoparticles.
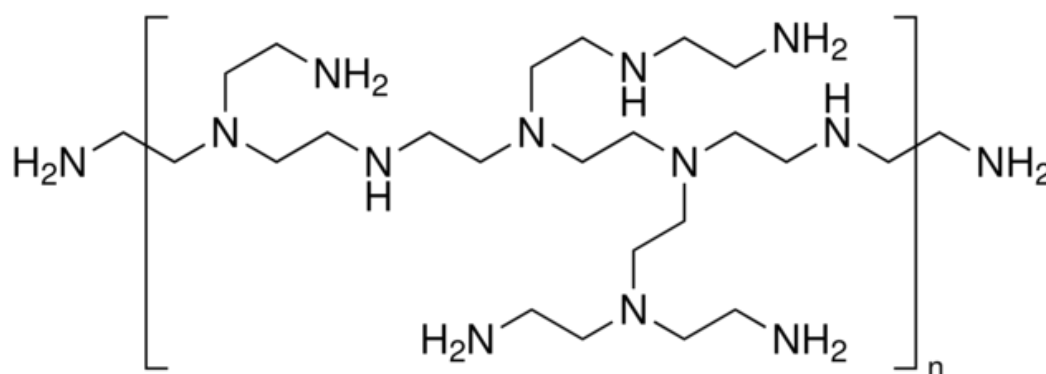
Figure 28 Structure of PEI molecule.

In our process, amine group functionalized positively charged Au-NPs were synthesized via reducing gold chloride hydrate by Poly(ethyleneimine) (PEI) (Figure **28**). The as prepared

Au-NPs were used to decorate 325 meshed graphite, 325-CBA and 325-CBD samples.

The synthesized Au-NPs were characterized by UV-Vis to confirm the formation of Au phase nanoparticles. The decorated graphite/functionalized graphene samples were characterized by TEM to confirm the successful decoration of Au-NPs. The added benefit of decorating functionalized graphene with Au-NPs, and comparing with control samples, one can indirectly infer the presence of functional groups as well as their location and distribution.

5.2 Results and discussion
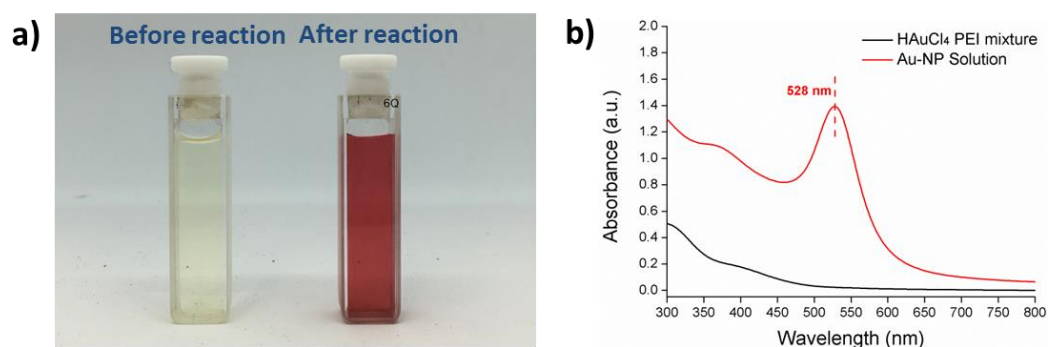
Figure 29 a) Image of PEI and HAuCl$_4$ mixture before (left) and after (right) reaction; b) UV-Vis spectra of PEI and HAuCl$_4$ mixture before (left) and after (right) reaction.

The amine functionalized Au-NPs were prepared by following the literature[145]. Typically, to a 40 ml of polyethyleneimine solution (0.3 g PEI) was added 1 ml of 10 mg/ml of gold chloride hydrate solution. The PEI molecule contains amine groups and can act as both reducing agent and stabilizer. The pH of the system was adjusted to 3.5 by adding diluted hydrochloric acid and the reaction was maintained under stirring for 12 h. During this process the color of the mixture turned from faint yellow to wine red (Figure **29a**), indicating the formation of Au-NP colloidal solution. The UV-Vis spectrum of the product solution exhibited a

plasmon peak at 528 nm (Figure **29b**), which is a characteristic for spherical Au-NPs[146].
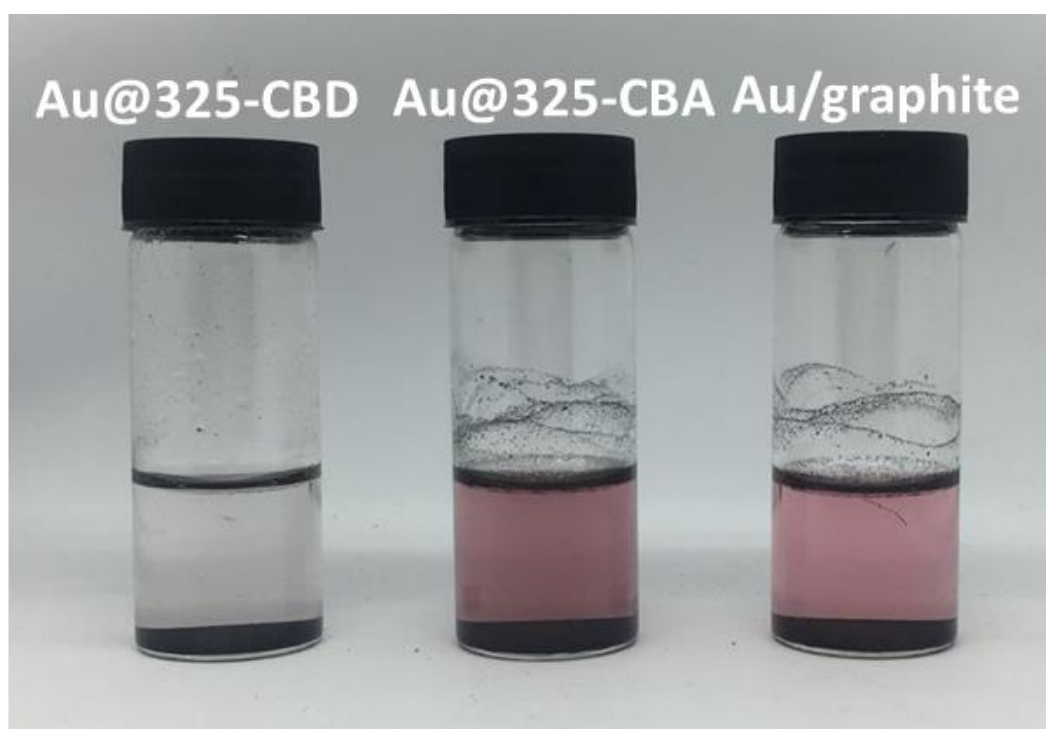
Figure 30 Images of Au/Graphite, Au@325-CBD, and Au@325-CBA samples after 24 h standing.

As the amine group on the surface of Au-NPs has potential to interact with carboxyl groups, 325-CBA and 325-CBD were selected for the decoration of Au-NPs. Pristine 325 mesh graphite was also used for control experiment. In brief, 5 mg of graphite or functionalized graphene samples were dispersed in 10 ml potassium hydroxide solution (pH = 12) in three sample vials by 10 mins of bath sonication. Subsequently, 2 ml of prepared Au-NPs solution was added into the dispersion and the system was sonicated for another 10 mins and maintained under stirring for 24 h. After that, the system was standing for 24 h to let the solid settle down. The final products were labeled as Au/graphite, Au@325-CBA and Au@325-CBD, respectively.
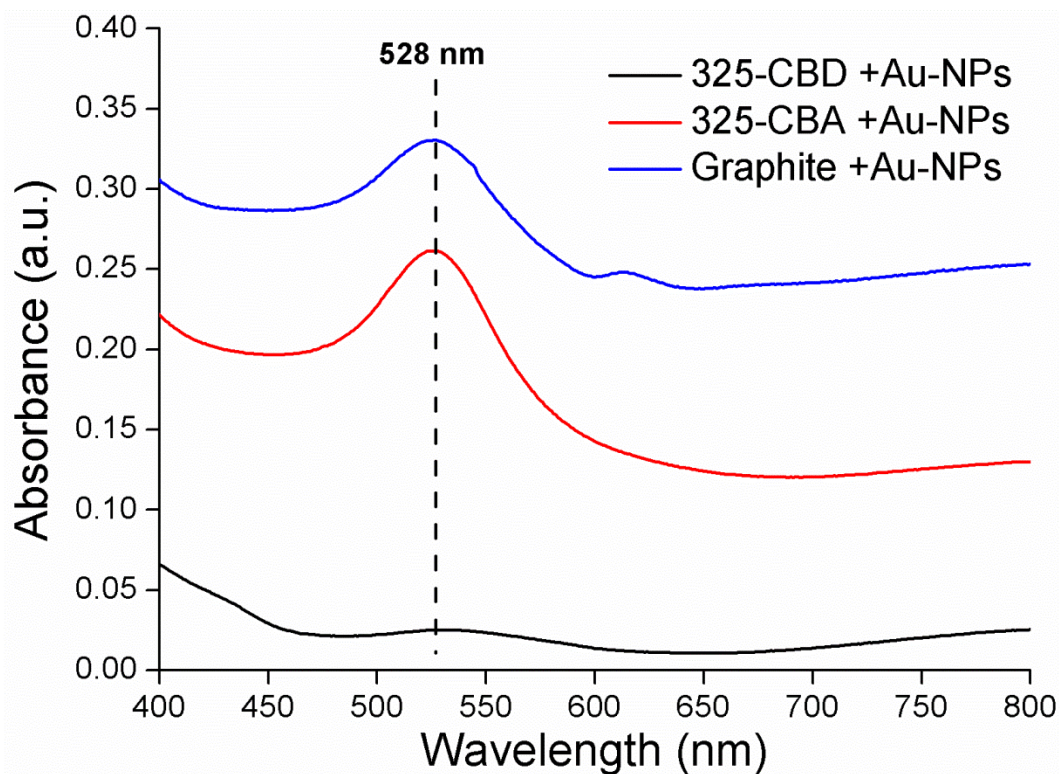
Figure 31 UV-Vis spectra of supernatant of Au/graphite, Au@325-CBD, and Au@325-CBA samples after

24 h standing.

As shown in Figure **30**, the supernatant in the vial containing 325-CBD sample became

colorless after standing, indicating the adsorption of Au-NPs. While the supernatant in other

two vials maintain faint red. UV-Vis spectra (Figure **31**) further confirmed that after 24 hours of

standing there was few Au-NPs left in the supernatant for Au@325-CBD sample, revealed by

the low absorbance (0.025) at 528 nm. In contrast, the absorbance of Au-NPs in Au/graphite

(0.33) and Au@325-CBA (0.26) samples were 13.2 and 10.4 times that of Au@325-CBD sample,

implying a much lower degree of Au-NPs adsorption. This could be attributed to low density of

anchor sites in pristine graphite and relatively low degree of functionalization of 325-CBA

sample.
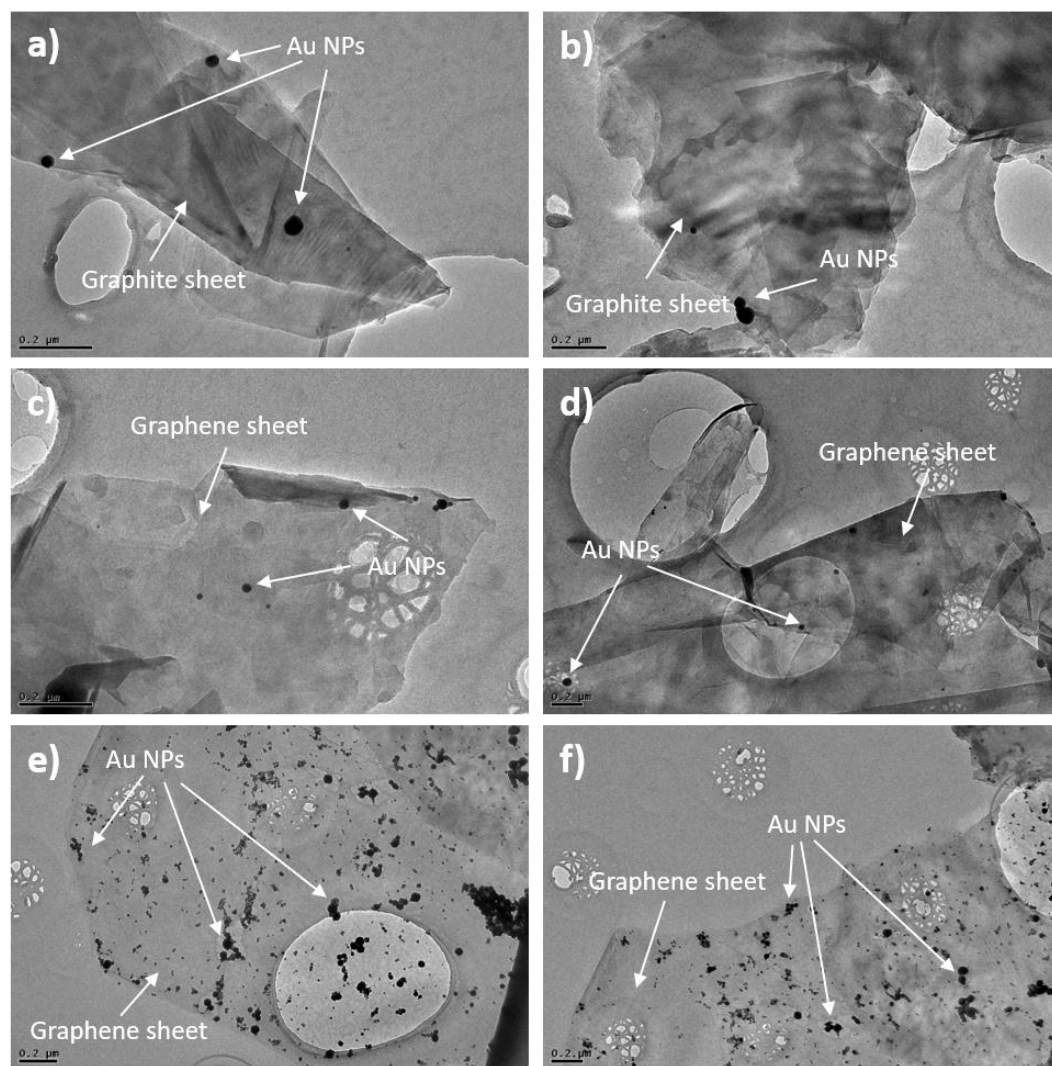
Figure 32 TEM images of Au/graphite (a, b), Au@325-CBA (c, d), and Au@325-CBD (e, f) samples.

TEM measurements were conducted for Au/graphite, Au@325-CBA, and Au@325-CBD samples after complete washing with water to remove any unbonded Au-NPs. As shown in Figure **32 a-d**, only a few nanoparticles were observed for Au/graphite and Au@325-CBA samples, this may due to the weak physical interaction between Au-NPs and carbon layers. By contrast, a higher density of decorated Au-NPs was observed for Au@325-CBD sample (Figure **32 e, f**). To gain a further view of the density of decorated Au-NPs, the average number of Au-NPs on graphite/functionalized graphene was calculated based on 5 TEM images at the same magnification with approximately equal area of graphite/graphene sheets and the result

is shown in Figure **33**. It was found that Au@325-CBD sample can reach up to the highest

density of bonded Au-NPs, which was about 18.3 times higher than that of Au/graphite sample

and 13.2 times higher than that of Au@325-CBA sample. This result further confirmed that the

carboxyl functionalized graphene can anchor anime functionalized Au-NPs and the diazonium

approach can achieve a higher degree of functionalization compared with bromide approach.
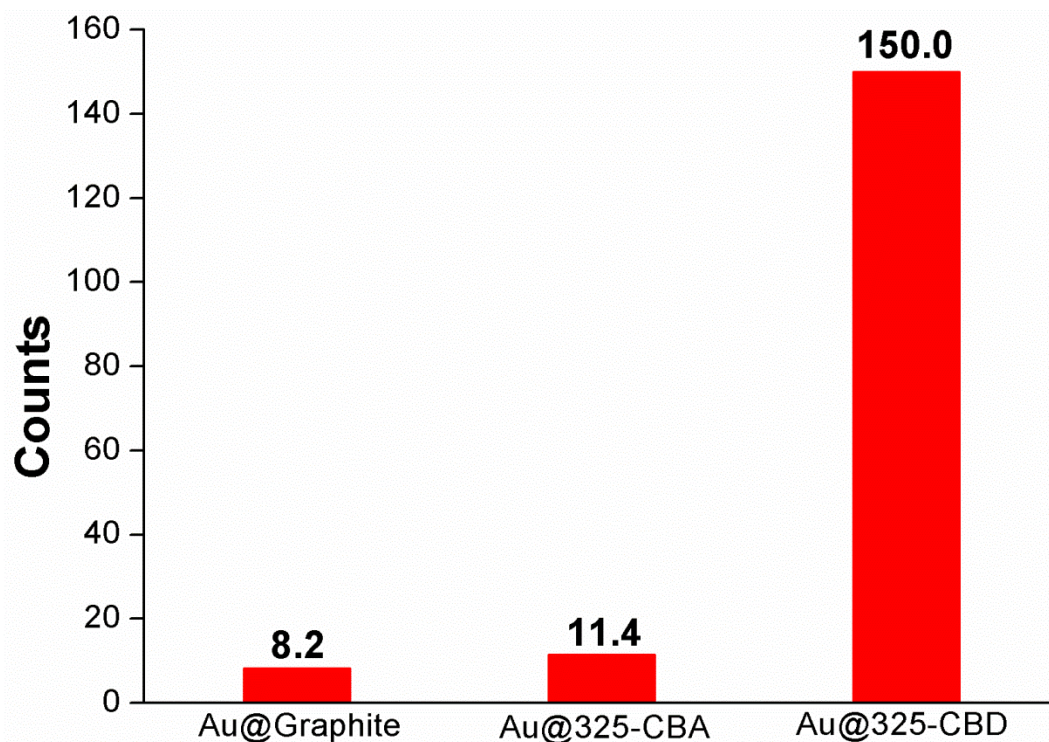
Figure 33 Average number of Au-NPs decorated on Au/graphite, Au@325-CBA, and Au@325-CBD

samples.

5.3 Conclusion

Amine functionalized positively Au-NPs have been successfully synthesized according to

the literature. The formation of Au-NPs was confirmed by UV-Vis characterization. For the

preparation of Au-NPs decorated functionalized graphene, 325-CBA and 325-CBD samples

were mixed with Au-NPs at room temperature in alkaline solution. Control experiment was

conducted by mixing graphite with Au-NPs under the same condition. TEM measurement revealed that Au@325-CBD reached up to the highest density of Au-NPs anchored on the surface of graphene. Few Au-NPs was decorated on Au@325-CBA and Au/graphite sample. This could be attributed to a relatively higher degree of functionalization of 325-CBD compared to 325-CBA.

Chapter 6: Experimental Section

6.1 General Instrumentation

6.1.1 Mass Spectrometry

The structure of the synthesized diazonium compounds were investigated by electron ionization (EI) (+) mass spectrometry on a TQD mass spectrometer and an Acquity UPLC (Waters Ltd, UK). Samples were prepared by dissolving 1 mg of the synthesized diazonium compounds in 1 ml of acetonitrile (HPLC grade).

6.1.2 Fourier Transform Infrared Spectroscopy (FT-IR)

FT-IR spectra were recorded on a Perkin Elmer Spectrum equipped with an attenuated Total Reflectance (ATR) accessory fitted with a diamond/KRS-5. Spectra were taken from 800 to 4000 cm^{-1} at a resolution of 1 cm^{-1}. Measurements were conducted for 8 scans for each sample and performed on solid samples under compression.

6.1.3 Powder XRD

The powder XRD measurements were conducted on a Bruker d8 Advance diffractometer using a Mo Kα source (λ = 0.7093 Å) operating at 40 kV and 50 mA, signal collected with a LYNXEYE detector. The potassium GIC samples were packed into a 1.0mm glass capillary inside the glove box and were rotated at 60 rpm during the measurement.

6.1.4 NMR

NMR samples were prepared in Methyl Sulfoxide-d_6 with a concentration of 1 mg/ml.

Data were collected on a Bruker 400 UltraShield NMR at 400 MHz.

6.1.5 Raman Spectroscopy

Raman spectra were recorded using a Horiba Jobin Yvon LabRam Evolution HR spectrometer in a back scattered confocal configuration using a Nd:YAG laser (532 nm, 2.33 eV.) The spectrometer was equipped with a CCD detector. Samples of the carbon materials were prepared by transferring the materials onto a membrane (0.2 μm pore size, PTFE, Hydrophilic) via filtration of the graphene dispersion (acetone), which was prepared by 5 mins sonication in an ultrasonic bath (Ultrawave U50, 30-40 kHz.). Samples were dried in air at 60 ℃ for 1 hour before test. All spectra were referenced to the position of the A_{1g} Raman active mode of Silicon at 520.7 cm^{-1}. Statistical Raman data was obtained from a 50 × 50 μm area with a 2.3 μm step size in the SWIFT mode for low integration times. Sample movement was carried out by an automated XY-scanning stage.

Analysis of the data was performed using the proprietary Labspec 6 data, where peak fits were obtained using classical least square (CLS) fitting with lineshapes that were permitted to have Lortenzian character.

6.1.6 Thermogravimetric Analysis (TGA)

TGA was carried out using a Pyris 1 TGA. Samples (1-10 mg) were heated under helium from room temperature to 500 ℃ at a rate of 5 ℃ per min.

6.1.7 Transition electron microscopy (TEM)

TEM images were acquired using a JEOL 2100F FEG TEM. Samples were prepared by

dispersing the solid powder in THF to give a dilute dispersion. Several drops of the solution were then placed onto a holey carbon grid. Imaging was conducted at a working voltage of 80 kV.

6.1.8 X-ray Photoelectron Spectroscopy (XPS)

The XPS measurements were acquired in a Kratos Axis Nova XPS spectrometer at NEXUS in Newcastle University. The samples were mounted on a clean aluminum platen and immobilized using carbon tape. The largest analysis area in this spectrometer (300x700 micron) was used in all the measurements. All the measurements were repeated at three different analysis positions with non-overlapping analysis areas. Charge compensation was used throughout the measurements. Survey scans were acquired with an energy resolution of 160 eV, and 0.4 eV steps, 100 ms dwell time and 2 sweeps. F 1s scans were acquired with an energy resolution of 20 eV, 0.1 eV steps, 300 ms dwell time and 10 sweeps.

6.2 Materials

The chemicals used in this project are listed below. All the chemicals were used as received without further statement.

Natural graphite flake (325 mesh, 99.8%)	Alfa Aesar
Tetrafluoroboric acid (48% min w/w aq. soln.)	Alfa Aesar
Graphite (Micrograft 99503UJ, 99.5%)	Nacional de Grafite, Brazil
Potassium hydroxide	Fischer Scientific

Hydrochloric acid	Fischer Scientific
Potassium cubes (in mineral oil, 99.5% trace metals basis)	Sigma Aldrich
4-Aminobenzoic acid (99%)	Sigma Aldrich
4-Fluoroaniline (99%)	Sigma Aldrich
4-Nitrobenzenediazonium tetrafluoroborate (97%)	Sigma Aldrich
4-Fluorobenzyl bromide (97%)	Sigma Aldrich
4-Bromomethyl benzoic acid (97%)	Sigma Aldrich
4-Nitrobenzyl bromide (99%)	Sigma Aldrich
Methyl Sulfoxide-d_6, for NMR (99.5+ %)	ACROS Organics
Acetonitrile (HPLC grade)	Fischer Scientific
Tetrahydrofuran	Durham SPS
Gold(III) chloride hydrate (50% Au basis)	Sigma Aldrich
Poly(ethyleneimine) solution (50% w/w in water)	Sigma Aldrich

6.3 Sample Preparation

6.3.1 Preparation of Graphite Intercalated Compounds (GICs) KC$_8$ by using 325 mesh natural graphite

The KC$_8$ graphite intercalated compounds (GICs) were prepared following the liquid

phase (LP) route in a nitrogen filled glove box (H_2O < 10 ppm, O_2 < 10 ppm)[132]. Typically, 0.5 g of

graphite (325 mesh) was mixed with 0.203 g potassium metal in the atomic ratio C/K = 8 in a glass vial. The vial was then put on a heating plate and heated to 200 °C. The system was maintained at this temperature for 4 hours, and the mixture was stirred occasionally with a spatula. During the intercalation, the grey black graphite powder was turned into golden brown powder. The system was then cooled down to room temperature.

6.3.2 Preparation of Graphite Intercalated Compounds (GICs) KC$_8$ (Micrograft graphite)

The KC$_8$ graphite intercalated compounds (GICs) were prepared following the liquid phase (LP) route in a nitrogen filled glove box (H$_2$O < 10 ppm, O$_2$ < 10 ppm)[132]. Typically, 0.5 g of graphite (Micrograft) was mixed with 0.203 g potassium metal in the atomic ratio C/K = 8 in a glass vial. The vial was then put on a heating plate up and heated up to 200 °C. The system was maintained at this temperature for 4 hours, and the mixture was stirred up occasionally with a spatula. During the intercalation, the grey black graphite powder was turned into golden brown powder. The system was then cooled down to room temperature.

6.3.3 Preparation of Graphenide solution – Approach 1

A modified literature procedure was followed[132]. Inside the glove box (H$_2$O < 10 ppm, O$_2$ < 10 ppm), 0.35 g of 325 mesh GICs was dispersed in 25 ml absolute THF in a 30 ml sample vial by tip sonication (33% amp., 5/5s pulse, 30 mins), the concentration of graphite was 10 mg/ml. Subsequently, the dispersion was stirred at 800 rpm for 5 days for further exfoliation. The dispersion was then centrifuged at 2,000 rpm for 30 mins to remove insoluble materials and the supernatant (graphenide) was collected. For measuring the concentration of graphenide

solution, 10 ml of grahpenide solution was quenched with 1 ml of methanol in the glove box. During the quenching procedure, graphene sheets were discharged and settled down as black solid. The sediment was collected via centrifugation and washed with water before drying at 100 °C under vacuum overnight. The mass of the discharged graphene was measured and the concentration of graphenide solution was calculated to be ~ 0.04 mg/mL.

6.3.4 Preparation of Graphenide Solution – Approach 2

A modified literature procedure was followed[132]. Inside the glove box (H_2O < 10 ppm, O_2 < 10 ppm), 0.10 g of metal potassium was mixed with 0.025 g of metal sodium in a glass vial. The mixture was pressed together with a spatula to form liquid Na/K alloy. The alloy was then transferred into a 30 ml glass vial containing 0.25 g of graphite (325 mesh graphite, the atomic ratio of C/K is 8), the concentration of graphite was 10 mg/ml. The vial was charged with 25 ml absolute THF and the dispersion was sonicated for 30 mins (amp. 33%, 5/5s pulse). The dark graphite dispersion was turned into golden brown dispersion during the sonication process indicating the formation of stage 1 KC_8. Subsequently, the dispersion was stirred at 800 rpm for 5 days for further exfoliation. The dispersion was then centrifuged at 2,000 rpm for 30 mins to remove insoluble materials and the supernatant (graphenide) was collected. For measuring the concentration of grapenide solution, 10 ml of grapenide solution was quenched with 1 ml of methanol in the glove box. During the quenching procedure, graphene sheets were discharged and settled down as black solid. The sediment was collected via centrifugation and washed with water before drying at 100 °C under vacuum overnight. The mass of the discharged graphene was measured and the concentration of graphenide solution was calculated to be ~ 0.15 mg/mL. To further improve the efficiency of exfoliation, we pre-shear mixed the

dispersion at 16,000 rpm for 30 mins and extended the sonication time to 1 hour, the concentration of the final graphenide solution was measured to be 0.8 mg/ml.

6.3.5 Synthesis of 4-Carboxybenzene Diazonium Tetrafluoroborate

Following a literature procedure[139], typically, to a solution of 4-Aminobenzoic acid (4.00 mmol, 548.56 mg) in H_2O (1.6 mL) was added 1.56 ml HBF_4 solution (48 wt. % aq.) and the mixture was stirred while cooling on ice. Subsequently, a solution of $NaNO_2$ (4.00 mmol, 276.00 mg) in H_2O (0.8 mL) was added dropwise. After addition, the reaction mixture was stirred for 30 mins on ice and subsequently filtered. The obtained crystals were washed with Et_2O and dried under vacuum. The products were stored at room temperature under N_2 atmosphere to prevent degradation. The characterization data was the same as that found in the literature[147].

Yield: 54%.

^{1}H NMR (DMSO-d_6) δ ppm 8.8 (m, J = 8.0 Hz, 2H); 8.4 (m, J = 8.0 Hz, 2H) ^{19}F NMR (DMSO-d_6) δ ppm -148.2; -148.3.

FT-IR (ATR solid): 2301 (-N_2^+)

MS (ESI) (m/z): [M]$^+$ calculated for $C_7H_5N_2O_2^+$: 149.13 found 149.93

6.3.6 Synthesis of 4-Fluorobenzene Diazonium Tetrafluoroborate

Following a literature procedure[139], to a solution of 4-Aminobenzoic acid (4.00 mmol, 444.48 mg) in H_2O (1.6 mL) added 1.56 ml HBF_4 solution (48 wt. % aq.) and the mixture was stirred while cooling on ice. Subsequently, a solution of $NaNO_2$ (4.00 mmol, 276.00 mg) in H_2O (0.8 mL) was added dropwise. After addition, the reaction mixture was stirred for 30 mins on

ice and subsequently filtered. The obtained crystals were washed with Et_2O and dried under vacuum. The products were stored at room temperature under N_2 atmosphere to prevent degradation. The characterization data was the same as that found in the literature[148].

Yield: 70%.

^1H NMR (DMSO-d_6) δ ppm 8.81-8.79 (m, 2H), 7.90 (t, J = 8.0 Hz, 2H) ^{19}F NMR (DMSO-d_6) δ ppm -87.1; -148.0; -148.1.

FT-IR (ATR solid): 2293 (-N_2^+)

MS (ESI) (m/z): $[M]^+$ calculated for $C_6H_4N_2F^+$: 123.11 found 123.93

6.3.7 Preparation of Functionalized KC$_8$ via Diazonium Approach

Inside the glove box (H_2O < 15 ppm, O_2 < 15 ppm), 51 mg of KC_8 (3.00 mmol carbon) was dispersed in 20 mL dry tetrahydrofuran (THF) via probe sonication (2 mins, 27 % amplify, 2/2s pulse). 4-carboxybenzene diazonium tetrafluoroborate (1.5 mmol) was weighed and added into the KC_8 dispersion dropwise under magnetic stirring, the mole ratio of carbon to bromide was 2:1. The reaction was maintained under stirring for 24 h after all the diazonium compounds was added. After that, the dispersion was taken out from the glove box and quenched with 1 ml methanol to remove the residual charge and filtrated on a 0.45 μm Nylon membrane. The filter cake was then washed with 150 ml acetone, 150 ml water and 50 ml ethanol to remove the residual reactant and potassium species. The obtained grey black powder was dried at 60 °C under vacuum overnight. The final product was labeled as 325-CBD, 325-FBD and 325-NBD for 325 mesh graphite GICs and SG-CBD, SG-FBD and SG-NBD for micrograft graphite

GICs.

6.3.8 Preparation of Functionalized KC$_8$ via Bromide Approach

The functionalization of KC$_8$ was conducted inside the glove box (H$_2$O < 10 ppm, O$_2$ < 10 ppm). Typically, 51 mg of KC$_8$ (3 mmol carbon) was dispersed in 20 mL dry tetrahydrofuran (THF) via probe sonication (2 mins, 27 % amplify, 2/2s pulse). Benzyl bromide (1.5 mmol) with various R group (R = COOH, F, and NO$_2$) was weighed and dissolved in 5 mL of absolute THF in another vial, the mole ratio of carbon to bromide was 2:1. Subsequently, the bromide THF solution was added into the KC$_8$ dispersion dropwise under magnetic stirring. The reaction was maintained under stirring for 24 h after all the bromide solution was added. After that, the dispersion was taken out from the glove box and quenched with 1 ml methanol to remove the residual charge and filtrated on a 0.45 μm Nylon membrane. The filter cake was then washed with 150 ml acetone, 150 ml water and 50 ml ethanol to remove the residual reactant and potassium species. The obtained black powder was dried at 60 ℃ under vacuum overnight. And the final products were labeled as 325-CBA, 325-FBB and 325-NBB for functionalized 325 mesh graphite GICs.

6.3.9 Preparation of Functionalized Graphenide via Diazonium Approach

The functionalization of graphenide was conducted inside the glove box (H$_2$O < 10 ppm, O$_2$ < 10 ppm). Typically, a glass bottle charged with 80 mg of graphenide solution (3.5 mmol carbon) was added with 1.75 mmol 4-Carboxybenzene Diazonium Tetrafluoroborate under vigorous stirring. The reaction was maintained under stirring for 24 h after all the diazonium compound was added. After that, the dispersion was taken out from the glove box and

quenched with 1 ml methanol to remove the residual charge and filtrated on a 0.45 μm Nylon membrane. The filter cake was then washed with 150 ml acetone, 150 ml water and 50 ml ethanol to remove the residual reactant and potassium species. The obtained black powder was dried at 60 ℃ under vacuum overnight and the product was labeled as graphenide-CBD.

6.3.10 Synthesis of Positively Charged Gold Nanoparticles (Au-NPs)

The positively charged gold nanoparticle was synthesized referring to the literature[145]. Briefly, a bottle was charged with 40 ml of polyethyleneimine (PEI solution, 50% w/w in water, 0.6 g) aqueous solution. Subsequently, 1 ml of 10 mg/ml of gold chloride hydrate solution was added to the system. After adjusting the pH of the system to 3.5, the mixture was allowed to stir for overnight at room temperature. The color of the mixture changed to a red color after reaction. The solution was used without any other treatment.

6.3.11 Preparation of Au-NPs Decorated Graphite/Functionalized Graphene

Briefly, 5 mg of 325 mesh graphite, 325-CBA and 325-CBD samples were dispersed in 10 ml potassium hydroxide solution (pH = 12) in three individual sample vials vial short time bath sonication (10 mins). 2 ml of the prepared Au-NPs solution was added into three sample vials and the dispersion was further sonicated for 10 mins. Subsequently, the system was maintained under stirring for 24 h, followed by another 24 h of standing to let the solid settle down. The sediment was collected by vacuum filtration and washed completely with water. The products were dried under vacuum at 60 ℃ overnight.

Chapter 7: Conclusion and Future Work

7.1 Conclusions

In this project, potassium GICs were prepared from 325 mesh graphite and graphite powder with smaller lateral size (S-Graphite, flake size < 5.2 μm), respectively. Raman spectroscopy and XRD showed that GICs prepared from 325 mesh graphite can reach a higher order of intercalation. The prepared GICs were then functionalized by diazonium compounds including 4-carboxybenzene diazonium tetrafluoroborate (4-CBD), 4-fluorobenzene diazonium tetrafluoroborate (4-FBD), and 4-nitrobenzene diazonium tetrafluoroborate (4-NBD). XPS characterization confirmed the successful attachment of functionality. Raman and TGA characterizations showed that the GICs prepared from 325 mesh graphite can achieve a higher degree of functionalization compared with S-Graphite GICs, which could be attributed to the higher order of intercalation of 325 mesh GICs. In addition, among these three diazonium salts, 4-CBD possessed the highest reactivity towards functionalization of GICs while 4-NBD possessed the lowest reactivity. Subsequently, various benzyl bromides including 4-bromomethyl benzoic acid (4-CBA), 4-fluorobenzyl bromide (4-FBB), and 4-nitrobenzyl bromide (4-NBB) were also used for the modification of 325 mesh GICs. It was found that 4-CBA and 4-FBB have comparable reactivity while 4-NBB has the lowest reactivity towards functionalization. Moreover, the reactivity of benzyl bromides was lower than that of diazonium compounds. Finally, the 325-CBD, 325-CBA and pristine graphite samples were decorated with amine modified gold nanoparticles (NH$_2$-AuNPs) and the hybrids were characterized by TEM. It was found that 325-CBD exhibited the highest adsorption capacity towards NH$_2$-AuNPs while 325-CBA and graphite showed comparable adsorption capacity.

7.2 Future work

7.2.1 Graphenide Solution

The work discussed in this thesis was predominantly about functionalized graphene directly from potassium GICs. However, more recently, graphenide has attracted great attention. Graphenide is a derivative of potassium GICs. It contains charged carbon layers, which can be well dispersed in organic solvents such as NMP and THF. They differ from potassium GICs the carbon layers in graphenide solution are fully exfoliated. This feature makes graphenide more promising for functionalization as there are more exposed electron doped surface. However, one of the drawbacks of graphenide solution is the low efficiency of graphite exploration in the solvents. For example, the concentration of graphenide in THF is usually less than 0.2 mg/ml [149]. Though the concentration can be improved to 0.8 mg/ml by using NMP as the solvent, the toxicity and high boiling point of NMP have restricted its application. To obtain a higher concentration of graphenide in THF, we have utilized two approaches for the preparation: 1) directly exfoliating potassium GICs in aprotic solvent, and 2) exfoliating graphite in alkali metal alloy (such as Na/K) dispersion. In our procedure, 325 mesh graphite was selected as the starting materials as it can reach to a higher order of intercalation. THF was selected as the aprotic solvent due to its low billing point and low toxicity compared with NMP. For method 1, 354 mg of 325 mesh GICs was dispersed in 25 ml THF via 0.5 h of tip sonication, the concentration of initial carbon was 10 mg/ml. The dispersion was then stirred at 800 rpm for 3 days to achieve further exfoliation of the GICs. After that, the dispersion was centrifuged at 1500 rpm for 30 mins to remove non-exfoliated large particles. The supernatant was collected and labeled as graphenide-1. For method 2, 250 mg of 325 mesh graphite was mixed

with Na/K liquid alloy in 25 ml THF. The Na/K alloy was made by pressing 102 mg of metal potassium and 25 mg of metal sodium, and the molar ratio of potassium to carbon was 1:8. As the Na/K alloy was liquid at room temperature, it can be well dispersed in THF to reach a high contact area with graphite sheets. The dispersion then experienced the same exfoliation as well as centrifugation process as described in method 1. The supernatant collected in method 2 was labeled as graphenide-2. For measuring the concentration of graphenide solution, 10 ml of graphenide-1 and graphenide-2 solution were charged with 1 ml of absolute methanol inside the glove box, respectively. As the quenching of negatively charged graphene by alcohols will only lead to the hydrogenation of graphene, the mass of graphene sheet was negligibly affected and could be accurately measured. After discharging, the black sediment was collected and washed with water to remove potassium species before drying under vacuum overnight. The mass of the powder was measured and the concentration of graphenide-1 and graphenide-2 was calculated to be 0.04 mg/ml and 0.14 mg/ml, respectively.

For further improving the production efficiency of method 2, the Na/K alloy –graphite dispersion was shear pre-mixed before the sonication process and the sonication time was extended to 1 hour. The concentration of the final graphenide solution was improved to 0.52 mg/ml.

To obtain a view of the reactivity of graphenide solution towards functionalization, the prepared graphenide solution was charged with 4-CBD. As shown in Figure **34b** and **34d**, a highly intense D band was observed for the graphenide-CBD sample and the I_D/I_G ratio of graphenide-CBD was comparable with that of 325-CBD (Table **4**), indicating a high degree of functionalization. It is also noteworthy that the I_{2D}/I_G ratio of graphenide-CBD sample was

higher than that of 325-CBD. This could be attributed to a higher degree of exfoliation.
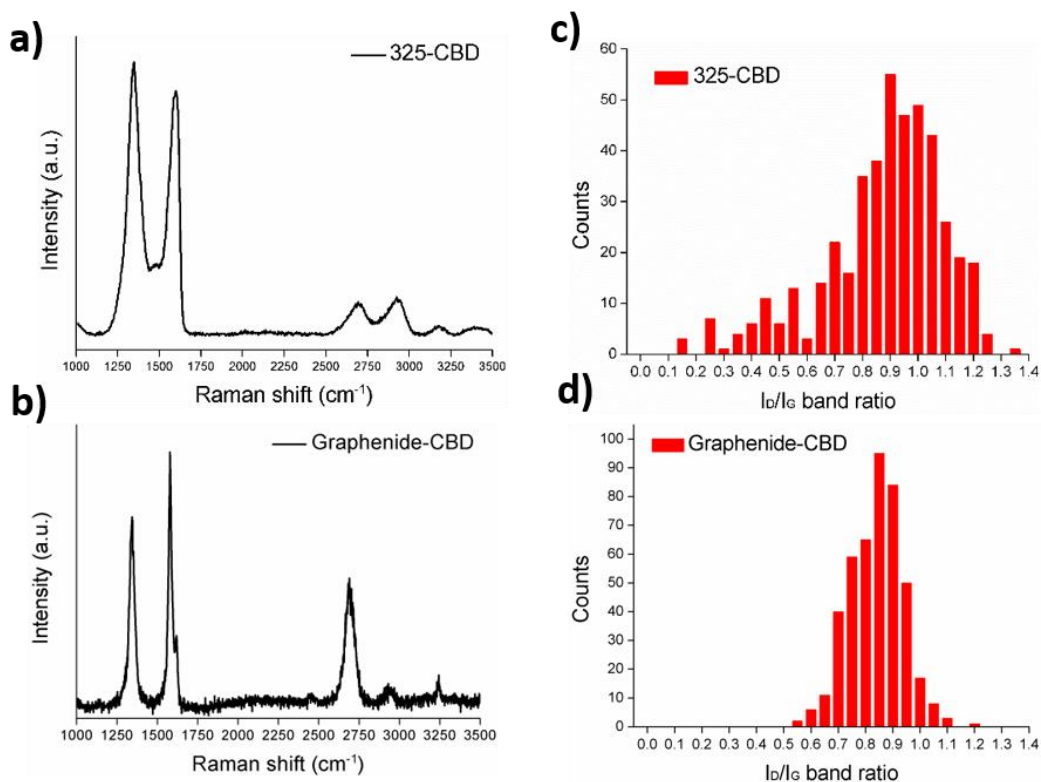
Figure 34 a, b) Raman spectra of 325-CBD and graphenide-CBD samples; c, d) Histogram of I_D/I_G ratio distribution of 325-CBD and graphenide-CBD samples.

In summary, highly exfoliated graphenide solution with high reactivity towards electrophile-type functionality can be prepared via a modified method. The as prepared graphenide could be recognized as an ideal candidate for further functionalization reactions.

Table 4 Average I_D/I_G Ratio and I_{2D}/I_G ratio of 325-CBD and Graphenide-CBD samples.

Sample name	I_D/I_G ratio (average)	$I_{2D/IG}$ ratio
325-CBD	0.90±0.22	0.14

Graphenide-CBD	0.86±0.098	0.52

7.2.2 Find an Application

In this project, we have reported an approach to covalently attach carboxyl group on the surface of graphene via diaoznium chemistry. And in Chapter 5, we have shown that NH_2-AuNPs can be successfully attached onto 325-CBD sample as amine group can interact well with carboxyl group. Consequently, it is reasonable to suspect other NH_2-rich nanoparticles/polymers can also be attached on 4-CBD functionalized graphene for specific application. For example, NH_2-rich polymers such as poly(allylamine hydrochloride) can be used to further functionalize 325-CBD via crosslinking to improve its dispersity in water[150]. Besides, NH_2-rich SiO_2 nanoparticles[151] can be anchored on the surface of 325-CBD to achieve a good distribution of SiO_2 nanoparticles as well as an improved carrier mobility of the hybrid, which then could be used as excellent Dye-Sensitized Solar Cells (DSSC) devices.

In general, the attachment of carboxyl group onto the surface of graphene made it a great platform for further deign of high-performance hybrids.

References

1. K. S. Novoselov, A. K. Geim, S. V. Morozov, D. Jiang, Y. Zhang, S. V. Dubonos, I. V. Grigorieva and A. A. Firsov, *Science*, 2004, **306**, 666-669.

2. B. Radisavljevic, A. Radenovic, J. Brivio, V. Giacometti and A. Kis, *Nat Nanotechnol*, 2011, **6**, 147-150.

3. C. L. Tan, X. H. Cao, X. J. Wu, Q. Y. He, J. Yang, X. Zhang, J. Z. Chen, W. Zhao, S. K. Han, G. H. Nam, M. Sindoro and H. Zhang, *Chem Rev*, 2017, **117**, 6225-6331.

4. H. Liu, A. T. Neal, Z. Zhu, Z. Luo, X. F. Xu, D. Tomanek and P. D. Ye, *Acs Nano*, 2014, **8**, 4033-4041.

5. C. Lee, X. D. Wei, J. W. Kysar and J. Hone, *Science*, 2008, **321**, 385-388.

6. F. Bonaccorso, L. Colombo, G. H. Yu, M. Stoller, V. Tozzini, A. C. Ferrari, R. S. Ruoff and V. Pellegrini, *Science*, 2015, **347**.

7. A. A. Balandin, S. Ghosh, W. Z. Bao, I. Calizo, D. Teweldebrhan, F. Miao and C. N. Lau, *Nano Lett*, 2008, **8**, 902-907.

8. R. R. Nair, P. Blake, A. N. Grigorenko, K. S. Novoselov, T. J. Booth, T. Stauber, N. M. R. Peres and A. K. Geim, *Science*, 2008, **320**, 1308-1308.

9. S. Bae, H. Kim, Y. Lee, X. F. Xu, J. S. Park, Y. Zheng, J. Balakrishnan, T. Lei, H. R. Kim, Y. I. Song, Y. J. Kim, K. S. Kim, B. Ozyilmaz, J. H. Ahn, B. H. Hong and S. Iijima, *Nat Nanotechnol*, 2010, **5**, 574-578.

10. D. C. Wei, B. Wu, Y. L. Guo, G. Yu and Y. Q. Liu, *Accounts Chem Res*, 2013, **46**, 106-115.

11. K. R. Paton, E. Varrla, C. Backes, R. J. Smith, U. Khan, A. O'Neill, C. Boland, M. Lotya, O. M. Istrate, P. King, T. Higgins, S. Barwich, P. May, P. Puczkarski, I. Ahmed, M. Moebius, H. Pettersson, E. Long, J. Coelho, S. E. O'Brien, E. K. McGuire, B. M. Sanchez, G. S. Duesberg, N. McEvoy, T. J. Pennycook, C. Downing, A. Crossley, V. Nicolosi and J. N. Coleman, *Nat Mater*, 2014, **13**, 624-630.

12. A. Ciesielski and P. Samori, *Chem Soc Rev*, 2014, **43**, 381-398.

13. X. L. Li, X. R. Wang, L. Zhang, S. W. Lee and H. J. Dai, *Science*, 2008, **319**, 1229-1232.

14. W. S. Hummers and R. E. Offeman, *J Am Chem Soc*, 1958, **80**, 1339-1339.

15. D. C. Marcano, D. V. Kosynkin, J. M. Berlin, A. Sinitskii, Z. Z. Sun, A. Slesarev, L. B. Alemany, W. Lu and J. M. Tour, *Acs Nano*, 2010, **4**, 4806-4814.

16. D. R. Dreyer, S. Park, C. W. Bielawski and R. S. Ruoff, *Chem Soc Rev*, 2010, **39**, 228-240.

17.   S. Mao, G. H. Lu and J. H. Chen, *Nanoscale*, 2015, **7**, 6924-6943.

18.   Y. X. Xu, G. Q. Shi and X. F. Duan, *Accounts Chem Res*, 2015, **48**, 1666-1675.

19.   A. C. Ferrari, F. Bonaccorso, V. Fal'ko, K. S. Novoselov, S. Roche, P. Boggild, S. Borini, F. H. L. Koppens, V. Palermo, N. Pugno, J. A. Garrido, R. Sordan, A. Bianco, L. Ballerini, M. Prato, E. Lidorikis, J. Kivioja, C. Marinelli, T. Ryhanen, A. Morpurgo, J. N. Coleman, V. Nicolosi, L. Colombo, A. Fert, M. Garcia-Hernandez, A. Bachtold, G. F. Schneider, F. Guinea, C. Dekker, M. Barbone, Z. P. Sun, C. Galiotis, A. N. Grigorenko, G. Konstantatos, A. Kis, M. Katsnelson, L. Vandersypen, A. Loiseau, V. Morandi, D. Neumaier, E. Treossi, V. Pellegrini, M. Polini, A. Tredicucci, G. M. Williams, B. H. Hong, J. H. Ahn, J. M. Kim, H. Zirath, B. J. van Wees, H. van der Zant, L. Occhipinti, A. Di Matteo, I. A. Kinloch, T. Seyller, E. Quesnel, X. L. Feng, K. Teo, N. Rupesinghe, P. Hakonen, S. R. T. Neil, Q. Tannock, T. Lofwander and J. Kinaret, *Nanoscale*, 2015, **7**, 4598-4810.

20.   E. B. Secor, S. Lim, H. Zhang, C. D. Frisbie, L. F. Francis and M. C. Hersam, *Adv Mater*, 2014, **26**, 4533-4538.

21.   K. Arapov, E. Rubingh, R. Abbel, J. Laven, G. de With and H. Friedrich, *Adv Funct Mater*, 2016, **26**, 586-593.

22.   P. G. Karagiannidis, S. A. Hodge, L. Lombardi, F. Tomarchio, N. Decorde, S. Milana, I. Goykhman, Y. Su, S. V. Mesite and D. N. Johnstone, *Acs Nano*, 2017, **11**, 2742.

23.   J. H. Du and H. M. Cheng, *Macromol Chem Phys*, 2012, **213**, 1060-1077.

24.   G. Kucinskis, G. Bajars and J. Kleperis, *J Power Sources*, 2013, **240**, 66-79.

25.   M. Pumera and C. H. A. Wong, *Chem Soc Rev*, 2013, **42**, 5987-5995.

26.   D. Berman, A. Erdemir and A. V. Sumant, *Mater Today*, 2014, **17**, 31-42.

27.   S. S. Chen, L. Brown, M. Levendorf, W. W. Cai, S. Y. Ju, J. Edgeworth, X. S. Li, C. W. Magnuson, A. Velamakanni, R. D. Piner, J. Y. Kang, J. Park and R. S. Ruoff, *Acs Nano*, 2011, **5**, 1321-1327.

28.   N. T. Kirkland, T. Schiller, N. Medhekar and N. Birbilis, *Corros Sci*, 2012, **56**, 1-4.

29.   R. K. S. Raman, P. C. Banerjee, D. E. Lobo, H. Gullapalli, M. Sumandasa, A. Kumar, L. Choudhary, R. Tkacz, P. M. Ajayan and M. Majumder, *Carbon*, 2012, **50**, 4040-4045.

30.   J. Hou, R. Wu, P. J. Zhao, A. M. Chang, G. Ji, B. Gao and Q. Zhao, *Mater Lett*, 2013, **100**, 173-176.

31.   W. C. Ren and H. M. Cheng, *Nat Nanotechnol*, 2014, **9**, 726-730.

32.   Y. H. Lee, X. Q. Zhang, W. J. Zhang, M. T. Chang, C. T. Lin, K. D. Chang, Y. C. Yu, J. T. W. Wang, C. S. Chang, L. J. Li and T. W. Lin, *Adv Mater*, 2012, **24**, 2320-2325.

33.   Y. M. Shi, C. Hamsen, X. T. Jia, K. K. Kim, A. Reina, M. Hofmann, A. L. Hsu, K.

Zhang, H. N. Li, Z. Y. Juang, M. S. Dresselhaus, L. J. Li and J. Kong, *Nano Lett*, 2010, **10**, 4134-4139.

34.   K. K. Kim, A. Hsu, X. T. Jia, S. M. Kim, Y. S. Shi, M. Hofmann, D. Nezich, J. F. Rodriguez-Nieva, M. Dresselhaus, T. Palacios and J. Kong, *Nano Lett*, 2012, **12**, 161-166.

35.   A. Reina, X. T. Jia, J. Ho, D. Nezich, H. B. Son, V. Bulovic, M. S. Dresselhaus and J. Kong, *Nano Lett*, 2009, **9**, 30-35.

36.   S. Yoshii, K. Nozawa, K. Toyoda, N. Matsukawa, A. Odagawa and A. Tsujimura, *Nano Lett*, 2011, **11**, 2628-2633.

37.   Q. K. Yu, J. Lian, S. Siriponglert, H. Li, Y. P. Chen and S. S. Pei, *Appl Phys Lett*, 2008, **93**.

38.   X. S. Li, W. W. Cai, J. H. An, S. Kim, J. Nah, D. X. Yang, R. Piner, A. Velamakanni, I. Jung, E. Tutuc, S. K. Banerjee, L. Colombo and R. S. Ruoff, *Science*, 2009, **324**, 1312-1314.

39.   Z. Yan, Z. W. Peng and J. M. Tour, *Accounts Chem Res*, 2014, **47**, 1327-1337.

40.   Q. K. Yu, L. A. Jauregui, W. Wu, R. Colby, J. F. Tian, Z. H. Su, H. L. Cao, Z. H. Liu, D. Pandey, D. G. Wei, T. F. Chung, P. Peng, N. P. Guisinger, E. A. Stach, J. M. Bao, S. S. Pei and Y. P. Chen, *Nat Mater*, 2011, **10**, 443-449.

41.   X. S. Li, C. W. Magnuson, A. Venugopal, J. H. An, J. W. Suk, B. Y. Han, M. Borysiak, W. W. Cai, A. Velamakanni, Y. W. Zhu, L. F. Fu, E. M. Vogel, E. Voelkl, L. Colombo and R. S. Ruoff, *Nano Lett*, 2010, **10**, 4328-4334.

42.   Z. Yan, J. Lin, Z. W. Peng, Z. Z. Sun, Y. Zhu, L. Li, C. S. Xiang, E. L. Samuel, C. Kittrell and J. M. Tour, *Acs Nano*, 2012, **6**, 9110-9117.

43.   H. Wang, G. Z. Wang, P. F. Bao, S. L. Yang, W. Zhu, X. Xie and W. J. Zhang, *J Am Chem Soc*, 2012, **134**, 3627-3630.

44.   L. Gan and Z. T. Luo, *Acs Nano*, 2013, **7**, 9480-9488.

45.   H. L. Zhou, W. J. Yu, L. X. Liu, R. Cheng, Y. Chen, X. Q. Huang, Y. Liu, Y. Wang, Y. Huang and X. F. Duan, *Nat Commun*, 2013, **4**.

46.   Y. F. Hao, M. S. Bharathi, L. Wang, Y. Y. Liu, H. Chen, S. Nie, X. H. Wang, H. Chou, C. Tan, B. Fallahazad, H. Ramanarayan, C. W. Magnuson, E. Tutuc, B. I. Yakobson, K. F. McCarty, Y. W. Zhang, P. Kim, J. Hone, L. Colombo and R. S. Ruoff, *Science*, 2013, **342**, 720-723.

47.   T. R. Wu, X. F. Zhang, Q. H. Yuan, J. C. Xue, G. Y. Lu, Z. H. Liu, H. S. Wang, H. M. Wang, F. Ding, Q. K. Yu, X. M. Xie and M. H. Jiang, *Nat Mater*, 2016, **15**, 43-47.

48.   L. B. Gao, W. C. Ren, H. L. Xu, L. Jin, Z. X. Wang, T. Ma, L. P. Ma, Z. Y. Zhang, Q. Fu,

L. M. Peng, X. H. Bao and H. M. Cheng, *Nat Commun*, 2012, **3**.

49. G. Imamura and K. Saiki, *J Phys Chem C*, 2011, **115**, 10000-10005.

50. S. J. Tang, H. M. Wang, H. S. Wang, Q. J. Sun, X. Y. Zhang, C. X. Cong, H. Xie, X. Y. Liu, X. H. Zhou, F. Q. Huang, X. S. Chen, T. Yu, F. Ding, X. M. Xie and M. H. Jiang, *Nat Commun*, 2015, **6**.

51. N. Mishra, J. Boeckl, N. Motta and F. Iacopi, *Phys Status Solidi A*, 2016, **213**, 2277-2289.

52. J. B. Casady and R. W. Johnson, *Solid State Electron*, 1996, **39**, 1409-1422.

53. C. Berger, Z. M. Song, X. B. Li, X. S. Wu, N. Brown, C. Naud, D. Mayou, T. B. Li, J. Hass, A. N. Marchenkov, E. H. Conrad, P. N. First and W. A. de Heer, *Science*, 2006, **312**, 1191-1196.

54. J. Hass, R. Feng, T. Li, X. Li, Z. Zong, W. A. de Heer, P. N. First, E. H. Conrad, C. A. Jeffrey and C. Berger, *Appl Phys Lett*, 2006, **89**.

55. K. V. Emtsev, A. Bostwick, K. Horn, J. Jobst, G. L. Kellogg, L. Ley, J. L. McChesney, T. Ohta, S. A. Reshanov, J. Rohrl, E. Rotenberg, A. K. Schmid, D. Waldmann, H. B. Weber and T. Seyller, *Nat Mater*, 2009, **8**, 203-207.

56. C. Virojanadara, M. Syvajarvi, R. Yakimova, L. I. Johansson, A. A. Zakharov and T. Balasubramanian, *Phys Rev B*, 2008, **78**.

57. W. A. de Heer, C. Berger, M. Ruan, M. Sprinkle, X. B. Li, Y. K. Hu, B. Q. Zhang, J. Hankinson and E. Conrad, *P Natl Acad Sci USA*, 2011, **108**, 16900-16905.

58. Y. M. Chang, H. Kim, J. H. Lee and Y. W. Song, *Appl Phys Lett*, 2010, **97**.

59. Y. Hernandez, V. Nicolosi, M. Lotya, F. M. Blighe, Z. Y. Sun, S. De, I. T. McGovern, B. Holland, M. Byrne, Y. K. Gun'ko, J. J. Boland, P. Niraj, G. Duesberg, S. Krishnamurthy, R. Goodhue, J. Hutchison, V. Scardaci, A. C. Ferrari and J. N. Coleman, *Nat Nanotechnol*, 2008, **3**, 563-568.

60. U. Khan, A. O'Neill, M. Lotya, S. De and J. N. Coleman, *Small*, 2010, **6**, 864-871.

61. E. Varrla, K. R. Paton, C. Backes, A. Harvey, R. J. Smith, J. McCauley and J. N. Coleman, *Nanoscale*, 2014, **6**, 11810-11819.

62. J. Q. Shang, F. Xue and E. Y. Ding, *Chem Commun*, 2015, **51**, 15811-15814.

63. P. Blake, P. D. Brimicombe, R. R. Nair, T. J. Booth, D. Jiang, F. Schedin, L. A. Ponomarenko, S. V. Morozov, H. F. Gleeson, E. W. Hill, A. K. Geim and K. S. Novoselov, *Nano Lett*, 2008, **8**, 1704-1708.

64. C. E. Hamilton, J. R. Lomeda, Z. Z. Sun, J. M. Tour and A. R. Barron, *Nano Lett*, 2009, **9**, 3460-3462.

65.   W. C. Du, X. Q. Jiang and L. H. Zhu, *J Mater Chem A*, 2013, **1**, 10592-10606.

66.   A. Ciesielski and P. Samor, *Adv Mater*, 2016, **28**, 6030-6051.

67.   L. Guardia, M. J. Fernandez-Merino, J. I. Paredes, P. Solis-Fernandez, S. Villar-Rodil, A. Martinez-Alonso and J. M. D. Tascon, *Carbon*, 2011, **49**, 1653-1662.

68.   A. M. Dimiev and J. M. Tour, *Acs Nano*, 2014, **8**, 3060-3068.

69.   W. W. Cai, R. D. Piner, F. J. Stadermann, S. Park, M. A. Shaibat, Y. Ishii, D. X. Yang, A. Velamakanni, S. J. An, M. Stoller, J. H. An, D. M. Chen and R. S. Ruoff, *Science*, 2008, **321**, 1815-1817.

70.   V. Georgakilas, J. N. Tiwari, K. C. Kemp, J. A. Perman, A. B. Bourlinos, K. S. Kim and R. Zboril, *Chem Rev*, 2016, **116**, 5464-5519.

71.   T. Kuila, A. K. Mishra, P. Khanra, N. H. Kim and J. H. Lee, *Nanoscale*, 2013, **5**, 52-71.

72.   T. Kuilla, S. Bhadra, D. H. Yao, N. H. Kim, S. Bose and J. H. Lee, *Prog Polym Sci*, 2010, **35**, 1350-1375.

73.   S. Stankovich, D. A. Dikin, G. H. B. Dommett, K. M. Kohlhaas, E. J. Zimney, E. A. Stach, R. D. Piner, S. T. Nguyen and R. S. Ruoff, *Nature*, 2006, **442**, 282-286.

74.   S. Stankovich, D. A. Dikin, R. D. Piner, K. A. Kohlhaas, A. Kleinhammes, Y. Jia, Y. Wu, S. T. Nguyen and R. S. Ruoff, *Carbon*, 2007, **45**, 1558-1565.

75.   C. K. Chua and M. Pumera, *Chem Soc Rev*, 2014, **43**, 291-312.

76.   S. Y. Toh, K. S. Loh, S. K. Kamarudin and W. R. W. Daud, *Chem Eng J*, 2014, **251**, 422-434.

77.   H. L. Guo, X. F. Wang, Q. Y. Qian, F. B. Wang and X. H. Xia, *Acs Nano*, 2009, **3**, 2653-2659.

78.   C. B. Liu, K. Wang, S. L. Luo, Y. H. Tang and L. Y. Chen, *Small*, 2011, **7**, 1203-1206.

79.   M. J. McAllister, J. L. Li, D. H. Adamson, H. C. Schniepp, A. A. Abdala, J. Liu, M. Herrera-Alonso, D. L. Milius, R. Car, R. K. Prud'homme and I. A. Aksay, *Chem Mater*, 2007, **19**, 4396-4404.

80.   Y. W. Zhu, S. Murali, M. D. Stoller, A. Velamakanni, R. D. Piner and R. S. Ruoff, *Carbon*, 2010, **48**, 2118-2122.

81.   D. Voiry, J. Yang, J. Kupferberg, R. Fullon, C. Lee, H. Y. Jeong, H. S. Shin and M. Chhowalla, *Science*, 2016, **353**, 1413-1416.

82.   R. J. Young, I. A. Kinloch, L. Gong and K. S. Novoselov, *Compos Sci Technol*, 2012, **72**, 1459-1476.

83.   V. Georgakilas, M. Otyepka, A. B. Bourlinos, V. Chandra, N. Kim, K. C. Kemp, P.

Hobza, R. Zboril and K. S. Kim, *Chem Rev*, 2012, **112**, 6156-6214.

84. A. Criado, M. Melchionna, S. Marchesan and M. Prato, *Angew Chem Int Edit*, 2015, **54**, 10734-10750.

85. E. Bekyarova, M. E. Itkis, P. Ramesh, C. Berger, M. Sprinkle, W. A. de Heer and R. C. Haddon, *J Am Chem Soc*, 2009, **131**, 1336-1337.

86. G. L. C. Paulus, Q. H. Wang and M. S. Strano, *Accounts Chem Res*, 2013, **46**, 160-170.

87. J. M. Englert, C. Dotzer, G. A. Yang, M. Schmid, C. Papp, J. M. Gottfried, H. P. Steinruck, E. Spiecker, F. Hauke and A. Hirsch, *Nat Chem*, 2011, **3**, 279-286.

88. C. K. Chua and M. Pumera, *Chem Soc Rev*, 2013, **42**, 3222-3233.

89. J. E. Johns and M. C. Hersam, *Accounts Chem Res*, 2013, **46**, 77-86.

90. J. L. Bahr, J. P. Yang, D. V. Kosynkin, M. J. Bronikowski, R. E. Smalley and J. M. Tour, *J Am Chem Soc*, 2001, **123**, 6536-6542.

91. M. S. Strano, C. A. Dyke, M. L. Usrey, P. W. Barone, M. J. Allen, H. W. Shan, C. Kittrell, R. H. Hauge, J. M. Tour and R. E. Smalley, *Science*, 2003, **301**, 1519-1522.

92. K. Flavin, M. N. Chaur, L. Echegoyen and S. Giordani, *Org Lett*, 2010, **12**, 840-843.

93. Z. Z. Sun, S. Kohama, Z. X. Zhang, J. R. Lomeda and J. M. Tour, *Nano Res*, 2010, **3**, 117-125.

94. S. Niyogi, E. Bekyarova, M. E. Itkis, H. Zhang, K. Shepperd, J. Hicks, M. Sprinkle, C. Berger, C. N. Lau, W. A. Deheer, E. H. Conrad and R. C. Haddon, *Nano Lett*, 2010, **10**, 4061-4066.

95. L. Gan, D. Y. Zhang and X. F. Guo, *Small*, 2012, **8**, 1326-1330.

96. M. Mooste, E. Kibena, J. Kozlova, M. Marandi, L. Matisen, A. Niilisk, V. Sammelselg and K. Tammeveski, *Electrochim Acta*, 2015, **161**, 195-204.

97. J. Greenwood, T. H. Phan, Y. Fujita, Z. Li, O. Lvasenko, W. Vanderlinden, H. Van Gorp, W. Frederickx, G. Lu, K. Tahara, Y. Tobe, H. Uji-i, S. F. L. Mertens and S. De Feyter, *Acs Nano*, 2015, **9**, 5520-5535.

98. Z. P. Qiu, J. Yu, P. Yan, Z. J. Wang, Q. J. Wan and N. J. Yang, *Acs Appl Mater Inter*, 2016, **8**, 28291-28298.

99. Q. Z. Wu, Y. P. Wu, Y. F. Hao, J. X. Geng, M. Charlton, S. S. Chen, Y. J. Ren, H. X. Ji, H. F. Li, D. W. Boukhvalov, R. D. Piner, C. W. Bielawski and R. S. Ruoff, *Chem Commun*, 2013, **49**, 677-679.

100. R. Sharma, J. H. Baik, C. J. Perera and M. S. Strano, *Nano Lett*, 2010, **10**, 398-405.

101. I. Y. Jeon, S. Y. Bae, J. M. Seo and J. B. Baek, *Adv Funct Mater*, 2015, **25**, 6961-6975.

102.   X. Zhong, J. Jin, S. W. Li, Z. Y. Niu, W. Q. Hu, R. Li and J. T. Ma, *Chem Commun*, 2010, **46**, 7340-7342.

103.   P. A. Denis, *Chem-Eur J*, 2013, **19**, 15719-15725.

104.   Y. Cao, S. Osuna, Y. Liang, R. C. Haddon and K. N. Houk, *J Am Chem Soc*, 2013, **135**, 17643-17649.

105.   L. Daukiya, C. Mattioli, D. Aubel, S. Hajjar-Garreau, F. Vonau, E. Denys, G. Reiter, J. Fransson, E. Perrin, M. L. Bocquet, C. Bena, A. Gourdon and L. Simon, *Acs Nano*, 2017, **11**, 627-634.

106.   D. C. Elias, R. R. Nair, T. M. G. Mohiuddin, S. V. Morozov, P. Blake, M. P. Halsall, A. C. Ferrari, D. W. Boukhvalov, M. I. Katsnelson, A. K. Geim and K. S. Novoselov, *Science*, 2009, **323**, 610-613.

107.   Z. Q. Luo, T. Yu, K. J. Kim, Z. H. Ni, Y. M. You, S. Lim, Z. X. Shen, S. Z. Wang and J. Y. Lin, *Acs Nano*, 2009, **3**, 1781-1788.

108.   S. L. Deng, Y. Zhang, A. H. Brozena, M. L. Mayes, P. Banerjee, W. A. Chiou, G. W. Rubloff, G. C. Schatz and Y. H. Wang, *Nat Commun*, 2011, **2**.

109.   J. Nossal, R. K. Saini, A. K. Sadana, H. F. Bettinger, L. B. Alemany, G. E. Scuseria, W. E. Billups, M. Saunders, A. Khong and R. Weisemann, *J Am Chem Soc*, 2001, **123**, 8482-8495.

110.   Z. Q. Yang, Y. Q. Sun, L. B. Alemany, T. N. Narayanan and W. E. Billups, *J Am Chem Soc*, 2012, **134**, 18689-18694.

111.   L. Wang, Z. Sofer, D. Bousa, D. Sedmidubsky, S. Huber, S. Matejkova, A. Michalcova and M. Pumera, *Angew Chem Int Edit*, 2016, **55**, 13965-13969.

112.   D. E. Palin and K. D. Wadsworth, *Nature*, 1948, **162**, 925-926.

113.   T. Nakajima, *Fluorine-carbon and fluoride-carbon materials: chemistry, physics, and applications*, CRC Press, 2001.

114.   E. T. Mickelson, C. B. Huffman, A. G. Rinzler, R. E. Smalley, R. H. Hauge and J. L. Margrave, *Chem Phys Lett*, 1998, **296**, 188-194.

115.   P. E. Pehrsson, W. Zhao, J. W. Baldwin, C. H. Song, J. Liu, S. Kooi and B. Zheng, *J Phys Chem B*, 2003, **107**, 5690-5695.

116.   R. R. Nair, W. C. Ren, R. Jalil, I. Riaz, V. G. Kravets, L. Britnell, P. Blake, F. Schedin, A. S. Mayorov, S. J. Yuan, M. I. Katsnelson, H. M. Cheng, W. Strupinski, L. G. Bulusheva, A. V. Okotrub, I. V. Grigorieva, A. N. Grigorenko, K. S. Novoselov and A. K. Geim, *Small*, 2010, **6**, 2877-2884.

117.   R. Zboril, F. Karlicky, A. B. Bourlinos, T. A. Steriotis, A. K. Stubos, V. Georgakilas, K. Safarova, D. Jancik, C. Trapalis and M. Otyepka, *Small*, 2010, **6**, 2885-2891.

118.   J. T. Robinson, J. S. Burgess, C. E. Junkermeier, S. C. Badescu, T. L. Reinecke, F. K. Perkins, M. K. Zalalutdniov, J. W. Baldwin, J. C. Culbertson, P. E. Sheehan and E. S. Snow, *Nano Lett*, 2010, **10**, 3001-3005.

119.   S. B. Bon, L. Valentini, R. Verdejo, J. L. G. Fierro, L. Peponi, M. A. Lopez-Manchado and J. M. Kenny, *Chem Mater*, 2009, **21**, 3433-3438.

120.   M. Baraket, S. G. Walton, E. H. Lock, J. T. Robinson and F. K. Perkins, *Appl Phys Lett*, 2010, **96**.

121.   M. S. Dresselhaus, A. Jorio, M. Hofmann, G. Dresselhaus and R. Saito, *Nano Lett*, 2010, **10**, 751-758.

122.   A. Das, S. Pisana, B. Chakraborty, S. Piscanec, S. K. Saha, U. V. Waghmare, K. S. Novoselov, H. R. Krishnamurthy, A. K. Geim, A. C. Ferrari and A. K. Sood, *Nat Nanotechnol*, 2008, **3**, 210-215.

123.   L. F. Lai, L. W. Chen, D. Zhan, L. Sun, J. P. Liu, S. H. Lim, C. K. Poh, Z. X. Shen and J. Y. Lin, *Carbon*, 2011, **49**, 3250-3257.

124.   D. Li, M. B. Muller, S. Gilje, R. B. Kaner and G. G. Wallace, *Nat Nanotechnol*, 2008, **3**, 101-105.

125.   D. M. Ottmers and H. F. Rase, *Carbon*, 1966, **4**, 125-127.

126.   N. Emery, C. Herold, M. d'Astuto, V. Garcia, C. Bellin, J. F. Mareche, P. Lagrange and G. Loupias, *Phys Rev Lett*, 2005, **95**, 087003.

127.   J. M. Englert, K. C. Knirsch, C. Dotzer, B. Butz, F. Hauke, E. Spiecker and A. Hirsch, *Chem Commun*, 2012, **48**, 5025-5027.

128.   M. Biswal, X. Zhang, D. Schilter, T. K. Lee, D. Y. Hwang, M. Saxena, S. H. Lee, S. S. Chen, S. K. Kwak, C. W. Bielawski, W. S. Bacsa and R. S. Ruoff, *J Am Chem Soc*, 2017, **139**, 4202-4210.

129.   T. Enoki, M. Suzuki and M. Endo, *Graphite intercalation compounds and applications*, Oxford University Press, New York, 2003.

130.   X. M. Geng, Y. F. Guo, D. F. Li, W. W. Li, C. Zhu, X. F. Wei, M. L. Chen, S. Gao, S. Q. Qiu, Y. P. Gong, L. Q. Wu, M. S. Long, M. T. Sun, G. B. Pan and L. W. Liu, *Sci Rep-Uk*, 2013, **3**.

131.   A. Penicaud and C. Drummond, *Accounts Chem Res*, 2013, **46**, 129-137.

132.   G. Bepete, F. Hof, K. Huang, K. Kampioti, E. Anglaret, C. Drummond and A. Penicaud, *Phys Status Solidi-R*, 2016, **10**, 895-899.

133.   E. G. C. Neiva, V. H. R. Souza, K. Huang, A. Penicaud and A. J. G. Zarbin, *J Colloid Interf Sci*, 2015, **453**, 28-35.

134.   R. A. Schafer, D. Dasler, U. Mundloch, F. Hauke and A. Hirsch, *J Am Chem Soc*, 2016,

138, 1647-1652.

135. J. Holzwarth, K. Y. Amsharov, D. I. Sharapa, D. Reger, K. Roshchyna, D. Lungerich, N. Jux, F. Hauke, T. Clark and A. Hirsch, *Angew Chem Int Edit*, 2017, **56**, 12184-12190.

136. J. C. Chacon-Torres and T. Pichler, *Phys Status Solidi B*, 2011, **248**, 2744-2747.

137. J. C. Chacon-Torres, S. Dzsaber, S. M. Vega-Diaz, J. Akbarzadeh, H. Peterlik, J. Kotakoski, G. Argentero, J. C. Meyer, T. Pichler, F. Simon, M. Terrones and S. Reich, *Carbon*, 2016, **105**, 90-95.

138. D. Dasler, R. A. Schafer, M. B. Minameyer, J. F. Hitzenberger, F. Hauke, T. Drewello and A. Hirsch, *J Am Chem Soc*, 2017, **139**, 11760-11765.

139. M. J. Hansen, M. M. Lerch, W. Szymanski and B. Feringa, *Angew Chem Int Edit*, 2016, **55**, 13514-13518.

140. K. Arapov, R. Abbel, G. de With and H. Friedrich, *Faraday Discuss*, 2014, **173**, 323-336.

141. Y. Choi, H. S. Bae, E. Seo, S. Jang, K. H. Park and B. S. Kim, *J Mater Chem*, 2011, **21**, 15431-15436.

142. M. Govindhan and A. C. Chen, *J Power Sources*, 2015, **274**, 928-936.

143. J. F. Liang, Z. B. Chen, L. Guo and L. D. Li, *Chem Commun*, 2011, **47**, 5476-5478.

144. S. Mao, G. H. Lu, K. H. Yu, Z. Bo and J. H. Chen, *Adv Mater*, 2010, **22**, 3521-3526.

145. X. Q. Gao, G. R. Xu, Y. Zhao, S. N. Li, F. Shi and Y. Chen, *Rsc Adv*, 2015, **5**, 88045-88051.

146. M. Yamamoto, Y. Kashiwagi, T. Sakata, H. Mori and M. Nakamoto, *Chem Lett*, 2007, **36**, 1348-1349.

147. F. Cicogna, I. Domenichelli, S. Coiai, F. Bellina, M. Lessi, R. Spiniello and E. Passaglia, *Polymer*, 2016, **82**, 366-377.

148. W. Erb, A. Hellal, M. Albini, J. Rouden and J. Blanchet, *Chem-Eur J*, 2014, **20**, 6608-6612.

149. Y. Wang, K. Huang, A. Derre, P. Puech, S. Rouziere, P. Launois, C. Castro, M. Monthioux and A. Penicaud, *Carbon*, 2017, **121**, 217-225.

150. H. T. Xing, J. H. Chen, X. Sun, Y. H. Huang, Z. B. Su, S. R. Hu, W. Weng, S. X. Li, H. X. Guo, W. B. Wu, Y. S. He, F. M. Li and Y. Huang, *Chem Eng J*, 2015, **263**, 280-289.

151. Y. Y. Fang, P. Ma, N. Q. Fu, X. W. Zhou, S. B. Fang and Y. Lin, *J Power Sources*, 2017, **370**, 20-26.